



**Fermi National Accelerator Laboratory**

FERMILAB-Pub-96/112

**Physics and Technology of the Next Linear Collider:  
A Report Submitted to Snowmass '96 by the NLC Zeroth-Order  
Design Group and the NLC Physics Working Group**

S. Kuhlman et al.

The NLC Accelerator Design Group and The NLC Physics Working Group

*Fermi National Accelerator Laboratory  
P.O. Box 500, Batavia, Illinois 60510*

February 1998

## **Disclaimer**

*This report was prepared as an account of work sponsored by an agency of the United States Government. Neither the United States Government nor any agency thereof, nor any of their employees, makes any warranty, expressed or implied, or assumes any legal liability or responsibility for the accuracy, completeness, or usefulness of any information, apparatus, product, or process disclosed, or represents that its use would not infringe privately owned rights. Reference herein to any specific commercial product, process, or service by trade name, trademark, manufacturer, or otherwise, does not necessarily constitute or imply its endorsement, recommendation, or favoring by the United States Government or any agency thereof. The views and opinions of authors expressed herein do not necessarily state or reflect those of the United States Government or any agency thereof.*

## **Distribution**

*Approved for public release; further dissemination unlimited.*

BNL 52-502  
FERMILAB-PUB-96/112  
LBNL-PUB-5425  
SLAC-Report-485  
UCRL-ID-124160  
UC-414  
June, 1996

Physics and Technology  
of the Next Linear Collider:

A Report Submitted to Snowmass '96  
by the NLC Zeroth-Order Design Group  
and the NLC Physics Working Group

hep-ex/9605011 30 May 1996

# The NLC Accelerator Design Group and The NLC Physics Working Group

S. Kuhlman;

*Argonne National Laboratory, Chicago, Illinois, USA*

P. Minkowski;

*University of Bern, Bern, Switzerland*

W. Marciano, F. Paige;

*Brookhaven National Laboratory, Upton, Long Island, New York, USA*

V. Telnov;

*Budker Institute for Nuclear Physics, Novosibirsk, Russia*

J. F. Gunion, T. Han, S. Lidia;

*University of California, Davis, California, USA*

J. Rosenzweig;

*University of California, Los Angeles, California, USA*

J. Wudka;

*University of California, Riverside, California, USA*

N. M. Kroll;

*University of California, San Diego, California, USA*

D. A. Bauer, H. Nelson;

*University of California, Santa Barbara, California, USA*

H. Haber, C. Heusch, B. Schumm;

*University of California, Santa Cruz, California, USA*

M. Gintner, S. Godfrey, P. Kalyniak;

*Carleton University, Ottawa, Canada*

L. Rinolfi;

*CERN, Geneva, Switzerland*

A. Barker, M. Danielson, S. Fahey, M. Goluboff, U. Nauenberg, D. L. Wagner;

*University of Colorado, Boulder, Colorado, USA*

P. C. Rowson;

*Columbia University, New York, New York, USA*

J. A. Holt, K. Maeshima, R. Raja;  
*Fermilab National Laboratory, Batavia, Illinois, USA*

H. Baer, R. Munroe;  
*Florida State University, Tallahassee, Florida, USA*

X. Tata;  
*University of Hawaii, Honolulu, Hawaii, USA*

T. Takahashi, T. Ohgaki;  
*Hiroshima University, Hiroshima, Japan*

R. van Kooten;  
*Indiana University, Bloomington, Indiana, USA*

M. Akemoto, T. Higo, K. Higashi, K. Kubo, K. Oide, K. Yokoya;  
*KEK National Laboratory, Tsukuba, Japan*

A. Jackson, W. A. Barletta, J. M. Byrd, S. Chattopadhyay, J. N. Corlett, W. M. Fawley,  
J. L. Feng, M. Furman, E. Henestroza, R. A. Jacobsen, K.-J. Kim, H. Li, H. Murayama,  
L. Reginato, R. A. Rimmer, D. Robin, M. Ronan, A. M. Sessler, D. Vanecek, J. S. Wurtele,  
M. Xie, S. S. Yu, A. A. Zholents;  
*Lawrence Berkeley National Laboratory, Berkeley, California, USA*

L. Bertolini, K. Van Bibber, D. Clem, F. Deadrick, T. Houck, D. E. Klem, M. Perry,  
G. A. Westenskow;  
*Lawrence Livermore National Laboratory, Livermore, California, USA*

B. Barakat;  
*Louisiana Tech University, Ruston, Louisiana, USA*

A. J. Dragt, R. L. Gluckstern;  
*University of Maryland, College Park, Maryland, USA*

S. R. Hertzbach;  
*University of Massachusetts, Amherst, Massachusetts, USA*

P. Burrows, M. Fero;  
*Massachusetts Institute of Technology, Cambridge, Massachusetts, USA*

M. Einhorn, G. L. Kane, K. Riles;  
*University of Michigan, Ann Arbor, Michigan, USA*

G. Giordano;  
*University of Milano, Milan, Italy*

G. B. Cleaver, K. Tanaka;  
*Ohio State University, Columbus, Ohio, USA*

J. Brau, R. E. Frey, D. Strom;  
*University of Oregon, Eugene, Oregon, USA*

R. Hollebeek;  
*University of Pennsylvania, Philadelphia, Pennsylvania, USA*

K. McDonald;  
*Princeton University, Princeton, New Jersey, USA*

G. Couture;  
*Université de Québec à Montreal, Montreal, Quebec, Canada*

D. D. Meyerhofer;  
*University of Rochester, Rochester, New York, USA*

F. Cuypers;  
*Paul Scherrer Institute*

C. Adolphsen, R. Aiello, R. Alley, R. Assmann, K. L. Bane, T. Barklow, V. Bharadwaj, J. Bogart, G. B. Bowden, G. Bower, M. Breidenbach, K. L. Brown, D. L. Burke, Y. Cai, G. Caryotakis, R. L. Cassel, P. Chen, S. L. Clark, J. E. Clendenin, C. Corvin, F.-J. Decker, A. Donaldson, R. Dubois, R. A. Early, K. R. Eppley, S. Ecklund, J. Eichner, P. Emma, L. Eriksson, Z. D. Farkas, A. S. Fisher, C. Foundoulis, W. R. Fowkes, J. Frisch, R. W. Fuller, L. Genova, S. Gold, G. Gross, S. Hanna, S. Hartman, S. A. Heifets, L. Hendrickson, R. H. Helm, J. Hewett, H. A. Hoag, J. Hodgson, J. Humphrey, R. Humphrey, J. Irwin, J. Jaros, R. K. Jobe, R. M. Jones, L. P. Keller, K. Ko, R. F. Koontz, E. Kraft, P. Krejcik, A. Kulikov, T. L. Lavine, Z. Li, W. Linebarger, G. A. Loew, R. J. Loewen, T. W. Markiewicz, T. Maruyama, T. S. Mattison, B. McKee, R. Messner, R. H. Miller, M. G. Minty, W. Moshhammer, M. Munro, C. D. Nantista, E. M. Nelson, W. R. Nelson, C. K. Ng, Y. Nosochkov, D. Palmer, R. B. Palmer, J. M. Paterson, C. Pearson, M. E. Peskin, R. M. Phillips, N. Phinney, R. Pope, T. O. Raubenheimer, J. Rifkin, T. Rizzo, S. H. Rokni, M. C. Ross, R. E. Ruland, R. D. Ruth, A. Saab, H. Schwarz, B. Scott, J. C. Sheppard, H. Shoaee, S. Smith, W. L. Spence, C. M. Spencer, J. E. Spencer, D. Sprehn, G. Stupakov, H. Tang, S. G. Tantawi, P. Tenenbaum, F. Tian, S. Thomas, K. A. Thompson, J. Turner, T. Usher, A. E. Vlieks, D. R. Walz, J. W. Wang, A. W. Weidemann, D. H. Whittum, P. B. Wilson, Z. Wilson, M. Woodley, M. Woods, Y. T. Yan, A. D. Yermian, F. Zimmermann;  
*Stanford Linear Accelerator Center, Stanford, California, USA*

B. F. L. Ward, A. Weidemann;  
*University of Tennessee, Knoxville, Tennessee, USA*

L. Sawyer, A. White;  
*University of Texas at Arlington, Arlington, Texas, USA*

C. Baltay, S. Manly;  
*Yale University, New Haven, Connecticut, USA*

# PREFACE

We present the prospects for the next generation of high-energy physics experiments with electron-positron colliding beams. This report summarizes the current status of the design and technological basis of a linear collider of center-of-mass energy 0.5–1.5 TeV, and the opportunities for high-energy physics experiments that this machine is expected to open.

Over the past two decades, particle physics experiments have made an increasingly precise confirmation of the “Standard Model” of strong, weak, and electromagnetic interactions. High-energy physicists feel confident that the basic structure of these once-mysterious interactions of elementary particles is now well understood. But the verification of this model has brought with it the realization that there is a missing piece to the story: although the structure of the weak interactions is based on a symmetry principle, we observe that symmetry to be broken, by an agent that we do not yet know. This agent, whatever its source, must provide new physical phenomena at the TeV energy scale.

The Large Hadron Collider (LHC) in Europe offers an entry into this energy regime with significant opportunity for discovery of new phenomena. An electron-positron collider at this next step in energy, the Next Linear Collider (NLC), will provide a complementary program of experiments with unique opportunities for both discovery and precision measurement. To understand the nature of the new phenomena at the TeV scale, to see how they fit together with the known particles and interactions into a grander picture, both of these facilities will be required.

In particular, electron-positron colliders offer specific features that are essential to understand the nature of these new interactions whatever their source. They allow precise and detailed studies of the two known particles that couple most strongly to these interactions, the  $W$  boson and the top quark. They provide a clean environment for the discovery of new particles whatever their nature, and they provide special tools, such as the use of electron beam polarization, to dissect the couplings of those particles.

All of this would be merely theoretical if the next-generation linear collider could not be realized. But, in the past few years, the technology of the linear collider has come of age. The experience gained from the operation of the Stanford Linear Collider (SLC) has provided a firm foundation to the design choices for the NLC. The fundamental new technologies needed to construct the NLC have been demonstrated experimentally. Microwave power sources have exceeded requirements for the initial stage of the NLC, and critical tests assure us that this technology can be expected to drive beams to a center-of-mass energies of a TeV or more. Essential demonstrations of prototype collider subsystems have either taken place or are now underway: the Final Focus Test Beam has already operated successfully; a linear accelerator and a damping ring will be operated within the next year. A detailed feasibility study, the “Zeroth-Order Design Report” (ZDR), has shown that these components can be integrated into a complete machine design.

The Next Linear Collider can be constructed, and it will play an essential role in our understanding of physics at the TeV energy scale.



# Contents

<b>Preface</b>	<b>v</b>
<b>1 The Next Linear Collider</b>	<b>1</b>
1.1 Goals for the Next Linear Collider . . . . .	1
1.2 Accelerator Design Choices . . . . .	4
1.2.1 The Stanford Linear Collider . . . . .	5
1.2.2 Future Linear Colliders . . . . .	6
1.3 The Next Linear Collider . . . . .	9
1.3.1 Technology Choice and Design Philosophy . . . . .	9
1.3.2 Status Report on Technologies for the NLC . . . . .	12
1.4 Outlook for the Next Linear Collider . . . . .	15
Bibliography for Chapter 1 . . . . .	17
<b>2 Physics Goals of the Next Linear Collider</b>	<b>19</b>
2.1 Introduction . . . . .	19
2.2 Standard Model Processes and Simulations . . . . .	24
2.2.1 Accelerator and Detector . . . . .	24
2.2.2 Simulations . . . . .	25
2.2.3 Standard Model Processes at the NLC . . . . .	26
2.3 Top Quark Physics . . . . .	30
2.3.1 Top Production, Decay, and Measurement . . . . .	30
2.3.2 Threshold Physics . . . . .	32
2.3.3 Top Couplings . . . . .	36
2.3.4 The Higgs-Top Yukawa Coupling . . . . .	40
2.3.5 Top Physics Reach of NLC and Hadron Colliders . . . . .	42
2.4 Higgs Boson Searches and Properties . . . . .	44
2.4.1 Introduction . . . . .	44

2.4.2	Present and Future Limits . . . . .	45
2.4.3	Standard Model Higgs . . . . .	48
2.4.4	Minimal Supersymmetric Standard Model Higgs . . . . .	52
2.4.5	Determination of Properties of Higgs Bosons . . . . .	55
2.4.6	Summary . . . . .	60
2.5	Supersymmetry . . . . .	61
2.5.1	Supersymmetry Signals at the NLC . . . . .	63
2.5.2	Superparticle Mass Measurements . . . . .	67
2.5.3	Supersymmetry Reach of the NLC and LHC . . . . .	72
2.6	Anomalous Gauge Boson Couplings . . . . .	79
2.6.1	Parametrization . . . . .	79
2.6.2	Present and Expected Pre-NLC Measurements . . . . .	80
2.6.3	Measurements in $W$ Pair Production at the NLC . . . . .	81
2.6.4	Measurements in Other Reactions at the NLC . . . . .	82
2.6.5	Conclusions . . . . .	83
2.7	Strong $WW$ Scattering . . . . .	86
2.7.1	The Reaction $e^+e^- \rightarrow W^+W^-$ . . . . .	86
2.7.2	The Reaction $e^+e^- \rightarrow \nu\bar{\nu}W^+W^-$ and $\nu\bar{\nu}ZZ$ . . . . .	88
2.7.3	The Reaction $e^+e^- \rightarrow \nu\bar{\nu}t\bar{t}$ . . . . .	90
2.7.4	Statistical significances at LHC versus NLC . . . . .	91
2.7.5	Conclusion . . . . .	93
2.8	New Gauge Bosons and Exotic Particles . . . . .	94
2.9	$e^-e^-$ , $e^-\gamma$ , and $\gamma\gamma$ Interactions . . . . .	99
2.9.1	Higgs Boson Studies . . . . .	100
2.9.2	Other New Physics Signatures . . . . .	102
2.9.3	Accelerator, Lasers, and the Interaction Region . . . . .	103
2.10	Precision Tests of QCD . . . . .	105
2.10.1	Precise Measurement of $\alpha_s$ . . . . .	105
2.10.2	Energy Evolution Studies . . . . .	107
2.10.3	Symmetry Tests Using Beam Polarization . . . . .	108
2.10.4	Gluon Radiation in $t\bar{t}$ Events; Anomalous Couplings . . . . .	108
2.11	Design of the NLC Detector . . . . .	109
2.12	Physics Processes which Constrain Detector Performance . . . . .	113
2.13	Conclusions . . . . .	115
	Bibliography for Chapter 2 . . . . .	117

<b>3</b>	<b>A Zeroth-Order Design for the Next Linear Collider</b>	<b>125</b>
3.1	Overview of Collider Systems . . . . .	125
3.1.1	Injectors and Damping Rings . . . . .	125
3.1.2	Bunch Length Compressors . . . . .	127
3.1.3	Main Linacs . . . . .	128
3.1.4	The Beam Delivery System . . . . .	128
3.1.5	Interaction Region . . . . .	130
3.2	Polarized Electron Injector . . . . .	131
3.3	Positron Source . . . . .	134
3.4	Damping Rings . . . . .	138
3.4.1	Main Damping Rings. . . . .	140
3.4.2	Positron Pre-Damping Ring . . . . .	142
3.5	Spin Rotators and Bunch Compressors . . . . .	144
3.6	Main Linacs: Design and Dynamics . . . . .	148
3.6.1	Linac Layout and Site Requirements . . . . .	150
3.6.2	Operation and Tuning of the Main Linacs . . . . .	153
3.7	The RF System for the Main Linacs . . . . .	158
3.7.1	Klystrons . . . . .	161
3.7.2	Modulators . . . . .	162
3.7.3	RF Pulse Compression and Power Transmission . . . . .	164
3.7.4	Accelerator Structure . . . . .	165
3.7.5	RF Drive and Phasing Systems . . . . .	170
3.7.6	Upgrade to 1 TeV . . . . .	171
3.7.7	Outlook . . . . .	173
3.8	Beam Delivery . . . . .	175
3.8.1	Collimation System . . . . .	176
3.8.2	IP Switch and Big Bend . . . . .	179
3.8.3	Final Focus . . . . .	180
3.9	Interaction Region and Detector Backgrounds . . . . .	183
3.9.1	Introduction . . . . .	183
3.9.2	Layout . . . . .	185
3.9.3	Backgrounds . . . . .	186
3.9.4	Quad Support and the Optical Anchor . . . . .	190
3.9.5	Conclusion . . . . .	193
	Bibliography for Chapter 3 . . . . .	194



# Chapter 1

## The Next Linear Collider

### 1.1 Goals for the Next Linear Collider

For the past 25 years accelerator facilities with colliding beams have been the forefront instruments used to study elementary particle physics at high energies (Fig. 1.1). Both hadron-hadron and electron-positron colliders have been used to make important observations and discoveries. Direct observations of the  $W^\pm$  and  $Z^0$  bosons at CERN and investigations of the top quark at Fermilab are examples of physics done at hadron colliders. Electron-positron colliders provide well-controlled and well-understood experimental environments in which new phenomena stand out and precise measurements can be made. The discoveries of the charm quark and  $\tau$  lepton at SPEAR, discovery of the gluon and establishment of QCD at PETRA and PEP, and precision exploration of electroweak phenomena at the SLC and LEP are highlights of the results produced by experiments at electron-positron colliders.

The ability to study nature with these two different kinds of instruments has proven essential to the advancement of our understanding of particle physics. This will remain true as we seek answers to questions posed at the TeV energy scale:

- What is the top quark, and what are its interactions?
- Why is the symmetry of the electroweak interaction broken, and what is the origin of mass?
- Do Higgs particles exist? If so, how many, and what are their structures and interactions?
- Is the world supersymmetric, and if so, what is its structure, and is this supersymmetry part of a larger unification of nature?
- Are quarks, leptons, and gauge bosons fundamental particles, or are they more complex?
- Are there other new particles or interactions, and what might nature contain that we have not yet imagined?

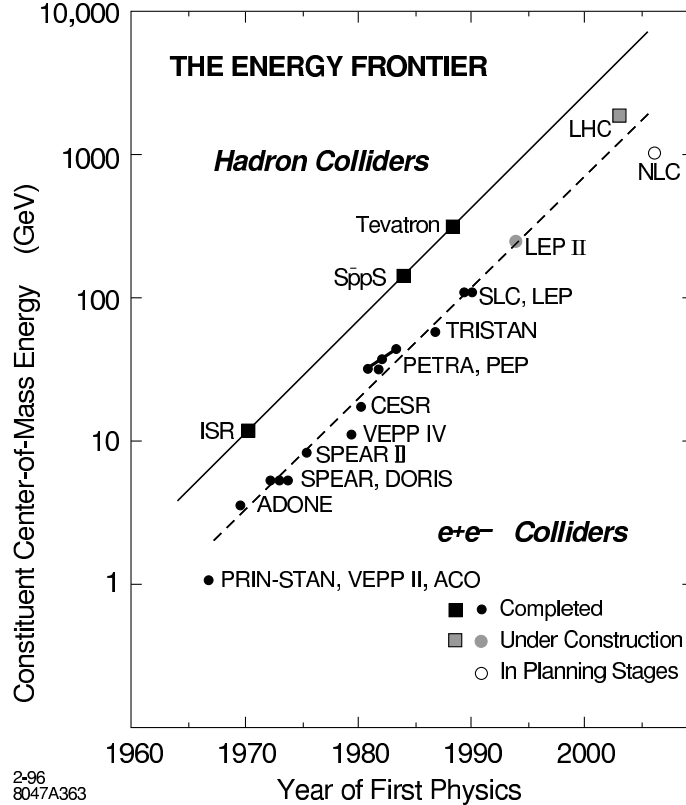


Figure 1.1: The energy frontier of particle physics. The effective constituent energy of existing and planned colliders and the year of first physics results from each.

The Large Hadron Collider (LHC) in Europe offers an entry into the TeV energy regime with significant opportunity for discovery of new phenomena. The planned participation in the design, construction, and utilization of this collider by nations around the world will make the LHC the first truly global facility for the study of particle physics. This will be an exciting and important step in the continuing evolution of our science.

The companion electron-positron collider at this next step in energy, the Next Linear Collider (NLC), will provide a complementary program of experiments with unique opportunities for both discovery and precision measurement. To understand the nature of physics at the TeV scale, to see how the new phenomena we expect to find there fit together with the known particles and interactions into a grander picture, both the LHC and the NLC will be required.

Studies of physics goals and requirements for the next-generation electron-positron collider began in 1987-88 in the United States [1, 2, 3], Europe [4, 5], and Japan [6, 7]. These regional studies have evolved into a series of internationally sponsored and organized workshops [8, 9, 10] that continue to build an important consensus on the goals and specifications of the Next Linear Collider. This document is both a part of this process, and input to

deliberations by the U.S. particle physics community that will take place this Summer at Snowmass, Colorado. To prepare for Snowmass, a series of workshops was held over the past year at locations throughout the United States. Working groups were established at a first meeting in Estes Park, Colorado to provide a framework for people to participate in the discussions of various topics in physics and experimentation at linear colliders. These groups continued to meet at subsequent workshops held at Fermilab, SLAC, and Brookhaven National Laboratory. This document contains a written summary from these workshops.

A picture has emerged of a high-performance collider able to explore a broad range of center of mass energies from a few hundred GeV to a TeV and beyond (Fig. 1.2). The goals of particle physics at the TeV scale require luminosities of approximately  $10^{34} \text{cm}^{-2} \text{sec}^{-1}$ , and reliable technologies that can provide large integrated data samples. It is important that the beam energy spread remain well controlled, and that backgrounds created by lost particles and radiation from the beams be maintained at low levels. This will assure that the clean experimental environment historically offered by electron-positron colliders remains intact. Beam polarization is an additional tool available at a linear collider that provides new and revealing views of particle physics, and this too is a requirement for any future collider.

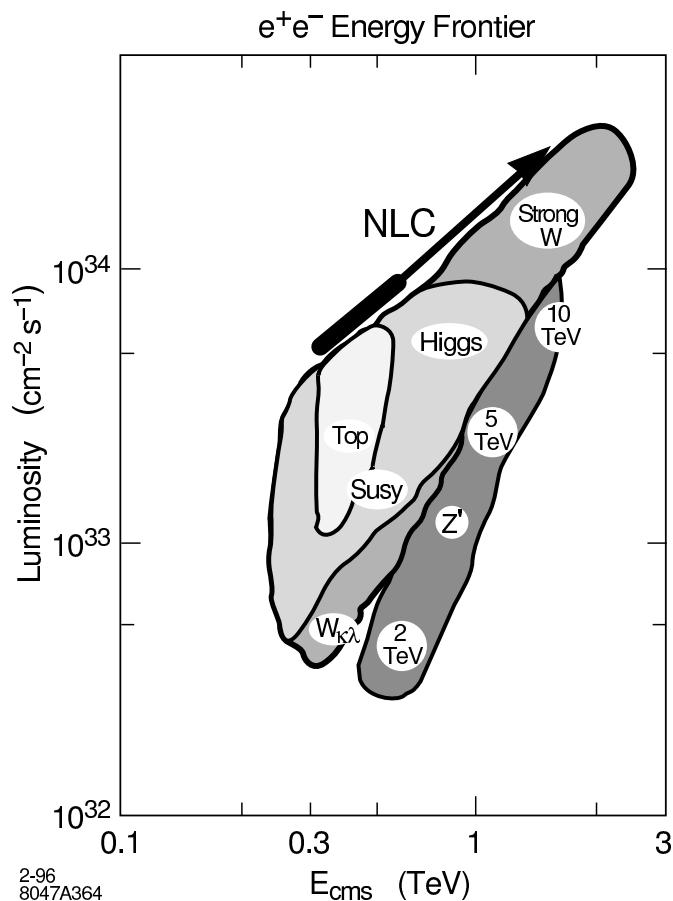


Figure 1.2: Physics goals for a TeV-scale  $e^+e^-$  collider.

In this first chapter we introduce the accelerator physics and technologies of the Next Linear Collider, discuss design choices and philosophies, and provide a brief status report on the R&D program that is being carried out in support of the NLC design effort. The second chapter of this document concentrates on the physics program of the NLC. The final chapter gives a more detailed overview of the accelerator design. A companion document, *A Zeroth-Order Design Report for the Next Linear Collider*, that contains results from a rather extensive feasibility study of the NLC, has also been prepared [11]. This may be of further interest to readers.

## 1.2 Accelerator Design Choices

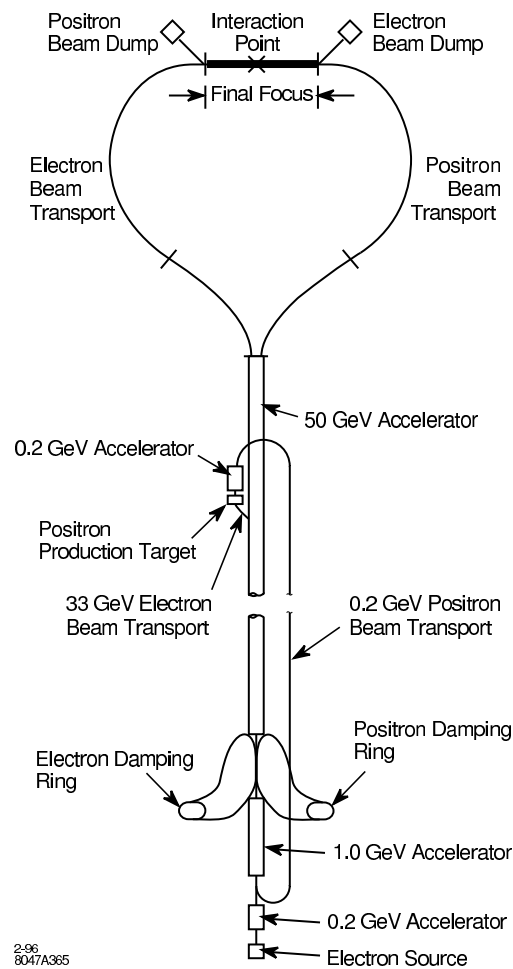


Figure 1.3: The Stanford Linear Collider (SLC).

### 1.2.1 The Stanford Linear Collider

The Stanford Linear Collider (Fig. 1.3) was conceived and built to accomplish two goals: to study particle physics at the 100-GeV energy scale, and to develop the accelerator physics and technology necessary for the realization of future high-energy colliders. The SLC was completed in 1987 and provided a first look at the physics of the  $Z^0$  in 1989. In time, the luminosity provided by this machine has grown steadily (Fig. 1.4), and has allowed particle physicists to make unique and important studies of the  $Z^0$  and its decays.

The design of the Next Linear Collider (NLC) presented in this document is intimately connected with experiences gained at the SLC. Our choices of technologies and philosophies of design have direct links to these experiences and considerable overlap with them. Lessons have been learned and techniques developed at the SLC that are relevant to the design and implementation of every part and system of the NLC:

- Injectors
  - Stabilized high-power electron sources
  - Polarized electrons
  - High-power targets and positron capture
- Damping Rings
  - Stabilized fast (50 ns) injection and extraction systems
  - Sub-picosecond phase synchronization with linac rf systems
- Linear Accelerator
  - Beam Acceleration
    - Management of large rf systems
    - Rf phase control
    - “Time-slot” compensation
    - Short-range longitudinal wake compensation
    - Multibunch beam loading compensation
  - Emittance Preservation
    - Beam-based alignment
    - LEM—lattice/energy matching
    - BNS damping
    - Coherent wakefield cancellation
    - Dispersion-free steering
- Final Focus Systems
  - Second-order chromatic optics and tuning
  - Precision diagnostics
  - Beam-beam control and tuning
- Experimentation
  - Theory and modeling of backgrounds

- Vulnerability of detector technologies
- Collimation—theory and implementation
- Systems Performance and Operation
  - Precision instrumentation—BPMs and wire scanners
  - Feedback theory and implementation
  - Importance of on-line modeling and analysis
  - Automated diagnostics and tuning
  - Mechanical stabilization of supports and components
  - Thermal stabilization of supports and components
  - Reliability
  - History monitoring (from seconds to years)

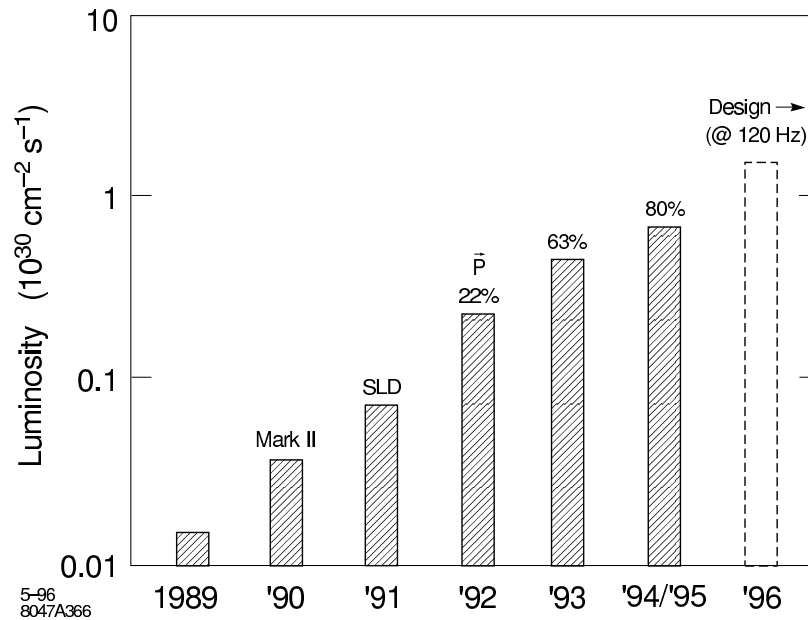


Figure 1.4: Performance of the SLC from early commissioning. Polarization of the electron beam is also shown.

## 1.2.2 Future Linear Colliders

The basic components of any linear collider are those already incorporated into the SLC; a generic collider complex is diagrammed in Fig. 1.5. The energy of such a future collider must be ten times that of the SLC, and a TeV-scale collider must be able to deliver luminosities that are several orders of magnitude greater than those achieved at the SLC. Trains of bunches of electrons and positrons are created, condensed in damping rings, accelerated to

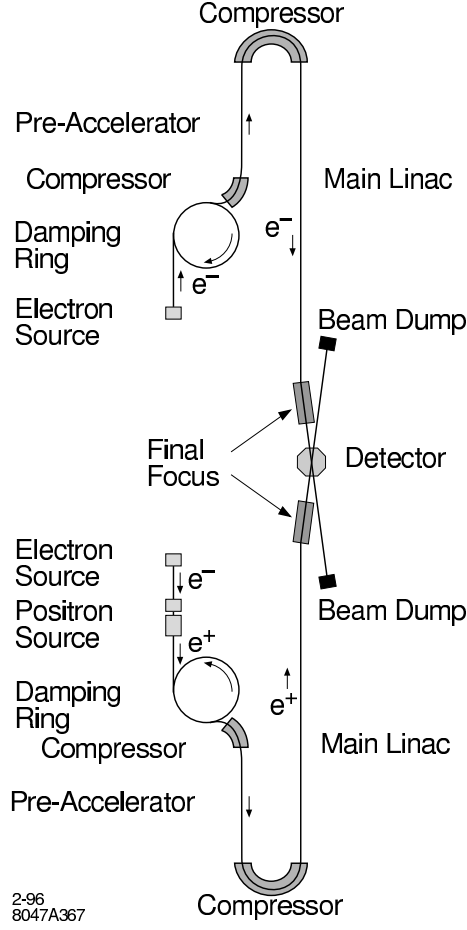


Figure 1.5: Schematic of a TeV-scale linear collider.

high energy, focused to small spots, and collided to produce a luminosity given by

$$L = \frac{nN^2Hf}{4\pi\sigma_x^*\sigma_y^*} \quad , \quad (1.1)$$

where

- $n$  = number of bunches per train,
- $N$  = number of particles per bunch,
- $H$  = beam pinch enhancement,
- $f$  = machine repetition rate,

and  $\sigma_x^*$  and  $\sigma_y^*$  are the horizontal and vertical beam dimensions at the collision point. Equation 1.1 can be written as

$$L = \frac{1}{4\pi E} \frac{NH}{\sigma_x^*} \frac{P}{\sigma_y^*} \quad , \quad (1.2)$$

where  $P$  is the average power in each beam. The factor  $N/\sigma_x^*$  determines the number of beamstrahlung photons emitted during the beam-beam interaction, and since these photons will alter the effective spread in beam collision energies and can create backgrounds in experimental detectors, this factor is highly constrained. It is mainly the last ratio,  $P/\sigma_y^*$ , that can be addressed by accelerator technology; high luminosity corresponds to high beam power and/or small beam spots. These two parameters pose different, and in many cases contrary, challenges to the accelerator physicist, and several technologies that represent differing degrees of compromise between beam power and spot size are being developed. Table 1.1 summarizes the initial stage of the mainstream design choices.

Table 1.1: Linear collider design parameters ( $E_{\text{cms}} = 500$  GeV).

	Frequency (GHz)	Gradient (MV/m)	Total Length (km)	Beam Power (MW)	$\sigma_y$ (nm)	Luminosity ( $10^{33} \text{ cm}^{-2} \text{ s}^{-1}$ )
SuperC	1.3	25	30	8.2	19	6
S-Band	3.0	21	30	7.3	15	5
X-Band	11.4	50	16	4.8	5.5	6
2-Beam	30.0	80	9	2.7	7.5	5

Each of the technologies in Table 1.1 is being pursued by physicists and engineers at laboratories around the globe. This strong international effort is remarkably well coordinated through collaborations that together provide a set of test facilities to address each of the important aspects of the collider design and implementation. A summary of the facilities presently in operation or under construction is given in Table 1.2.

Table 1.2: Linear collider test facilities around the world.

Facility	Location	Goal	Operations
SLC	SLAC	Prototype Collider	1988
ATF	KEK	Injector and Damping Ring	1995
TTF	DESY	SuperC Linac	1997
SBTF	DESY	S-band Linac	1996
NLCTA	SLAC	X-band Linac	1996
CTF	CERN	2-Beam Linac	1996
FFTB	SLAC	Final Focus/IR	1994

## 1.3 The Next Linear Collider

### 1.3.1 Technology Choice and Design Philosophy

The goal to reach 1 to 1.5-TeV cms energy with luminosities of  $10^{34} \text{ cm}^{-2} \text{ s}^{-1}$  or more and our experiences with the SLC, guide our choice of technologies for the NLC. We believe that the most natural match to these design goals is made with normal-conducting X-band (11.424 GHz) microwave components patterned after the S-band technology used in the SLC. A schematic of a section of the rf system of the NLC is shown in Fig. 1.6. Our choice of technology has required the development of new advanced rf klystrons and pulse-compression systems, but provides confidence that accelerating gradients of 50–100 MV/m can be achieved and used in the implementation of the collider. The technical risk of building a collider with new X-band technologies is perhaps greater than simply building a larger SLC at S-Band, but the goal to reach 1–1.5 TeV is substantially more assured, and capital costs to reach these energies will be lower.

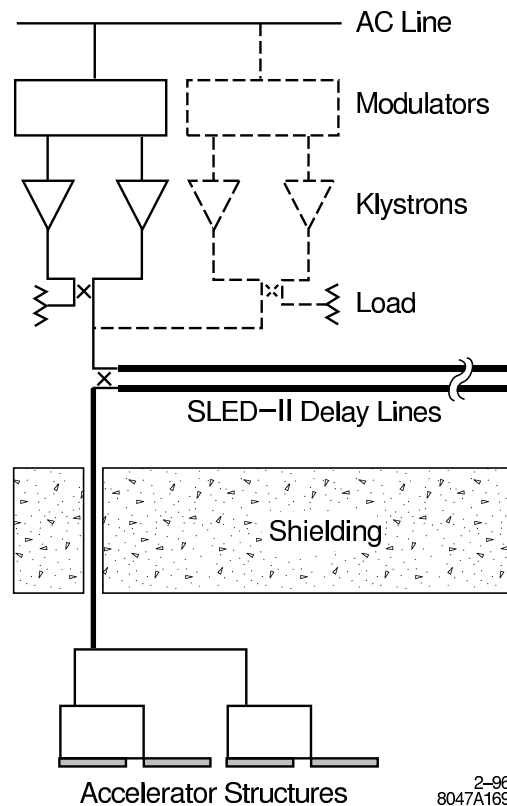


Figure 1.6: Normal-conducting rf system module in NLC main linacs. The dashed elements are expected to be necessary to reach 1 TeV cms energy.

The NLC is designed with nominal cms energy of 1 TeV. It is envisaged to be built with

an initial rf system able to drive the beams to 0.5-TeV cms energy, but with all infrastructure and beam lines able to support 1 TeV. The rf system design incorporates the ability to replace and add modulators and klystrons without access to the accelerator beam line (dashed lines in Fig. 1.6), so an unobtrusive, smooth, and adiabatic transition from 0.5 TeV to 1 TeV cms energy can be made with modest and expected improvements in X-band technology. This allows the collider to begin operation with the greatest of margins in cost and performance, and provides an excellent match to the anticipated physics goals at the energy frontier (Fig. 1.2). Our philosophy is akin to that taken previously in the construction of the SLAC linac which provided a 17-GeV electron beam at its inauguration, was improved to 35 GeV, and with continued advances in S-band technology, now provides 50-GeV electrons and positrons for the SLC.

The NLC design also incorporates multiple paths to further upgrade the cms energy to 1.5 TeV. The “trombone” shape of the collider layout would easily accommodate a straight-forward albeit expensive increase in the length of the main accelerators without requiring extensive modification of the remainder of the complex. This final energy might also be accomplished by development of new, more efficient, X-band technologies; for example, gridded klystrons, cluster klystrons, or relativistic two-beam klystrons.

The highest-level parameters of the NLC are listed in Table 1.3. At each of the nominal 0.5- and 1-TeV cms energies, three sets of parameters define the operating plane of the collider. The expected luminosity is constant over the operating plane, but is achieved with differing combinations of beam current and spot size. This provides a *region* in parameter space where the collider can be operated. Construction and operational tolerances for the various subsystems of the collider are set by the most difficult portion of the operating region. For example, the more difficult parameters for the final focus are those of case (a) in Table 1.3, for which the beam height is smallest. In contrast, preserving the emittance of the beam in the linac is more difficult in case (c), in which the beam charge is highest and the bunch length longest. This design philosophy builds significant margin into the underlying parameters of the collider.

An important element in the design strategy of the NLC is the use of the beam to measure and correct or compensate for errors in electrical and mechanical parameters of the accelerator. These techniques, many in extensive use at the SLC and FFTB, are able to achieve far greater accuracy than is possible during fabrication and installation of components. For example, the use of optical matching and beam-based alignment algorithms considerably loosen tolerances required on magnet strengths and positioning. These procedures require accurate measurement of the properties of the beam and extensive online modeling and control software. The existence of instrumentation suitable for these purposes is an important aspect of the readiness of technologies for the collider.

Additional performance overhead has been included in the designs of most subsystems of the NLC. Errors that we anticipate will occur during machine tuning operations have been taken into account. For example, the injector systems are designed to provide 20% more charge than is indicated in Table 1.3. Fabrication and alignment tolerances for main

Table 1.3: High-level parameters and operating region in parameter space of the NLC.

	NLC-Ia	NLC-Ib	NLC-Ic	NLC-IIa	NLC-IIb	NLC-IIc
Nominal CMS Energy (TeV)		0.5			1.0	
Repetition Rate (Hz)		180			120	
Bunches Pulse		90			90	
Bunch Separation (ns)		1.4			1.4	
Bunch Charge ( $10^{10}$ )	0.65	0.75	0.85	0.95	1.10	1.25
Beam Power (MW)	4.2	4.8	5.5	6.8	7.9	9.0
$\sigma_x$ at IP (nm)	264	294	294	231	250	284
$\sigma_y$ at IP (nm)	5.1	6.3	7.8	4.4	5.1	6.5
$\sigma_z$ at IP ( $\mu\text{m}$ )	100	125	150	125	150	150
Pinch Enhancement H	1.4	1.4	1.5	1.4	1.4	1.5
Beamstrahlung $\delta_E$ (%)	3.5	3.2	3.5	12.6	12.6	12.1
No. Photons per $e^-/e^+$	0.97	1.02	1.16	1.65	1.77	1.74
Max. Beam Energy (GeV)	267	250	232	529	500	468
Luminosity ( $10^{33}$ )	5.8	5.5	6.0	10.2	11.0	10.6
No. Klystrons		4528			9816	
Klystron Peak Power (MW)		50			75	
Pulse Compression Gain		3.6			3.6	
Unloaded Gradient (MV/m)		50			85	
Total Linac Length (km)		17.6			19.1	
Beam Delivery Length (km)		10.4			10.4	
Total Site Length (km)		30.5			30.5	
Total Linac AC Power (MW)		120			193	

linac structures are specified without assuming benefit from certain global tuning methods such as coherent wakefield cancellation. These are powerful techniques in routine practice at the SLC, but our philosophy is to use them only to provide operational margin. We also recognize that the beam-based tuning described above cannot be done with perfect accuracy. For example, we have analyzed the tuning procedure for the final focus and estimated a 30% increase in the spot size at the IP due to errors that we anticipate will occur in measuring and correcting aberrations inherent in the optics. (This is included in Table 1.3.) This layered approach to specification of collider performance is an important part of our design philosophy.

### 1.3.2 Status Report on Technologies for the NLC

Progress in development of X-band rf components has been impressive in recent years. Prototype klystrons now produce 50-MW pulses, over 1.5 microseconds long, with performance characteristics that are correctly modeled by computer codes. The most recent prototype produces 75-MW pulses, one microsecond long. This exceeds the requirements of the initial 0.5-TeV stage of the NLC, and indeed approaches the requirements for 1-TeV cms energy. Tests of rf pulse-compression transformers have exceeded most goals of the NLC, and high-power rf windows and mode converters that allow high-efficiency transfer of power between components have been successfully tested. Examples of some of these results are shown in Fig. 1.7.

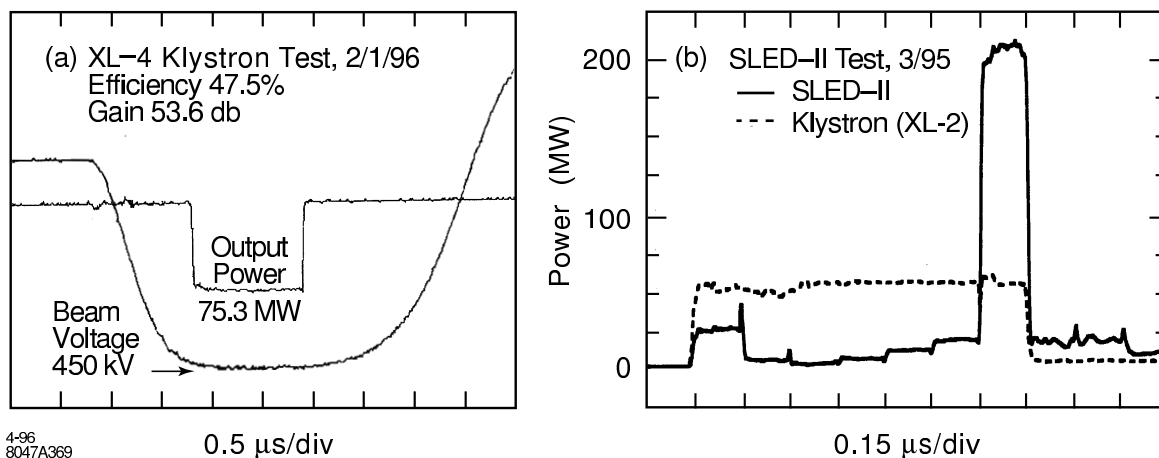


Figure 1.7: Results of tests of X-band rf components: (a) high-power klystrons, and (b) pulse compression systems.

The voltage gradient that can be used in a particle accelerator can be limited by the dark current created when electrons are drawn from the surfaces of the accelerator structures and captured on the accelerating rf wave. For a given rf frequency, there is a well-defined gradient beyond which some electrons emitted at rest will be captured and accelerated to relativistic velocities. This threshold gradient is about 16 MV/m at S-band, and scales to 64 MV/m at

X-band. These are not actual limits to gradients that can be utilized in an accelerator since much of the charge is swept aside by the focusing quadrupoles of the machine lattice, but the dark current will grow rapidly above these values, and may adversely affect the primary beam or interfere with instrumentation needed for tuning. Gradients somewhat above the capture threshold are likely to be useful in practice, but the operational limits are not well known since no large-scale high-performance facility has been operated significantly above capture threshold. Expected thresholds of dark currents in S-band and X-band structures have been confirmed, and it has been proven that (unloaded) gradients as large as 70 MV/m can be used at X-band (Fig. 1.8).

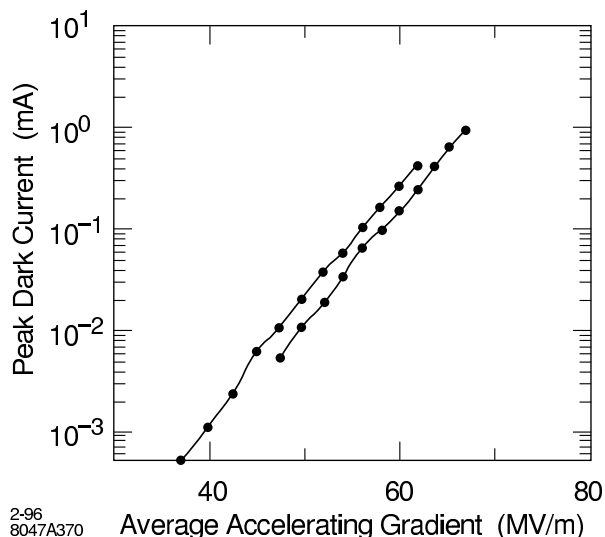


Figure 1.8: Processing of X-band accelerator structures to high gradient.

The electro-mechanical design of the structures of the main accelerator must not only produce the desired gradient, but must also minimize wakefields excited by the passage of the beam. The retarded electromagnetic fields left by each particle can disrupt the trajectories of particles that follow it through the accelerator. Many techniques to control the effects of the short-distance, intrabunch wakefields have been developed, tested, and put into use at the SLC. It will be necessary to also control long-range wakefields at the NLC in order to allow trains of closely spaced bunches to be accelerated on each rf pulse.

Structures in which wakefields are suppressed by careful tuning of their response to the passage of the beam have been developed, and tests have been performed at a facility (ASSET) installed in the SLAC linac (Fig. 1.9). Agreement with theoretical expectations is excellent and lends confidence to the design and manufacture of these structures. A more advanced design that further mitigates the long-range wakefields by coupling deflecting rf modes to external energy-absorbing materials has been completed, and a prototype of this new structure is being readied for testing in ASSET as well.

Work remains to be done on X-band rf technologies, but with prototype components

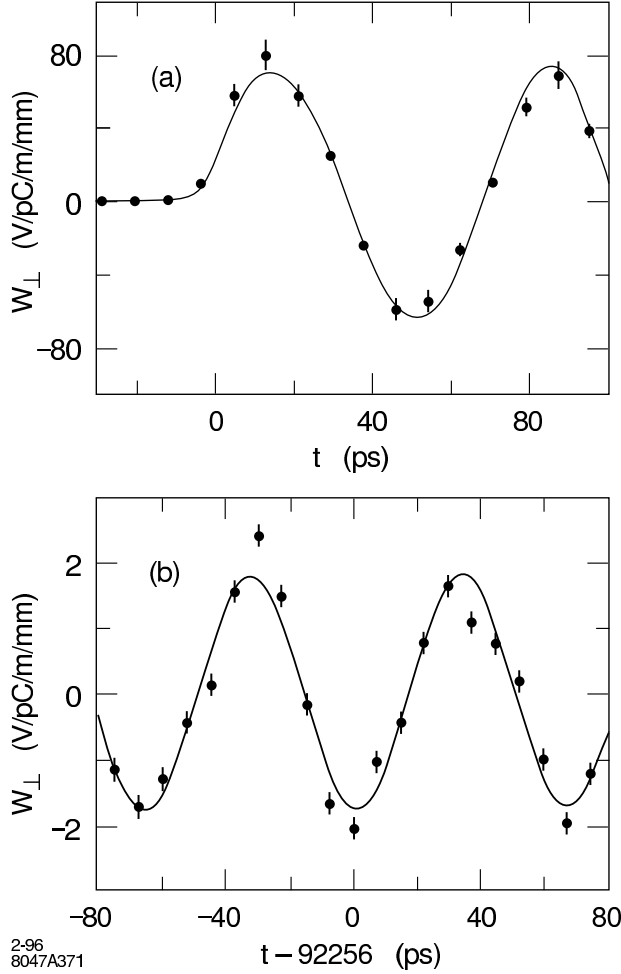


Figure 1.9: Measured and predicted transverse dipole wakefields in a 1.8-m-long X-band accelerator structure.

now in hand, tests of completely integrated systems have begun. A fully engineered test accelerator is under construction at SLAC that will allow optimization of rf systems and provide experience with beam operations at X-band frequencies. This test accelerator will be a 40-m long beam line containing six 1.8-m-long X-band structures powered by 50–75 MW klystrons to an accelerating gradient of 50–85 MV/m. Commissioning of this facility has begun, and operations are expected to be underway by the end of this year (Table 1.2).

The spot sizes that must be produced at the interaction point of the NLC represent significant extrapolations from those achieved at the SLC. It is important to demonstrate that it is possible to demagnify a beam by the large factor needed in the NLC. An experiment has been performed by the Final Focus Test Beam (FFTB) Collaboration to show that such large demagnifications can be achieved. The FFTB is a prototype beam line installed in a channel located at the end of the SLAC linac at zero degrees extraction angle. The FFTB lattice is designed to produce a focal point at which the beam height can be demagnified by

a factor of 380 to reduce the SLC beam ( $\gamma\varepsilon_y = 2 \times 10^{-6}$  m-rad) to a size smaller than 100 nm. The demagnification factor of the FFTB beam line is well in excess of that needed for the NLC.

The FFTB optics are chromatically corrected to third order in the beam energy spread. (The SLC is corrected to second order.) All magnetic elements are mounted on precision stages that can be remotely positioned with step size of about 0.3 micron, and beam-based alignment procedures were developed that successfully place these elements to within 5–15 microns of an ideal smooth trajectory. New state-of-the-art instruments were developed and used to measure the FFTB beam positions and spot sizes. Following a brief shake-down run in August of 1993, data were taken with the FFTB during a three-week period in April and May of 1994. Beam demagnifications of 320 and spot sizes of 70 nm were controllably produced during this period. Measurements of these beams are shown in Fig. 1.10. The design of the NLC final focus follows that of the FFTB, and the experiences gained from the FFTB are incorporated into the tuning strategies for the NLC.

Important advances have also been made in instrumentation required to measure and control properties of the beams. The SLC control system has evolved dramatically over the past years to include extensive online modeling and automation of data analysis and tuning procedures. Scheduled procedures use sets of wire scanners to make complete measurements of the beam phase space, and provide recorded histories of machine performance. Online data-analysis packages are able to reconstruct fully coupled non-linear optical systems. Beam-based feedback and feedforward loops are in routine operation in the SLC with over 100 loops providing control of beam trajectories and energies. Beam position monitors have been developed for the FFTB that achieve pulse-to-pulse resolutions of 1 micron, and new position monitors have recently been installed that are able to measure beam motions of 100 nm. The FFTB focal-point spot monitors have demonstrated techniques to measure beam sizes of 30–40 nm, and extrapolation of these techniques to sizes as small as 10 nm is expected to be successful.

## 1.4 Outlook for the Next Linear Collider

As the SLC has systematically increased its luminosity, the accelerator physics and technologies of linear colliders have matured. Experiences and lessons learned from the task of making this first collider perform as an instrument for particle physics studies make a firm foundation on which to base the design and technology choices for the next linear collider. At the same time, essential demonstrations of new collider technologies have either taken place or soon will be underway. The experimental program with the FFTB is providing the experience needed to evaluate limitations to designs of final focus and interaction regions. The ability to demagnify beams by the amount required for the NLC has already been achieved. Microwave power sources have exceeded requirements for the initial stage of the NLC, and critical tests assure us that this technology can be expected to drive beams to center-of-mass energies of a TeV or more. Fully integrated test accelerators are presently under construction

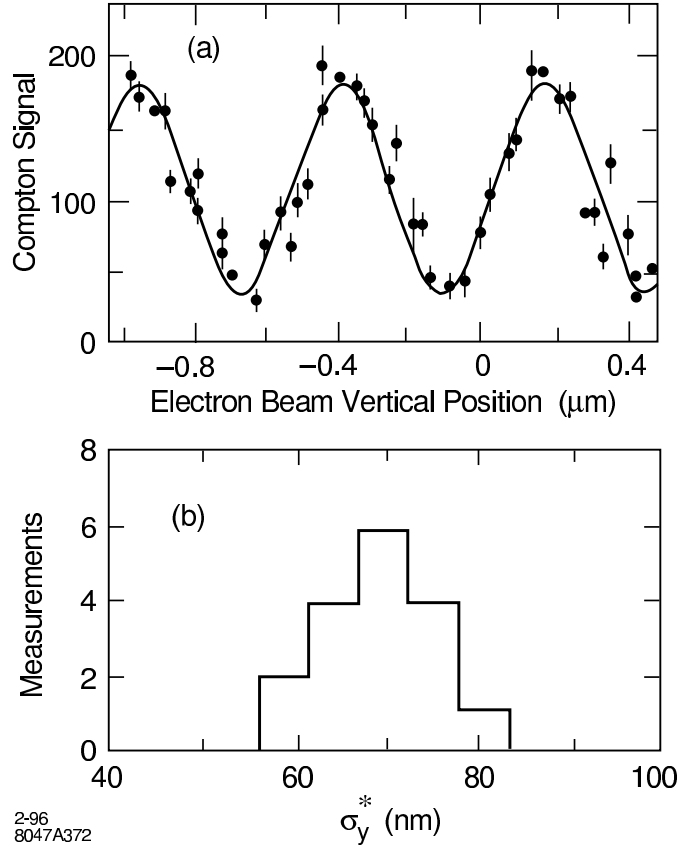


Figure 1.10: Measurement of 70-nm beam spots with a laser-Compton beam size monitor in the FFTB. (a) The rate of Compton scatters from a laser interference pattern used to determine the beam size, in this case 73 nm. (b) Repeatability of spot measurement over periods of several hours.

at CERN, DESY, KEK, and SLAC that will soon provide answers to questions of technical optimization and costs of the major components of a TeV-scale collider.

Given the great international interest and commitment to the goals of a TeV-scale high-performance  $e^+e^-$  collider, it is certain that the final design, construction, and utilization of such a collider will be a global effort. It is important that the scientific community put into place foundations for such a collaboration. The international character of the linear collider project is already reflected in the collaborations at work on the accelerator physics and technology of linear colliders, and in the process of international discussion and review of progress in the field [12]. It is essential that we continue to build on this base of understanding and cooperation, and make certain that all involved in this enterprise are full parties in its final realization.

# Bibliography

- [1] C. Ahn *et al.* SLAC-Report-329, 1988.
- [2] Proceedings of the 1988 DPF Summer Study: Snowmass '88, High Energy Physics in the 1990s, F. Gilman, ed., Snowmass, Colorado, 1988.
- [3] Proceedings of the 1990 DPF Summer Study on High Energy Physics: Research Directions for the Decade, E. F. Berger, ed., Snowmass, CO, 1990.
- [4] Proceedings of the 1987 LaThuile Meeting: Results and Perspectives in Particle Physics, M. Greco, ed., Gif-sur-Yvette, France, 1987.
- [5] Workshop on Electron-Positron Collisions at 500 GeV: The Physics Potential, DESY, 1990.
- [6] Proceedings of the First Workshop on Japan Linear Collider (JLC I), S.Kawabata, ed., KEK, 1989.
- [7] Proceedings of the Second Workshop on Japan Linear Collider (JLC II), KEK, 1990.
- [8] Proceedings of the First International Workshop on Physics and Experiments with Linear Colliders, R. Orava, ed., Saariselka, Finland, 1991.
- [9] Proceedings of the Second International Workshop on Physics and Experiments with Linear Colliders, F. Harris, *et al.*, eds., Waikoloa, Hawaii, 1993.
- [10] Proceedings of the Third International Workshop on Physics and Experiments with Linear Colliders, Iwate, Japan, 1995.
- [11] "Zeroth-Order Design Report for the Next Linear Collider," SLAC Report 474 (Stanford University May 1996).
- [12] International Linear Collider Technical Review Committee Report, 1995, G. Loew, ed. (Available from the editor.)



# Chapter 2

## Physics Goals of the Next Linear Collider

### 2.1 Introduction

During the past several decades, significant advances have been made in elementary particle physics. We now have a renormalizable quantum field theory of strong and electroweak interactions, based on the principle of local  $SU(3)_c \times SU(2)_L \times U(1)_Y$  gauge invariance. That theory properly describes the interactions of all known particles, incorporating the proven symmetries and successes of quantum electrodynamics, the quark model, and low energy V–A theory. It correctly predicted weak neutral currents, the now observed gluons and weak gauge bosons, and the special properties of the heavy fermions  $\tau$ ,  $b$ , and  $t$ . Since it is a renormalizable theory, its predictions can be tested at the quantum loop level by high precision experiments. It has already confronted a wealth of data at the level of 1% or better without any significant evidence of inconsistency. Because of those impressive successes, the  $SU(3)_c \times SU(2)_L \times U(1)_Y$  theory has been given the title “The Standard Model”, a designation which establishes it as the paradigm against which future experimental findings and new theoretical ideas must be compared.

The Standard Model cannot be the final theory of Nature, but it does represent the completion of a major stage toward the uncovering of that theory. To make further progress, we must examine both the strengths and failings of this model and direct experimental effort toward the weakest points in its structure.

The Standard Model is based on the interactions of fermions and vector gauge bosons. The fermions are grouped into three generations of leptons and quarks which span an enormous mass range. Their newest member, the top quark, is exceptionally heavy. Why is the top so massive, or why are the other fermions so light? This question highlights the broader problem of why Nature chose to repeat the fermion generations three times and endow quarks and leptons with their observed pattern of masses and mixing. It is likely that future intense scrutiny of the top quark’s properties will provide new insights regarding this

important problem.

The vector bosons of the Standard Model are grouped into eight massless gluons of  $SU(3)_c$  which mediate the strong interactions, plus the  $W^\pm$ ,  $Z$ , and  $\gamma$  which are responsible for electroweak interactions. The  $SU(3)_c$  gauge theory, called quantum chromodynamics (QCD), taken on its own, is an ideal theory. It has no arbitrary or free parameters but can, in principle, explain all hadronic dynamics including confinement, asymptotic freedom, proton structure, and baryon and meson spectroscopy. Confirming those properties and uncovering additional more subtle features of QCD remains an important experimental and theoretical challenge.

In contrast with QCD, the electroweak sector has many arbitrary parameters. Most stem from the Higgs mechanism which is used to break the  $SU(2)_L \times U(1)_Y$  symmetry and endow particles with mass. In the simplest realization of this symmetry breaking, one introduces a scalar doublet  $\phi$ , the Higgs field, which obtains a vacuum expectation value  $v$ . This assumption introduces into the theory an electroweak mass scale  $v \simeq 250$  GeV. The masses of the  $W$  and  $Z$  bosons and the various quarks and leptons are proportional to  $v$ . Their disparity reflects extreme differences in their couplings to the scalar field  $\phi$ . It is true that this simple model with one Higgs field can parametrize all electroweak masses, quark mixing, and even CP violation. But it does not provide insight into any of these phenomena, or even into the basic fact that the electroweak gauge symmetry is spontaneously broken. The many unanswered questions associated with the Higgs field, or whatever more complicated structure leads to the breaking of the electroweak symmetry, call for experiments which thoroughly explore this sector.

An important testable prediction of the simple Higgs model is the existence of a neutral spin-0 remnant particle  $H$ , called the Higgs scalar. Its mass depends on the self-coupling  $\lambda$  of the Higgs field through the relation

$$m_H = \sqrt{2\lambda}v, \quad (2.1)$$

but it is unspecified as long as  $\lambda$  is unknown. There is an experimental lower bound on  $m_H$  of 65 GeV from direct searches at LEP. That search reach is expected to be extended up to about 90 GeV at LEP II. There is also an approximate upper bound on the Higgs mass  $m_H \lesssim 800$  GeV from theoretical bounds on  $\lambda$ . For example, perturbative partial wave unitarity in high energy scattering of longitudinal  $W$  bosons,  $W_L W_L \rightarrow W_L W_L$  requires  $|\lambda| \lesssim 8\pi/5$ . This gives a large window in which to search. However, there is a much stronger upper bound which comes from the stronger assumption that the Higgs boson is a fundamental particle with no nonperturbative interactions up to the grand unification scale. This requires  $m_H \lesssim 200$  GeV; we will refer to a Higgs boson satisfying this hypothesis as a ‘light Higgs’.

Even more daunting than the problem of finding the Higgs boson  $H$  in the context of the simple Higgs theory is the prospect that this theory is inadequate to correctly describe the weak interaction scale. This simplest theory has theoretical problems of self-consistency, particularly when it is extrapolated to a unified theory at high energies. Also, the fact that its pattern of couplings must be input without any explanation is a sign that this theory is

only a parametrization of electroweak symmetry breaking rather than being a fundamental explanation of this phenomenon. This state of affairs has led to many speculations on the true symmetry breaking mechanism and, from there, to interesting new physics possibilities beyond the Standard Model with observable manifestations at high energy.

In order to build a theory in which electroweak symmetry is naturally broken by the expectation value of a fundamental Higgs field, it is necessary to incorporate supersymmetry (SUSY) at the weak interaction scale. That elegant boson-fermion symmetry allows a simple connection to gauge or string theory unification and provides a logic for the symmetry-breaking form of the Higgs potential. Achieving these goals, however, requires introducing novel partners for all Standard Model particles. It also requires at least two Higgs doublets and thus predicts five remnant scalars,  $h$ ,  $H$ ,  $A$ ,  $H^\pm$ . The  $h$  should have a mass below about 150 GeV and should be most similar to the Standard Model Higgs boson. Finding that particle and determining its properties may be our first window to supersymmetry. If supersymmetry does indeed appear below 1 TeV, there will be a wealth of supersymmetry partner spectroscopy waiting to be explored. Currently, supersymmetry has no direct experimental support. However, there are two very suggestive pieces of evidence that are in favor of this theory. The first is the values of the  $SU(3) \times SU(2) \times U(1)$  coupling constants. These coupling constants are in just the relation predicted by a supersymmetric grand unified theory. The second is the tendency of the precision electroweak data to favor a light Higgs boson, which is an indication that the mechanism of electroweak symmetry breaking involves weakly-coupled fields.

Alternatively, one might imagine that there is no fundamental Higgs field, and that the electroweak symmetry is broken dynamically by fermion-antifermion condensation due to new strong forces at high energy. Scenarios ranging from  $t\bar{t}$  condensation to complex extended technicolor models have been proposed. Their basic premise is very appealing, but no compelling model exists. Nevertheless, the generic idea of new underlying strong dynamics gives rise to testable consequences for anomalous top and gauge boson couplings and high energy scattering behavior.

This issue of whether the mechanism of electroweak symmetry breaking is weak-coupling or strong-coupling is the most important question in elementary particle physics today. The NLC should resolve it definitively. For the case in which this physics is weak-coupling, the NLC should have a rich experimental program involving the detailed study of Higgs bosons and supersymmetric particles. The precise spectrum and branching ratio determinations for these particles should give information which, like the values of the strong and electroweak coupling constants, can be extrapolated to the unification scale. This scenario offers the tantalizing possibility that experimental data collected at the NLC would be directly relevant to supergravity and superstring theories at very high energy. On the other hand, if the mechanism of electroweak symmetry breaking is strong-coupling, this could imply a new spectroscopy at the TeV energy scale which the NLC might access directly.

In addition to these two options which relate directly to the physics of electroweak symmetry breaking, there are many other possibilities for new physics at the TeV energy scale.

These include larger gauge groups with additional  $W'$  and  $Z'$  gauge bosons, heavy new fermions, and additional scalars. Many of these possibilities are realized in specific models of electroweak symmetry breaking, so a broad-based search for new phenomena is an essential part of the experimental program devoted to this question. The most direct way to uncover such new particles and their associated phenomena is to search at very high energies above particle production threshold. Important indirect evidence can also be inferred from precision studies of Standard Model parameters such as  $m_W$ ,  $\sin^2 \theta_W$ , and the couplings of heavy quarks and  $W$  bosons to the  $\gamma$  and  $Z^0$ .

For the exploration of all of these possibilities, which defines the next step in experimental high-energy physics, the Next Linear Collider (NLC) will play an essential role. We envisage this machine as an  $e^+e^-$  collider which operates initially at a center of mass energy of about 500 GeV and can be upgraded to 1.5 TeV, providing a luminosity corresponding to  $10^4$  events per year for a process with the point cross section for QED pair production. This machine will employ polarized electrons and offers the possibility of  $e^-e^-$ ,  $e\gamma$ , and  $\gamma\gamma$  collider options. With such a facility, it is possible to carry out crucial and unique experiments across the whole range of possibilities we have just described for the physics of the weak interaction scale. In this report, we will summarize the capabilities of the NLC to explore the physics of the weak interaction scale across this broad front. A design for the NLC is presented in an accompanying report [1].

In Section 2 of this chapter, we will summarize the basic conclusions of this report relevant to the physics studies, including the basic accelerator parameters of energy and luminosity. We will also describe the basic assumptions on detector performance that we will use to describe the physics capabilities of this machine. In Sections 11 and 12, after our discussion of the physics opportunities that the NLC will provide, we will give a more detailed description of a detector design and the constraints on the detector which come both from the physics goals and from the accelerator.

One of the first physics goals of the NLC will be the detailed study of the top quark at its threshold and just above. We will explain in Section 3 the special features of the  $t\bar{t}$  threshold region which make it a unique laboratory for the precision measurement of the top mass and width, the QCD coupling of the top quark, and the possible couplings to the Higgs boson and other new particles. We will also describe how the NLC will make precision measurements of the couplings of top to electroweak gauge bosons, couplings which might contain signals of new strong interactions which connect top to the sector responsible for electroweak symmetry breaking.

Whether the electroweak gauge symmetry is broken by fundamental Higgs bosons or by new high-energy strong interactions, the NLC will bring important contributions to the experimental study of this sector. First of all, though the LHC and other facilities have the capability to find a light Higgs boson in many decay channels, the NLC is the only planned facility at which the existence of a light Higgs boson can be ruled out in a model-independent way. If the light Higgs boson is indeed present, we will show in Section 4 that the NLC will be able not only to discover this particle but also to characterize many of its interactions.

We will show that the NLC has a unique capability to determine the couplings of the Higgs boson to  $Z$  and  $W$ , to heavy quarks and leptons, and to photons. These measurements dovetail nicely with the expected measurement of the Higgs production cross section from gluon fusion at the LHC to give the complete phenomenological profile of this particle.

If the presence of a relatively light fundamental Higgs particle is accompanied by the appearance of supersymmetry at the TeV scale, the NLC can perform crucial experiments to characterize the new supersymmetric particles. We will show in Section 5 that the NLC can detect the supersymmetric partners of  $W$  and  $Z$  over essentially the complete range of parameters expected in the model. But, even more importantly, the NLC can measure the masses and mixing angles of these particles and, in so doing, determine the most important underlying parameters of supersymmetry. This determination of parameters will be essential not only for the exploration of the physics of fermion partners at  $e^+e^-$  colliders, but also for the extraction of detailed information about the underlying theory from the complementary signatures of supersymmetry seen at hadron colliders.

If electroweak gauge symmetry is broken by new forces at high energy, one can look for the signs of these forces in the couplings of  $W$  bosons to the  $\gamma$  and  $Z$  and in the study of  $WW$  scattering. We will show in Section 6 that the NLC is an ideal machine for the study of the gauge couplings of the  $W$ , capable of achieving parts per mil precision on the  $W$  form factors. We will show in Section 7 that the NLC at the high end of its energy range can achieve constraints on  $WW$  scattering comparable to those of the LHC, in an environment with a number of qualitative advantages. We will also show that the NLC also offers new windows into  $WW$  interactions through the precision study of  $e^+e^- \rightarrow W^+W^-$  and through high-energy  $t\bar{t}$  production.

Finally, these capabilities of the NLC to explore specific models of electroweak symmetry breaking are balanced by the ability of this facility to perform broad searches for novel fermions, scalars, and gauge bosons. We will describe the abilities of the NLC to search for exotic particles in  $e^+e^-$  annihilation in Section 8. In Section 9, we will show how this broad capability is extended further by the availability of  $e^-e^-$ ,  $e\gamma$ , and  $\gamma\gamma$  collisions. In Section 10, we will show that the NLC will also contribute to the future program in the study of the strong interactions, in particular, through the precision measurement of  $\alpha_s$ .

Section 13 will present our conclusions. We will review the unique capabilities of the NLC and contrast its prospects with those of the next generation of hadron colliders.

## 2.2 Standard Model Processes and Simulations

We begin by describing the basic assumptions underlying our study of the physics capabilities of the NLC. We will briefly discuss the expected energy and luminosity that the NLC will provide, the performance of the detector that we expect to have available, our simulation methods, and the magnitudes of the most important standard model background processes.

### 2.2.1 Accelerator and Detector

The NLC is envisaged as the first full-scale  $e^+e^-$  linear collider, a machine designed from the beginning with the goal of high-luminosity colliding beam physics and one which takes account of the lessons of its prototype, the SLC. The NLC will be designed for an initial energy of 500 GeV in the center of mass, with an upgrade path to 1.5 TeV. It will provide a luminosity sufficient for a thorough experimental program on  $e^+e^-$  annihilation to standard and exotic particle pairs. It will provide a highly polarized  $e^-$  beam, and possibly also a polarized positron beam. Our basic assumptions on luminosity as a function of energy and on polarization are given in Table 2.1. These assumptions are justified in the description of the accelerator design given in Chapter 3 of this report and, at greater length, in [1].

Table 2.1: Basic Parameters of the Next Linear Collider

Energy (GeV)	Luminosity ( $\text{cm}^{-2}\text{s}^{-1}$ )	
500 GeV	$5 \times 10^{33}$	
1000 GeV	$1 \times 10^{34}$	
1500 GeV	$1 \times 10^{34}$	
Polarization:	80% $e^-$ , 0% $e^+$	Initial
	90% $e^-$ 65% $e^+$	Possible

The NLC experiments can be carried out with a standard  $4\pi$  multipurpose detector similar to those at LEP or SLC. In our concept of this detector, we include some innovations such as all-silicon tracking to minimize the effect of machine-related backgrounds, but for the most part the demands we have made on the detector are straightforwardly met. The essential performance assumptions we have made are shown in Table 2.2. Because of the small beam spot sizes at a linear collider, which allows us to bring a CCD vertex detector within 2 cm of the interaction point, the detector should have excellent  $b$ -tagging capabilities. The assumed curve of efficiency versus purity for  $b$ -tagging is shown in Fig. 2.1; the performance required has already been demonstrated in the SLD vertex detector.

Table 2.2: Summary of the detector parametrization used in the simulations. Smeared quantities are denoted in the table by a subscript  $s$ .

Particle	Energy	Momentum
Electrons	$\frac{\delta E}{E} = \frac{12\%}{\sqrt{E}} + 1.0\%$ $E_s = E + \delta E$	$P_s^2 = E_s^2 - m_e^2$
Photons	$\frac{\delta E}{E} = \frac{12\%}{\sqrt{E}} + 1.0\%$ $E_s = E + \delta E$	$P_s = E_s$
Neutral Hadrons	$\frac{\delta E}{E} = \frac{45\%}{\sqrt{E}} + 2.0\%$ $E_s = E + \delta E$	$P_s^2 = E_s^2 - m_\pi^2$
Charged Hadrons	$E_s^2 = P_s^2 + m_\pi^2$	$\frac{\delta P_{x,y}}{P_{x,y}^2} = 0.0005 \oplus \frac{0.0015}{P_{x,y}\sqrt{P}(\sin\theta)^{2.5}}$ $\frac{\delta P_z}{P_z^2} = \frac{0.0015}{P_{x,y}\sqrt{P}(\sin\theta)^{2.5}}$ $(P_s)_i = P_i + \delta P_i$

## 2.2.2 Simulations

In the studies presented here, the detector model has been used in concert with a set of familiar and newly-written simulation programs. In general, the background processes were generated by PYTHIA 5.7 [2], except for the background from  $e^+e^- \rightarrow W^+W^-$ , which plays an especially important role at linear collider energies. For this process we used a new generator [3] which is based on the formalism for this reaction presented by Hagiwara *et al.* [4]. This generator computed the total amplitude for  $W^+W^-$  production and subsequent decay to four fermions, retaining the full spin correlations through the process. It did make the approximation of treating the  $W$ 's as on-shell particles, but it properly treated the effects of initial state electron polarization, beamstrahlung, collinear multi-photon initial state bremsstrahlung, and a nonzero  $W$  boson decay width. The same Monte Carlo program was used in the studies of nonstandard  $W$  physics reported in Sections 6 and 7. Many of the other analyses used specialized generators at this level of sophistication to simulate the new physics processes. These are described in the various sections of this report. Except where it is reported otherwise, the hadronization of partons and subsequent decays were performed by JETSET 7.4 [2].

Four-vectors of stable particles emerging from the simulated reaction were adjusted by a detector resolution smearing routine, which implemented the parametrization summarized in Table 2.2. All quantities were parametrized as a function of theta. The smearing assumed Gaussian errors and populated tails out to  $3.5\sigma$ . The parametrization assumed a dead cone about the beampipe of 150 mrad ( $\cos\theta = 0.99$ ). The neutral particle and charged

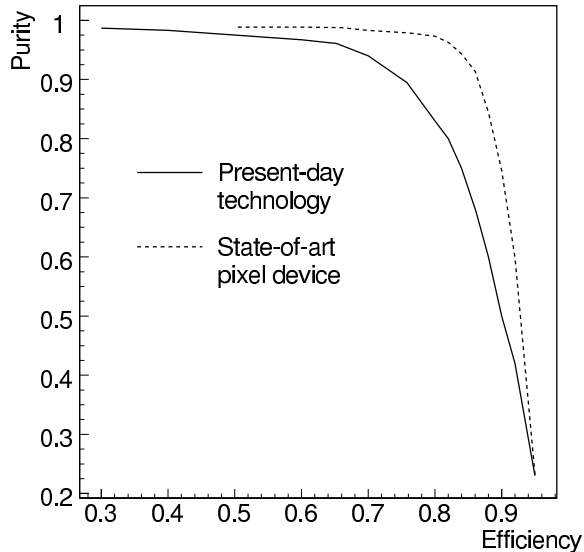


Figure 2.1: Efficiency versus purity relation for  $b$ -tagging with the NLC detector.

particle detection efficiencies were each taken to be 98%. For neutral hadrons, the momentum directions were Gaussian smeared in a cone about the original direction with a half-width of 15 mrad to simulate finite directional resolution. For photons and electrons, the directions were smeared by a cone of half-width 10 mrad.

### 2.2.3 Standard Model Processes at the NLC

Standard model processes, in addition to being interesting in their own right, are the background to searches for new physics at the NLC. Many of the standard model reactions at the NLC are familiar at lower energies and need only be extrapolated to higher energies. However, new processes, such as the pair production of gauge bosons, emerge as dominant reactions.

The cross sections of Standard Model processes at an  $e^+e^-$  collider are shown as a function of center of mass energy in Fig. 2.2 [5]. From left to right across this plot, the familiar  $e^+e^-$  annihilation processes fall with energy according to the point cross section for  $e^+e^- \rightarrow \mu^+\mu^-$  in QED,

$$\sigma = \frac{4\pi\alpha^2}{3s} = \frac{87 \text{ fb}}{s (\text{TeV}^2)}. \quad (2.2)$$

At the same time, new processes involving pair production and multiple production of weak interaction vector bosons become important.

Another view of the standard model backgrounds is given in Fig. 2.3, where the cross sections for the dominant  $e^+e^-$  annihilation processes are shown as a function of the degree of longitudinal polarization. The curves were calculated using ISAJET 7.13 [6]. The peripheral

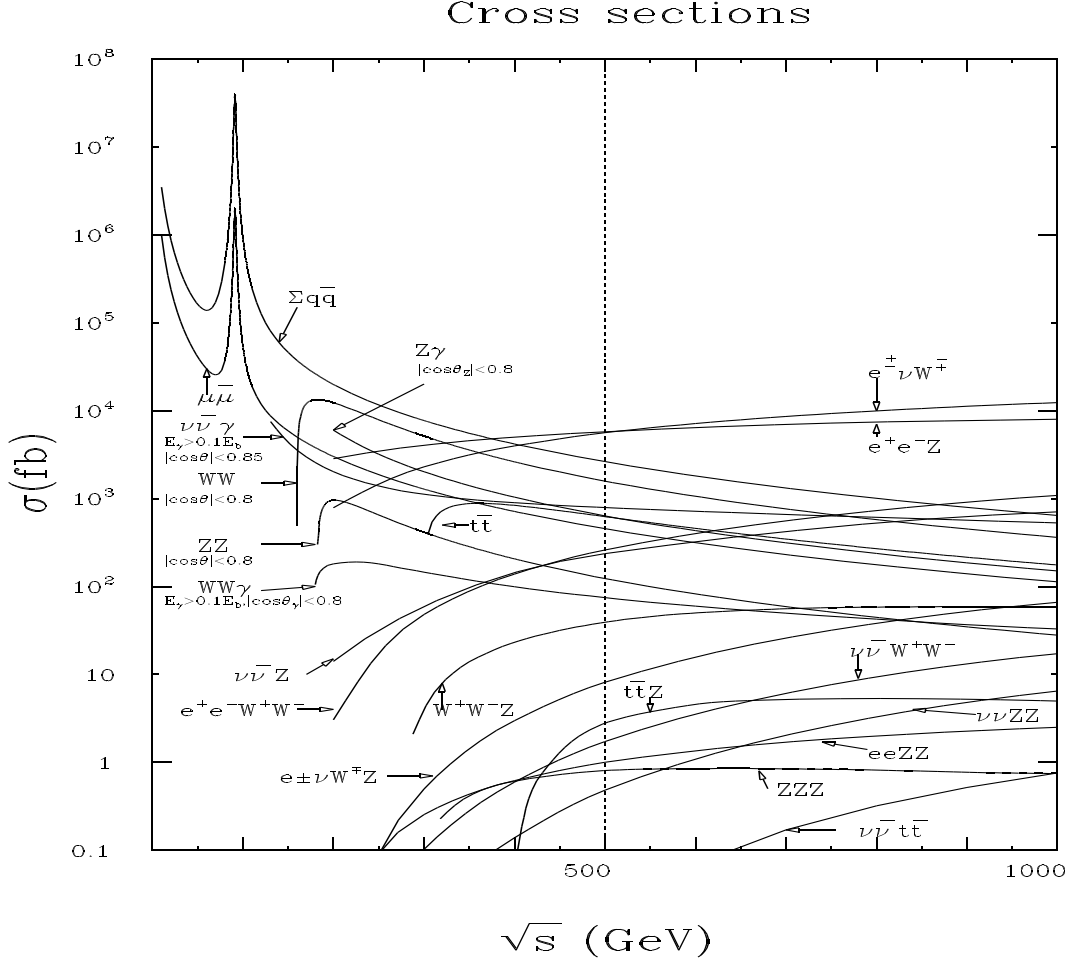


Figure 2.2: Cross sections for Standard Model physics processes in  $e^+e^-$  annihilation, as a function of center of mass energy, from [5].

two photon, t-channel Bhabha scattering and  $e^+e^- \rightarrow Z^0\gamma$  processes are not shown; the cross sections for these reactions are relatively independent of polarization. The reactions  $e^+e^- \rightarrow e^+\nu W^-, e^-\bar{\nu}W^+, e^+e^-Z^0$  are also not shown. The first of these is present only for left-handed  $e^-$ ; the other two depend only weakly on  $e^-$  beam polarization. The most troublesome source of background in many of the physics analyses is the reaction  $e^+e^- \rightarrow W^+W^-$ , whose special role we have already pointed out. It is noteworthy that the cross section for this process can be reduced substantially by adjusting the electron beam polarization.

Cuts on other quantities, such as the acoplanarity and production angle will also be useful for removing standard model background. The distributions in these variables for standard model annihilation processes are shown in Figs. 2.4 and 2.5.

In general, the two photon and  $e^+e^- \rightarrow Z^0\gamma$  processes are not important as backgrounds to annihilation processes because they may be removed easily from the data sample by low transverse momentum and multiplicity cuts [7]. The cross section for Bhabha scattering is

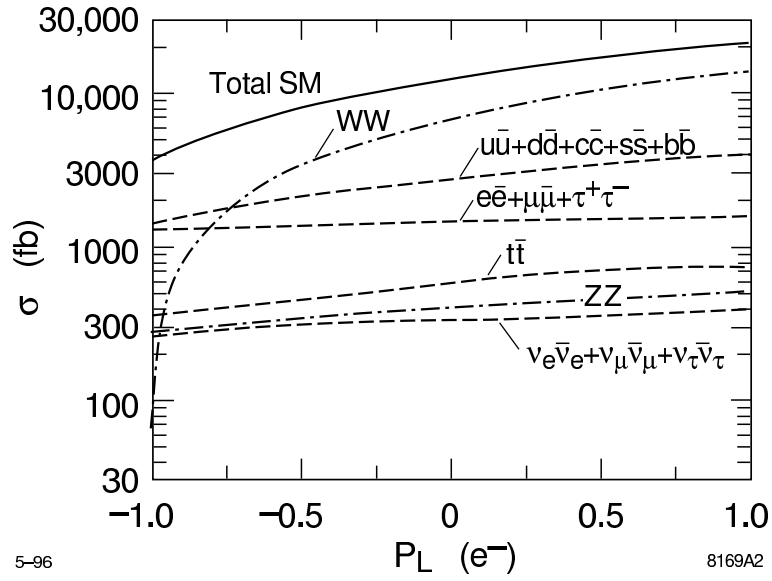


Figure 2.3: Cross sections for Standard Model physics processes in  $e^+e^-$  annihilation at 500 GeV, as a function of the electron longitudinal polarization.

very large in the forward direction but drops to a few units of R at large angles.

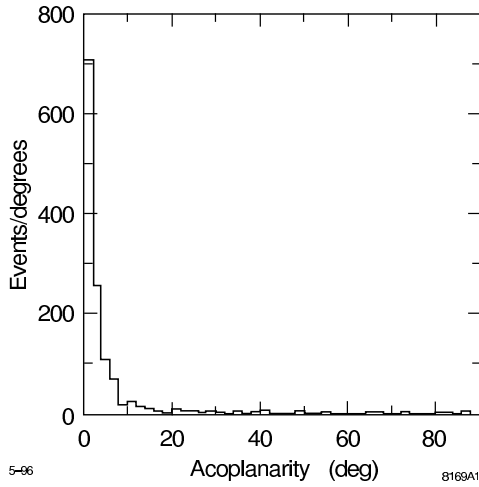


Figure 2.4: Expectation for the acoplanarity distribution in  $e^+e^- \rightarrow W^+W^-$  events in which both  $W$  bosons decay to hadrons.

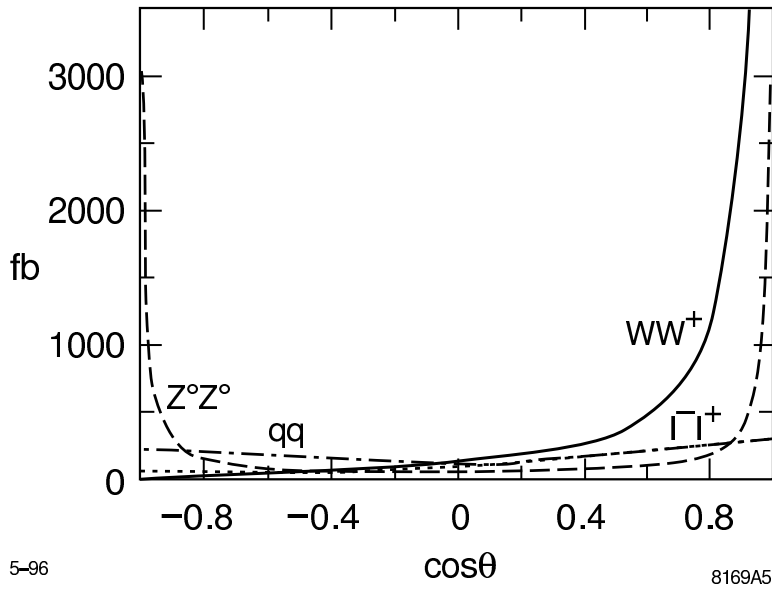


Figure 2.5: Expectation for the  $\cos \theta$  distribution due to standard model processes.

## 2.3 Top Quark Physics

The stage for the future of top physics has been set by the recent discovery [8] of top at Fermilab. The very large top mass,  $m_t \approx 174 \pm 8 \text{ GeV}/c^2$ , forces one to consider the possibility that the top quark plays a special role in particle physics. At the very least, the properties of the top quark could reveal important information about the physics of electroweak symmetry breaking. In this context, the determination of the complete set of top quark properties should be an important goal. A high-energy future linear  $e^+e^-$  collider provides a very impressive tool to carry out a detailed top quark physics program.

The  $t\bar{t}$  threshold region has a rich phenomenology which derives from its mix of toponium and continuum structure. Only in  $e^-e^+$  collisions can this threshold structure be properly resolved, making possible definitive measurements of the top mass and width and tests of the QCD potential at very short range. Above threshold, the NLC makes it possible to measure the complete set of top couplings to gauge bosons, both for neutral current ( $\gamma$  and  $Z^0$ ) and charged current interactions. The high electron-beam polarization available at NLC plays an important role in such studies, simplifying the search for anomalous top couplings and CP violating effects. A complete understanding of electroweak symmetry breaking will require the measurement of the Higgs boson couplings to fermions; of these, the coupling to top is the most accessible. At the NLC, this quantity can be measured by direct  $t\bar{t}H$  production above threshold and also, if the Higgs boson is light, by the effect of Higgs boson exchange on the threshold properties. Finally, the NLC provides a relatively clean final state and precise vertex detection which make it straightforward to study the decays of the top. All standard decay modes can be reconstructed with reasonable efficiency, and exotic decay modes, in those examples studied to date, can be readily identified.

The physics program for the top quark also imposes important constraints on the NLC design. The energy must be adjustable, to run both at the  $t\bar{t}$  threshold and at a point in the continuum about 100 GeV above threshold. The study of the threshold region requires that the center-of-mass energy spread be much smaller than the top quark width, and that tails in the energy distribution be understood. Experimenters must be able to determine both the absolute energy and the differential luminosity spectrum.

### 2.3.1 Top Production, Decay, and Measurement

The large mass of the top quark causes it to have a very large decay width, and this exerts a decisive influence on its phenomenology. In the Standard Model, the weak decay of top proceeds very rapidly via  $t \rightarrow bW$ , resulting in a total decay width given by

$$\Gamma_t \approx (0.18)(m_t/m_W)^3 \text{ GeV} . \quad (2.3)$$

For  $m_t = 180 \text{ GeV}/c^2$  this lowest-order prediction is  $\Gamma_t = 1.71 \text{ GeV}$ . After first-order QCD and electroweak corrections [9], this becomes 1.57 GeV. Hence, top decay is much more rapid than the characteristic time for hadron formation, for which the scale is  $\Lambda_{\text{QCD}}$ . This implies

that the phenomenology of top physics is fundamentally different than that of the lighter quarks. For example, there will be no top-flavored mesons. While we lose the familiar study of the spectroscopy of these states, we gain unique clarity in the ability to reconstruct the properties of the elementary quark itself. This may prove to be a crucial advantage toward uncovering fundamental issues.

The top decay also provides a natural cutoff for gluon emission. Indeed, in  $t\bar{t}$  processes, the nonperturbative color strings appear in fragmentation only after the tops decay and form along the separating  $b$  and  $\bar{b}$  lines. Hard gluons emitted from the top and its product bottom quark can exhibit interference phenomena which are sensitive to the value of  $\Gamma_t$  [10, 11].

In the Standard Model,  $|V_{tb}| \approx 1$ , so that the decay mode  $t \rightarrow bW$  completely saturates the decay width. Then the branching ratios are determined by the  $W$  decay modes from the  $b\bar{b}W^+W^-$  intermediate state. This gives 6-jet, 4-jet + lepton, and 2-lepton final states in the ratio 4:4:1, or, including QCD corrections to the  $W$  decay rates,  $\text{BR}(t\bar{t} \rightarrow b\bar{b}qq'qq') = 0.455$ ;  $\text{BR}(t\bar{t} \rightarrow b\bar{b}qq'\ell\nu) = 0.439$ ;  $\text{BR}(t\bar{t} \rightarrow \ell\nu\ell\nu) = 0.106$ , where  $q = u, c$ ,  $q' = d, s$ , and  $\ell = e, \mu, \tau$ .

The parton-like decay of top implies that, unlike other quarks, its spin is transferred to a readily reconstructable final state. Measurement of the  $b\bar{b}W^+W^-$  final state therefore provides a powerful means of probing new physics manifested by top with helicity analyses. This is explored in Section 2.3.3. Another implication of the large  $m_t$  is the Standard Model prediction that the decay  $t \rightarrow bW$  produces mostly longitudinally polarized  $W$  bosons; the degree of longitudinal polarization is given by  $m_t^2/(m_t^2 + 2m_W^2) \approx 72\%$  for  $m_t = 180 \text{ GeV}/c^2$ . This reflects the fact that the longitudinally polarized  $W$  bosons contain degrees of freedom from the electroweak symmetry breaking sector.

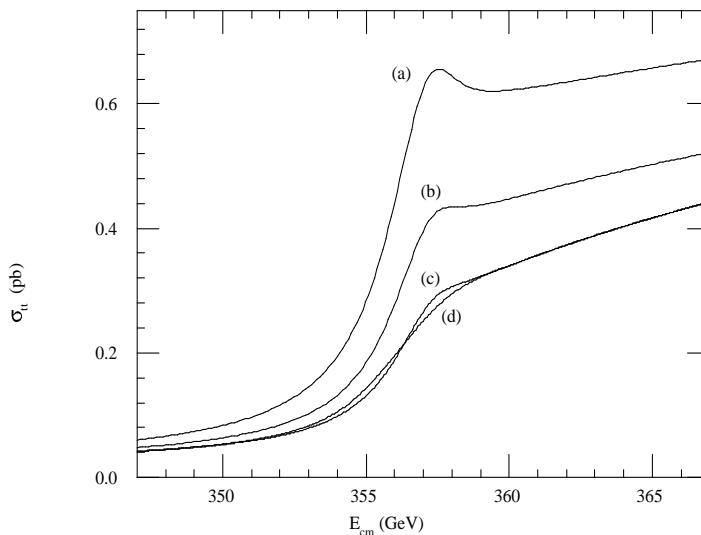


Figure 2.6: Production cross section for top-quark pairs near threshold for  $m_t = 180 \text{ GeV}/c^2$ . The ideal theoretical cross section is given by curve (a). In curves (b), (c) and (d), we add, successively, the effects of initial-state radiation, beamstrahlung, and beam energy spread.

The  $t\bar{t}$  cross section due to  $s$ -channel  $e^+e^-$  annihilation mediated by  $\gamma, Z$  bosons increases abruptly just below threshold (see Fig. 2.6), reaches a maximum at roughly 50 GeV above threshold, then falls roughly proportional to the point cross section, Eq. 2.2, as the energy increases. At  $\sqrt{s} = 500$  GeV the lowest-order total cross section for unpolarized beams is 0.54 pb; it is 0.74 (0.34) for a fully left-hand (right-hand) polarized electron beam. Hence, in a design year of integrated luminosity ( $50 \text{ fb}^{-1}$ ) at  $\sqrt{s} = 500$  GeV we can produce 25,000  $t\bar{t}$  events. The cross sections for  $t$ -channel processes, resulting, for example, in final states such as  $e^+e^-t\bar{t}$  or  $\nu\bar{\nu}t\bar{t}$ , increase with energy, but are still relatively small. We will discuss these processes in Section 7.3.

The emphasis of most event selection strategies has been to take advantage of the multi-jet topology of the roughly 90% of  $t\bar{t}$  events with 4 or 6 jets in the final state. Therefore, cuts on thrust or number of jets drastically reduces the light fermion pair background. In addition, one can use the multi-jet mass constraints  $M(\text{jet-jet}) \approx m_W$  and  $M(3\text{-jet}) \approx m_t$ . Simulation studies [12] have shown that multi-jet resolutions of 5 GeV/ $c^2$  and 15 GeV/ $c^2$  for the 2-jet and 3-jet masses, respectively, are adequate and readily achievable with LEP/SLC detectors. A detection efficiency of about 70% with a signal to background ratio of 10 was attained by selecting 6-jet final states just above threshold. These numbers are typical also for studies which select the 4-jet+ $\ell\nu$  decay mode.

Of the backgrounds considered in this study, that from  $W$ -pair production is the most difficult to eliminate. However, in the limit that the electron beam is fully right-hand polarized, the  $W^+W^-$  cross section is dramatically reduced. Thus it is possible to use the beam polarization to experimentally control and measure the background. We note, though, that the signal is also somewhat reduced by running with a right-handed polarized beam. A possible strategy might be to run with a right-handed polarized beam only long enough to make a significant check of the background due to  $W$  pairs. Another important technique is that of precision vertex detection. The present experience with SLC/SLD can be used as a rather good model of what is possible at NLC. The small and stable interaction point, along with the small beam sizes and bunch timing, make the NLC ideal for pushing the techniques of vertex detection. This has important implications for top physics. Rather loose  $b$ -tagging, applied in conjunction with the standard topological and mass cuts mentioned above, should lead to substantially improved top event selection efficiencies and purities.

### 2.3.2 Threshold Physics

In Fig. 2.6 we show the cross section for  $t\bar{t}$  production as a function of nominal center-of-mass energy for  $m_t = 180 \text{ GeV}/c^2$ . In this discussion,  $m_t$  is the pole mass in QCD perturbation theory. The theoretical cross section, indicated as curve (a), is based on the results of Strassler and Peskin [13], using the  $q\bar{q}$  potential of QCD with  $\alpha_s(M_Z^2) = 0.12$  and Standard Model couplings to  $\gamma$  and  $Z$ . To this curve, the energy-smearing mechanisms of initial-state radiation, beamstrahlung, and beam energy spread, have been successively applied; curve (d) includes all effects. The beam effects were calculated using NLC design parameters.

The threshold enhancement given by the predicted cross section curve of Fig. 2.6a reflects the Coulomb-like attraction of the produced  $t\bar{t}$  state due to the short-distance QCD potential

$$V(r) \sim -C_F \frac{\alpha_s(\mu)}{r}, \quad (2.4)$$

where  $C_F = 4/3$  and  $\mu$  is evaluated at the scale of the Bohr radius of this toponium atom:  $\mu \sim \alpha_s m_t$ . The level spacings of the QCD potential, approximately given by the Rydberg energy,  $\sim \alpha_s^2 m_t$ , turn out to be comparable to the widths of the resonance states, given by  $\Gamma_\theta \approx 2\Gamma_t$ . Thus, the bound state exists, on average, only for approximately one classical revolution before one of the top quarks undergoes a weak decay. The level spacings of the QCD potential approximately given by the Rydberg energy,  $\sim \alpha_s^2 m_t$ , turn out to be comparable to the widths of the resonance states, given by  $\Gamma_\theta \approx 2\Gamma_t$ . Therefore the various toponium states become smeared together, as seen in Fig. 2.6, where only the bump at the position of the 1S resonance is distinguishable. The infrared cutoff imposed by the large top width also implies [14] that the physics is independent of the long-distance behavior of the QCD potential. The assumed intermediate-distance potential is also found [12] to have a negligible impact. Hence, the threshold physics measurements depend only on the short-distance potential (Eq. 2.4) of perturbative QCD.

An increase of  $\alpha_s$  deepens the QCD potential, thereby increasing the wave function at the origin and producing an enhanced 1S resonance bump. In addition, the binding energy of the state varies roughly as the Rydberg energy  $\sim \alpha_s^2 m_t$ . So the larger  $\alpha_s$  has the combined effect of increasing the cross section as well as shifting the apparent position of the threshold to lower energy. The latter effect is also what is expected for a shift to lower  $m_t$ . Therefore, there exists a significant correlation between the measurements of  $\alpha_s$  and  $m_t$  from a threshold scan.

A number of studies have been carried out to simulate the measurement of the  $t\bar{t}$  threshold cross section. Figure 2.7a depicts a threshold scan [12] for which an integrated luminosity of  $1 \text{ fb}^{-1}$  has been expended at each of 10 energy points across the threshold, plus one point below threshold to measure backgrounds. A value of  $m_t = 150 \text{ GeV}/c^2$  was used. No beam polarization was assumed. A fit of the data points to the theoretical cross section, including all radiative and beam effects discussed above, results in a sensitivity for the measurement of  $m_t$  and  $\alpha_s$  shown in Fig. 2.7b. The correlation between these two parameters is apparent. Even for the modest luminosity assumed here, the cross section measurement gives quite good sensitivity to these quantities. If no prior knowledge is assumed, the errors for  $m_t$  and  $\alpha_s$  are  $200 \text{ MeV}/c^2$  and  $0.005$ , respectively. Conversely, the single-parameter sensitivity for  $m_t$  approaches  $100 \text{ MeV}/c^2$  if  $\alpha_s$  is known to much better than 2% accuracy. We will describe a method for the precision measurement of  $\alpha_s$  in Section 10.1. The theoretical systematic error due to uncertainties in the  $t\bar{t}$  threshold cross section is of order 200 MeV.

For a quarkonium state, we expect the cross section at the 1S peak to vary with the total width roughly as  $\sigma_{1S} \sim |V_{tb}|/\Gamma_t$ , and therefore is very sensitive to the width, as indicated in Fig. 2.8 for rather wide variations in  $\Gamma_t$  relative to the Standard Model expectation. (It is noted that the calculations of Figs. 2.6 and 2.8 use the uncorrected top width, so that the

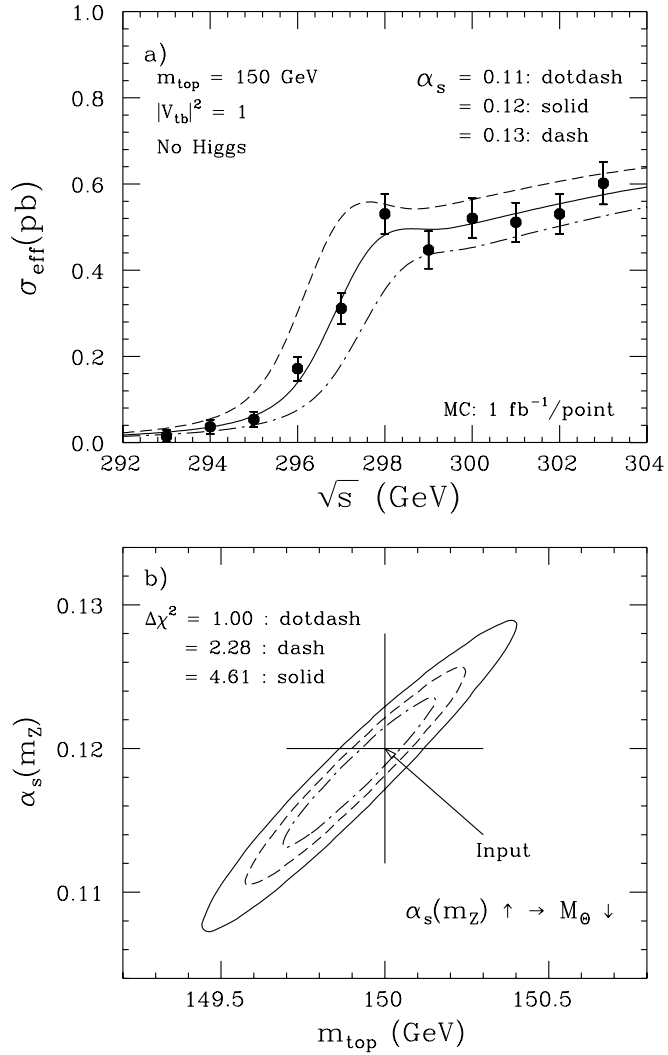


Figure 2.7: (a) Top threshold scan; (b) corresponding error ellipse for  $m_t$  and  $\alpha_s$ . A value for  $m_t$  of 150 GeV/ $c^2$  was assumed.

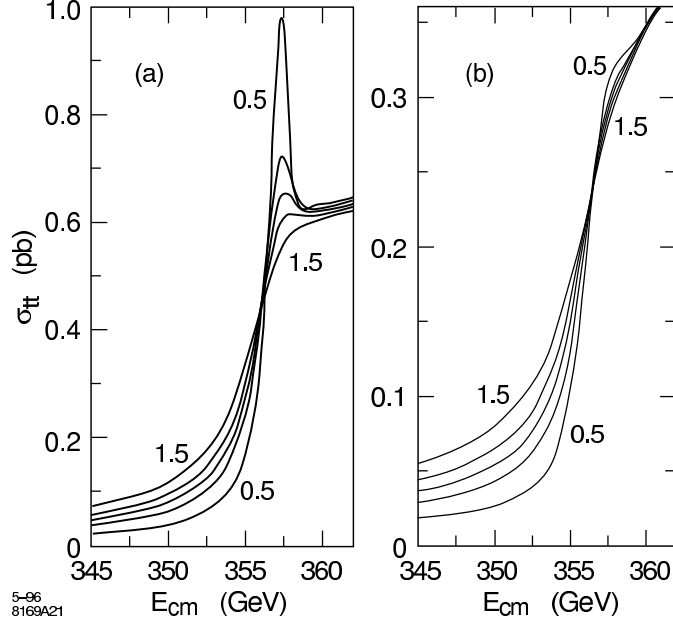


Figure 2.8: Variation of the  $t\bar{t}$  threshold cross section with the top width for  $m_t = 180 \text{ GeV}/c^2$ . The curves correspond to values of  $\Gamma_t/\Gamma_{SM}$  of 0.5, 0.8, 1.0, 1.2, and 1.5, presented in the order indicated, for (a) the theoretical cross section, and (b) the cross section after including radiative and beam effects.

resonance structure will be slightly more pronounced than what is shown.) After applying a correction for initial-state radiation and the beam-related energy spread, the width is affected as shown in Fig. 2.8. This implies that a scan strategy optimized for measuring  $\Gamma_t$  would spend a relatively large fraction of running time below the 1S peak. The threshold physics, combining the cross section information with the momentum and asymmetry results, as discussed below, represents what is most likely the best opportunity to measure  $\Gamma_t$ .

In addition to the QCD potential, the  $t\bar{t}$  pair is also subject to the Yukawa potential associated with Higgs exchange:

$$V_Y = -\frac{\lambda^2}{4\pi} \frac{e^{-m_H r}}{r}, \quad (2.5)$$

where  $m_H$  is the Higgs mass and  $\lambda$  is the  $t\bar{t}$ -Higgs Yukawa coupling,  $\lambda = m_t/v = [\sqrt{2}G_F]^{1/2} m_t$ . Because of the extremely short range of the Yukawa potential, its effect is primarily to alter the wave function at the origin, and hence to shift the level of the cross section. This exciting possibility is discussed further in Section 2.3.4. The physics of the threshold cross section is, in summary, expected to depend on the following set of parameters:

$$\sigma = \sigma(m_t, \alpha_s, \Gamma_t, m_H, \lambda). \quad (2.6)$$

As we have discussed, the lifetime of the toponium resonance is determined by the first top quark to undergo weak decay, rather than by the annihilation process. This has the interesting implication that the kinetic energy (or momentum) of the top quark as reconstructed from its decay products reflects the potential energy of the top in the QCD potential. Hence, a measurement of the momentum distribution will be sensitive to  $\alpha_s$  and  $\Gamma_t$ . The theory [15] and phenomenology [12, 16] of this physics has been extensively studied. A convenient observable which has been used to characterize the distribution is the position of the peak in the reconstructed top quark momentum distribution. The position of this peak at a given center-of-mass energy is indeed found to be sensitive to  $\Gamma_t$  and the other parameters in Eq. 2.6.

Yet another, quite different observable has been studied [17, 12] to help further pin down the physics parameters at threshold. Top is produced symmetrically when produced in the 1S state. The vector coupling of  $t\bar{t}$  to the  $\gamma$  and  $Z$  can create S- and D-wave resonance states. On the other hand, the axial-vector coupling of the top quark to the  $Z$  gives rise to P-wave resonance states. Hence, there is naturally interference between S- and P-waves which gives rise to a forward-backward asymmetry ( $A_{FB}$ ) proportional to  $\beta \cos\theta$ . Because of the large width of the resonance states, due to the large  $\Gamma_t$ , these states do overlap to a significant extent, and a sizable  $A_{FB}$  develops. The value of  $A_{FB}$  varies from about 5% to 12% across the threshold, with the minimum value near the 1S resonance. Since the top width controls the amount of S-P overlap, we expect the forward-backward asymmetry to be a sensitive method for measuring  $\Gamma_t$ .

In summary, a data set of  $50 \text{ fb}^{-1}$  at threshold would provide sensitivity to  $m_t$  and  $\alpha_s$  at the level of  $120 \text{ MeV}/c^2$  and  $0.0025$ , respectively. Similarly, the sensitivity to the total top decay width is 5–10%. Accelerator and detector designs have become sufficiently stable to make possible calculations which incorporate the systematics associated with luminosity spectra and backgrounds. This would allow better determination of the limiting systematic errors at threshold, which are presently estimated to be at or below the sensitivities above. The measurement of the luminosity spectrum is discussed in more detail in Section 13.

### 2.3.3 Top Couplings

At the NLC,  $e^+e^- \rightarrow t\bar{t}$  above threshold will provide a unique opportunity to measure simultaneously all of the top couplings. Due to its rapid weak decay, the top spin is transferred directly to the final state with negligible hadronization uncertainties, therefore allowing the helicity-dependent information contained in the Lagrangian to be propagated to the final state. This final state, expected to be dominated by  $bW^+\bar{b}W^-$ , can be fully reconstructed with good efficiency and purity, so that a complete helicity analysis can be performed.

The top neutral-current coupling can be generalized to the following expression for the  $Zt\bar{t}$  or  $\gamma t\bar{t}$  vertex factor:

$$\mathcal{M}^{\mu(\gamma,Z)} = e\gamma^\mu \left[ Q_V^{\gamma,Z} F_{1V}^{\gamma,Z} + Q_A^{\gamma,Z} F_{1A}^{\gamma,Z} \gamma^5 \right] + \frac{i e}{2m_t} \sigma^{\mu\nu} k_\nu \left[ Q_V^{\gamma,Z} F_{2V}^{\gamma,Z} + Q_A^{\gamma,Z} F_{2A}^{\gamma,Z} \gamma^5 \right]. \quad (2.7)$$

This expression reduces to the familiar Standard Model tree level expression when we set the form factors to  $F_{1V}^\gamma = F_{1V}^Z = F_{1A}^Z = 1$ , with all others zero. The quantities  $Q_{A,V}^{\gamma,Z}$  are the usual SM coupling constants:  $Q_V^\gamma = \frac{2}{3}$ ,  $Q_A^\gamma = 0$ ,  $Q_V^Z = (1 - \frac{8}{3} \sin^2 \theta_W)/(4 \sin \theta_W \cos \theta_W)$ , and  $Q_A^Z = -1/(4 \sin \theta_W \cos \theta_W)$ . The non-standard couplings  $F_{2V}^{\gamma,Z}$  and  $F_{2A}^{\gamma,Z}$  correspond to the electroweak magnetic and electric dipole moments, respectively. While these couplings are zero at tree level in the Standard Model, the analog of the magnetic dipole coupling is expected to attain a value of order  $\alpha_s/\pi$  due to corrections beyond leading order. On the other hand, the electric dipole term violates CP and is expected to be zero in the Standard Model through two loops [18]. Such a non-standard coupling necessarily involves a top spin flip, hence is proportional to  $m_t$ .

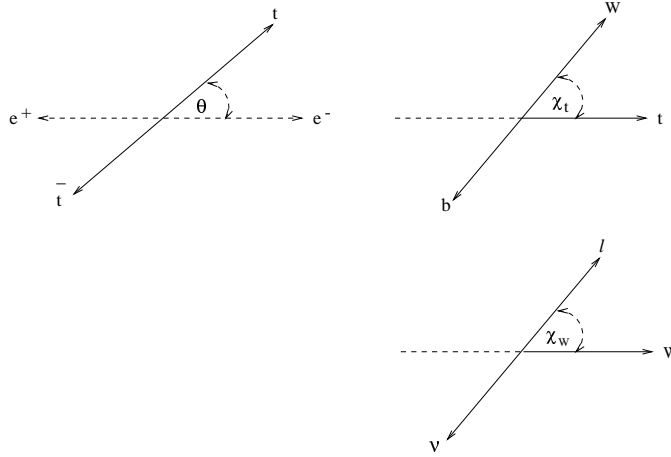


Figure 2.9: Definitions of helicity angles. (a) Production angle  $\theta$  in  $t\bar{t}$  rest frame; (b)  $\chi_t$  measured in the top rest frame as shown; and (c)  $\chi_W$  in the  $W$  rest frame.

The form factors can be measured through their distinct dependencies on the helicities of the  $e^-$ ,  $e^+$ ,  $t$ , and  $\bar{t}$ , which can be accessed experimentally through the beam polarization and the angular distributions in the final state. The production and decay angles can be defined as shown in Fig. 2.9. The angle  $\chi_W$  is defined in the  $W$  rest frame. The analogous statement holds for the definition of  $\chi_t$ . Experimentally, all such angles, including the angles corresponding to  $\chi_t$  and  $\chi_W$  for the  $\bar{t}$  hemisphere, are accessible. Given the large number of constraints available in these events, full event reconstruction is entirely feasible. To reconstruct  $\theta$  one must also take into account photon and gluon radiation. Photon radiation from the initial state is an important effect, which, however, represents a purely longitudinal boost which can be handled within the framework of final-state mass constraints. Gluon radiation can be more subtle. Jets remaining after reconstruction of  $t$  and  $\bar{t}$  can be due to gluon radiation from  $t$  or  $b$ , and the correct assignment must be decided based on the kinematic constraints and the expectations of QCD.

The distributions of the production angle  $\theta$  for the SM in terms of the various helicity

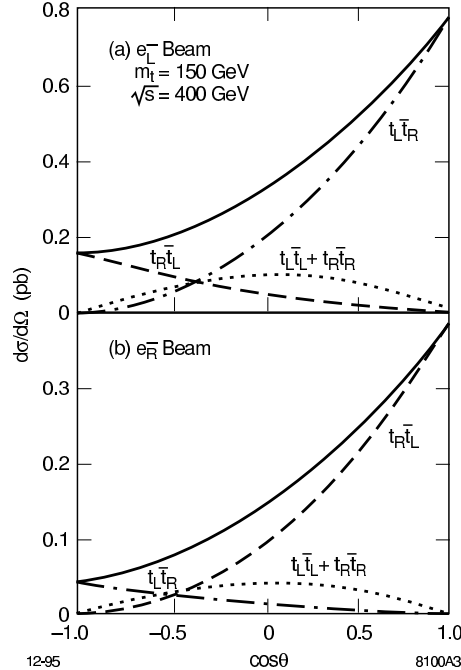


Figure 2.10: Production angle for  $t\bar{t}$  for the possible final-state helicity combinations, as indicated, for 100% polarized beams with (a) left-hand polarized electrons, and (b) right-hand polarized electrons. The complete cross sections are the solid curves.

states are given in Fig. 2.10 for left and right-hand polarized electron beam. We see, for example, that for a left-hand polarized electron beam, top quarks produced at forward angles are predominantly left handed, while forward-produced top quarks are predominantly right handed when the electron beam is right-hand polarized. These helicity amplitudes combine to produce the following general form for the angular distribution [19]:

$$\frac{d\sigma}{d\cos\theta} = \frac{\beta_t}{32\pi s} \left[ c_0 \sin^2\theta + c_+(1 + \cos\theta)^2 + c_-(1 - \cos\theta)^2 \right], \quad (2.8)$$

where  $c_0$  and  $c_{\pm}$  are functions of the form factors of Eq. 2.7, including any non-standard couplings. The helicity structure of the event is highly constrained by the measurements of beam polarization and production angle.

For the measurement of the decay form factors, there are two alternative methods that might provide higher statistics. The first is to measure the top quark decay distributions using polarized beams at the  $t\bar{t}$  threshold, making use of the fact that the spin of the nonrelativistic top quarks follows the spin of the incident electron and positron [20]. The second is to analyze the polarization of top quarks above threshold using the beam axis boosted to the top frame; this gives a very high polarization for the decay analysis [21].

For the top charged-current coupling we can write the  $Wtb$  vertex factor as

$$\mathcal{M}^{\mu,W} = \frac{g}{\sqrt{2}}\gamma^\mu [P_L F_{1L}^W + P_R F_{1R}^W] + \frac{ig}{2\sqrt{2}m_t}\sigma^{\mu\nu}k_\nu [P_L F_{2L}^W + P_R F_{2R}^W], \quad (2.9)$$

where the quantities  $P_{L,R}$  are the left-right projectors. In the Standard Model, we have  $F_{1L}^W = 1$  and all others zero. The form factor  $F_{1R}^W$  represents a right-handed, or  $V + A$ , charged current component. As mentioned earlier, the case where the  $W$  is longitudinally polarized is particularly relevant for heavy top, and the  $\chi_t$  and  $\chi_W$  distributions are sensitive to this behavior.

We now outline an analysis [22] to measure or set limits on the various form factors mentioned above. We consider a modest integrated luminosity of  $10 \text{ fb}^{-1}$ ,  $m_t = 180 \text{ GeV}/c^2$ , and  $\sqrt{s} = 500 \text{ GeV}$ . Electron beam polarization is assumed to be  $\pm 80\%$ . The decays are assumed to be  $t \rightarrow bW$ . In general, one needs to distinguish  $t$  from  $\bar{t}$ . The most straightforward method for this is to demand that at least one of the  $W$  decays be leptonic, and to use the charge of the lepton as the tag. (One might imagine using other techniques, for example with topological secondary vertex detection one could perhaps distinguish  $b$  from  $\bar{b}$ .) So we assume the following decay chain:

$$t\bar{t} \rightarrow b\bar{b}WW \rightarrow b\bar{b}q\bar{q}\ell\nu, \quad (2.10)$$

where  $\ell = e, \mu$ . The branching fraction for this decay chain is 29%.

Since the top production and decay information is correlated, it is possible to combine all relevant observables to ensure maximum sensitivity to the couplings. In this study, a likelihood function is used to combine the observables. We use the Monte Carlo generator developed by Schmidt [23], which includes  $t\bar{t}(g)$  production to  $\mathcal{O}(\alpha_s)$ . Most significantly, the Monte Carlo correctly includes the helicity information at all stages. The top decay products, including any jets due to hard gluon radiation, must be correctly assigned with good probability. The correct assignments are rather easily arbitrated using the  $W$  and top mass constraints. When the effects of initial-state radiation and beamstrahlung are included, it has been shown [19] that the correct event reconstruction can be performed with an efficiency of about 70%. The overall efficiency of the analysis, including branching fractions, reconstruction efficiency, and acceptance, is about 18%.

After simple, phenomenological detection resolution and acceptance functions are applied, the resulting helicity angles (see Fig. 2.9) are then used to form a likelihood which is the square of the theoretical amplitude for these angles given an assumed set of form factors. Table 2.3 summarizes some of the results of this analysis. The upper and lower limits of the top quark couplings in their departures from the Standard Model values are given at 68% and 90% CL. All couplings, with real and imaginary parts, can be determined in this way. The right-handed charged-current coupling is shown both for unpolarized and 80% left-polarized electron beam, whereas the other results assume 80% left-polarized beam only. We see that even with a modest integrated luminosity of  $10 \text{ fb}^{-1}$  at  $\sqrt{s} = 500 \text{ GeV}$ , the sensitivity to the form factors is quite good, at the level of 5–10% relative to Standard Model couplings. In

terms of absolute units, the 90% CL limit of  $F_{2A}^Z$  at 0.15, for example, corresponds to a  $t$ - $Z$  electric dipole moment of  $8 \times 10^{-18}$  e-cm.

Table 2.3: Results from the global top quark form factor analysis described in the text, for a data sample of  $10 \text{ fb}^{-1}$  and  $\sqrt{s} = 500 \text{ GeV}$ .

Form Factor	SM Value (Lowest Order)	Limit 68% CL	Limit 90% CL
$F_{1R}^W(P = 0)$	0	$\pm 0.13$	$\pm 0.18$
$F_{1R}^W(P = 80\%)$	0	$\pm 0.06$	$\pm 0.10$
$F_{1A}^Z$	1	$1 \pm 0.08$	$1 \pm 0.13$
$F_{1V}^Z$	1	$1 \pm 0.10$	$1 \pm 0.16$
$F_{2A}^\gamma$	0	$\pm 0.05$	$\pm 0.08$
$F_{2V}^\gamma$	0	$\pm 0.07$	$^{+0.13}_{-0.11}$
$F_{2A}^Z$	0	$\pm 0.09$	$\pm 0.15$
$F_{2V}^Z$	0	$\pm 0.07$	$\pm 0.10$
$\Im(F_{2A}^Z)$	0	$\pm 0.06$	$\pm 0.09$

### 2.3.4 The Higgs-Top Yukawa Coupling

The coupling strength of the Higgs boson to a fermion is proportional to the fermion's mass. The Higgs-top coupling is consequently large and may be unique among the Higgs-fermion couplings in that it is accessible to direct measurement. Such measurements have been contemplated at LHC [24], but they require efficient vertex tagging in high-luminosity running. The environment at NLC is much cleaner, but the luminosity requirements are comparable. With the availability of large data sets ( $> 50 \text{ fb}^{-1}$ ), several approaches are tractable at NLC: (1) for light to moderate mass Higgs bosons, the  $t\bar{t}$  production cross-section near threshold is sensitive to the Higgs contribution to the  $t\bar{t}$  potential; (2) for relatively light Higgs, the yield of  $t\bar{t}H$  events measures the Higgs-top coupling; and (3) for Higgs masses exceeding the  $t\bar{t}$  threshold, the Higgs boson resonance can appear in  $t\bar{t}Z$  events and exhibit the Higgs-top coupling.

Threshold measurements have been discussed above for their intrinsic interest and sensitivity to basic top parameters. Here we note that the presence of an additional attractive, short range force arising from Higgs exchange increases the modulus of the toponium wavefunction at the origin, and thereby enhances the cross-section. Fig. 2.11 shows the distinctive energy dependence of the Higgs enhancement factor, which peaks at the 1S state [25]. Fujii *et al.*[12] have simulated a threshold scan of 10 points, spaced at 1 GeV intervals, to de-

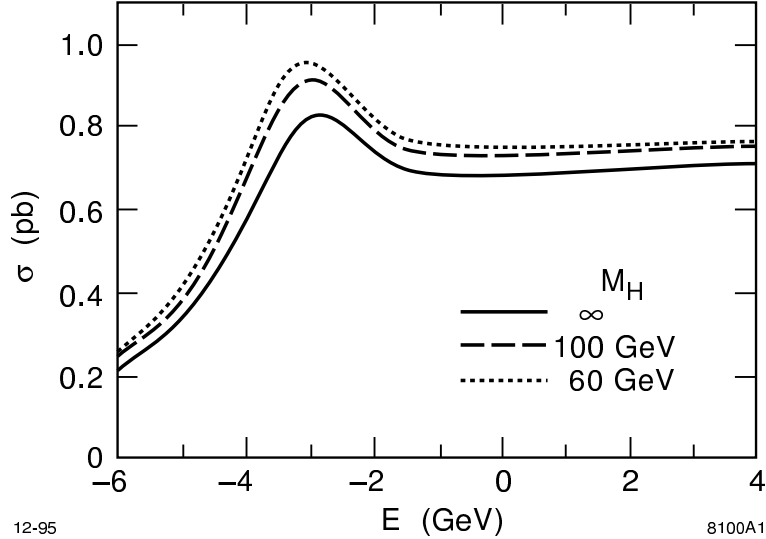


Figure 2.11: Theoretical cross section as a function of Higgs mass for  $m_t = 180 \text{ GeV}/c^2$ .

termine the sensitivity to the Higgs-top coupling strength. Their results imply that a 10% measurement is possible with  $100 \text{ fb}^{-1}$  evenly distributed over the 10 points for  $M_H = 100 \text{ GeV}$ . The enhancement is roughly inversely proportional to the Higgs mass, so the scan would yield a 20% (30%) measurement for a 200 (300) GeV Higgs mass. An optimized scan will do better.

The  $t\bar{t}H$  events almost always result from “Higgs-strahlung”, radiation of the Higgs boson from one of the top quarks, so their yield provides a measure of the square of the Higgs-top coupling. The cross-section for the process is small [26], in the  $\mathcal{O}(1) \text{ fb}$  range for a 500 GeV NLC and  $M_H < 100 \text{ GeV}$ . Detection of the events is challenging; they typically contain 8 jets, including 4  $b$  jets. The process  $e^+e^- \rightarrow t\bar{t}Z$  occurs at comparable rate, and along with  $e^+e^- \rightarrow t\bar{t}jj$  constitutes the important background. Preliminary studies [12, 27] show that a  $100 \text{ fb}^{-1}$  sample at 500 GeV will give a  $\leq 15\%$  measurement of the Higgs-top coupling for  $M_H \leq 100 \text{ GeV}$ . At  $\sqrt{s} = 1000 \text{ GeV}$ , the sensitivity extends to over 200 GeV for a measurement of similar accuracy.

The cross-section for  $e^+e^- \rightarrow t\bar{t}Z$  is about 5 fb between 500 and 1000 GeV center-of-mass energies. When the Higgs mass is above the  $t\bar{t}$  threshold, this cross section is enhanced by the process  $e^+e^- \rightarrow Z^0H^0$ , with Higgs decay to  $t\bar{t}$ . Fujii *et al.* [28] have studied the process for  $m_t = 130 \text{ GeV}$ , and concluded that, with an integrated luminosity of  $60 \text{ fb}^{-1}$  at  $\sqrt{s} = 600 \text{ GeV}$ , one could measure the top-Higgs coupling within 10% for a 300 GeV Higgs. For Higgs masses above  $2m_t$ , the cross-section is lower, and the increased width of the Higgs will make isolating a signal in the  $t\bar{t}$  invariant mass distribution more difficult. Even so, one could measure the Higgs-top coupling for a 400 GeV Higgs produced at  $\sqrt{s} = 1000 \text{ GeV}$  within about 35% with a data sample of  $100 \text{ fb}^{-1}$ .

The Higgs-strahlung process is also sensitive to deviations from the Standard Model

involving extended Higgs sectors. The  $t\bar{t}H$  final state can result from Higgs emission from the  $t$  (or  $\bar{t}$ ), or from the intermediate  $Z$ . Interference between these sub-processes can give rise to large CP violating effects in extended Higgs models. This was studied in Ref. [29] for a range of two-Higgs doublet models, and it was found that for roughly  $100 \text{ fb}^{-1}$  of data at  $\sqrt{s} = 800 \text{ GeV}$  it would be possible to observe a significant CP asymmetry in a number of final-state observables.

The Higgs-top coupling can be determined in the case that the Higgs is very heavy ( $M_H > 400 \text{ GeV}/c^2$ ) by measuring the rate of the process  $e^+e^- \rightarrow \nu\bar{\nu}t\bar{t}$ . At  $\sqrt{s} = 1500 \text{ GeV}$ , the cross section for this process is about  $2 \text{ fb}$  in the absence of a Higgs, but will be enhanced by more than a factor of two for Higgs masses in the range  $400\text{--}1000 \text{ GeV}/c^2$ . Preliminary studies by Fujii [28] show that care is required to eliminate radiative  $t\bar{t}$ ,  $e^+e^-t\bar{t}$ , and  $t\bar{t}Z$  backgrounds, but suggest that the Higgs-top coupling can be measurable up to  $m_H = 1 \text{ TeV}/c^2$ . The case of a very heavy Higgs boson is discussed in more detail in Section 7.3.

### 2.3.5 Top Physics Reach of NLC and Hadron Colliders

Table 2.4 summarizes the top physics reach of the NLC and several hadron colliders. The Tevatron Upgrade (TeV\*) will establish the baseline for top quark physics in the LHC/NLC era, and will address many subjects of interest in top physics. Its reach has been studied in a report by Amidei *et al.* [30]. The Atlas TDR [24] provides some information on the top physics reach at LHC; this subject will certainly be developed further in the future. The table at best represents what has been studied to date. If a particular measurement at a particular machine has not yet been analyzed, the corresponding entry has been left blank. An “X” marks measurements that cannot be made at a particular machine, by virtue of excessive backgrounds, insufficient signal, or unavailable production mechanisms.

The table demonstrates how crucial a role the NLC plays in obtaining a complete picture of top quark physics. NLC will provide the definitive top mass measurement. It will provide the only direct measure of the top width; at hadron colliders, the total width can be inferred only from a  $V_{tb}$  measurement using the assumption that the top has no unobserved exotic decays. The NLC will measure the axial-vector and vector electroweak couplings, some of the charged-current couplings (expressed here as CKM elements), the top-Higgs coupling, and the flavor specific strong coupling. Hadron colliders will also measure the charged current couplings (although  $V_{td}$  is probably impossible at both hadron and  $e^+e^-$  colliders), and the strong and electromagnetic couplings, but not the couplings to the  $Z$ . The LHC may probe the top-Higgs coupling by isolating  $t\bar{t}H$  events, but only with difficulty. The NLC can measure the top decay form factors, checking for longitudinal  $W$  production and searching for right-handed  $W$ 's, as can the hadron colliders. Only the NLC can measure the electroweak magnetic and electric dipole moments, because they depend on the neutral current production mechanism. We should note that LHC can be sensitive to top-associated CP violation through more complicated effective interactions [31, 32]. Rare decays with distinctive signatures can be sought in either environment, with the advantage to hadron

Table 2.4: Top Physics at Future Facilities

Quantity	TeV* (1 fb <sup>-1</sup> )	TeV33 (10 fb <sup>-1</sup> )	LHC (100 fb <sup>-1</sup> )	NLC( $\sqrt{s} = 360$ ) (50 fb <sup>-1</sup> )	NLC( $\sqrt{s} = 500$ ) (50 fb <sup>-1</sup> )
$\Delta m_t$	3.5 GeV/c <sup>2</sup>	2.0 GeV/c <sup>2</sup>	2 GeV/c <sup>2</sup>	0.20 GeV/c <sup>2</sup>	
$\Delta \Gamma_t$				6–8%	
$\Delta a_t$	X	X	X		4%
$\Delta v_t$	X	X	X		5%
$\Delta V_{tb}$	14%	6%	X		
$\Delta V_{ts}$	X	X	X?	?	?
$\Delta V_{td}$	X	X	X	X	X
$\Delta \lambda_t$	X	X	?	14%	20%
$\Delta \alpha_s^t$	( $\sigma_{t\bar{t}} = 11\%$ )	( $\sigma_{t\bar{t}} = 4\%$ )		0.005	
$\Delta B(t \rightarrow bW^0)$	4%	1.3%		1%	
$\Delta B(t \rightarrow bW_R)$	2%	0.6%			2%
$\Delta \delta$	X	X	X		$< 0.3 e\hbar/2m_t$
$\Delta d$	X	X	X		$< 4 \times 10^{-18}$ e-cm
$B(t \rightarrow H^+b)$	$< 15\%$	$< 6\%$	$< 1.4\%$		$< 2\%$
$B(t \rightarrow \tilde{t}\tilde{\chi}^0)$					$< 1\%$
$B(t \rightarrow c\gamma)$	$< 0.3\%$	$< 0.04\%$			
$B(t \rightarrow cZ)$	$< 1.5\%$	$< 0.4\%$	$< 5 \times 10^{-5}$		$< \text{few} \cdot 10^{-4}$
$B(t \rightarrow ch^0)$				$< 1\%$	

decays by virtue of the large statistical samples anticipated. The more exotic decays, *e.g.*  $t \rightarrow \tilde{t}\tilde{\chi}^0$ , are more sensitively sought in the clean environment of the NLC.

## 2.4 Higgs Boson Searches and Properties

### 2.4.1 Introduction

Despite the extraordinary success of the Standard Model (SM) in describing particle physics up to the highest energy available today, the mechanism responsible for electroweak symmetry breaking (EWSB) has yet to be determined. In particular, the Higgs boson [33, 34, 35] predicted in the minimal Standard Model and the theoretically attractive Supersymmetric (SUSY) Grand Unified Theory (GUT) extensions thereof have yet to be observed. If EWSB does indeed derive from nonzero vacuum expectation values for elementary scalar Higgs fields, then one of the primary goals of constructing future colliders must be to *completely* delineate the Higgs boson sector. In particular, it will be crucial to discover all of the physical Higgs bosons and determine their masses, widths and couplings. Conversely, if a fundamental Higgs boson does not exist, it is essential to demonstrate this unambiguously.

The EWSB mechanism in the Standard Model is phenomenologically characterized by a single Higgs boson ( $h_{SM}$ ) in the physical particle spectrum. The mass of the  $h_{SM}$  is undetermined by the theory, but its couplings to fermions and vector bosons are completely determined. In SUSY theories, there are two Higgs doublets with vacuum expectation values  $v_1, v_2$ . These contribute mass terms for the gauge bosons proportional to  $(v_1^2 + v_2^2)$ , masses for down-type fermions proportional to  $v_1$ , and masses for up-type fermions proportional to  $v_2$ . In the Minimal Supersymmetric Standard Model (MSSM) [36, 37] these two doublets give rise to five physical Higgs bosons:  $h^0$ , the lighter of the two  $CP$ -even states;  $H^0$ , the heavier  $CP$ -even state; the  $CP$ -odd  $A^0$  boson, and a pair of charged bosons  $H^\pm$ . The mass of the minimal SM Higgs boson is unspecified, but in the MSSM, there are tree-level relations which determine the spectrum of masses in terms of one of the boson masses (e.g., the mass of the  $A^0$ ) and the ratio of the vacuum expectation values,  $v_2/v_1$ . The  $CP$ -even and  $CP$ -odd neutral Higgs bosons have nontrivial mixing angles  $\alpha$  and  $\beta$ , respectively, which affect their couplings and decays. In particular,  $v_2/v_1 = \tan \beta$ . Both masses and couplings receive further radiative corrections which are functions of the SUSY Higgs mass parameter,  $\mu$ , the scale of mass at which SUSY is broken,  $M_{SUSY}$ , the mass of the top quark, and the  $A_i$  parameters of the soft supersymmetry-breaking interaction. More general models of the Higgs sector, which also include electroweak singlets, are also possible in SUSY theories. Finally in non-supersymmetric models with two Higgs doublets (2HDM), the Higgs bosons may have mixed  $CP$  character.

Supersymmetry has exciting implications for the discovery potential of the Higgs bosons that it predicts. In the MSSM, considering renormalization group improved radiative corrections and assuming  $m_t = 180$  GeV with the stop mass less than 1 TeV, the lightest Higgs boson must have mass  $M_{h^0} \lesssim 130$  GeV. An even more sweeping statement can be made [38] that  $M_{h^0} \lesssim 150$  GeV for *any* SUSY theory with a grand unification at high energy which includes the elementary Higgs fields.

## 2.4.2 Present and Future Limits

The best direct limits on the SM Higgs boson come from searches at LEP, with the present limit [39] being  $M_{h_{SM}} > 65.2$  GeV at 95% confidence level (C.L.). These limits can also be interpreted in the framework of the MSSM to exclude the lightest SUSY Higgs with mass less than approximately 45 GeV. Electroweak radiative corrections including the top quark and the Higgs boson affect precision electroweak measurements, and global fits [40] using data from LEP, SLC, the Tevatron, and neutrino scattering give the relatively weak limit implying that  $M_{h_{SM}} < 300$  GeV (95% C.L.).

### LEP2

The limit on the Higgs boson mass will be improved in the near future with the operation of LEP2. With an integrated luminosity of  $150 \text{ pb}^{-1}$  in each of the four LEP detectors, expected from one year of running at design luminosity, the  $5\sigma$  discovery reach can be increased [41] to about 95 GeV with running at center-of-mass energies of 192 GeV scheduled for 1997. At the same energy and luminosity, the process  $e^+e^- \rightarrow hA$  can be discovered (excluded) at a cross section of 65 (30) fb, when supersymmetric decay channels are closed. The resultant exclusion region in the MSSM parameter space can be found in Fig. 2.13. The possibility of running at 205 GeV, which would result in an extension of limits close to the MSSM bound, is currently being investigated.

### Upgraded Tevatron

The associated production of a Higgs boson and a  $W$  or  $Z$  boson, with the Higgs decaying to  $b\bar{b}$  and the  $W$  or  $Z$  decaying leptonically, is a possible way to detect the Higgs in the mass range 60–130 GeV, at a high luminosity Tevatron collider [30]. The Higgs decay gives rise to 2 jets, thus one will use  $b$  tagging to reduce the large  $W + 2$  jet background. It appears that the present  $b$  tagging capability at CDF is more than adequate to reduce this background (at moderate Run II luminosities, e.g.,  $10^{32} \times \text{cm}^{-2} \text{ sec}^{-1}$ ,  $1 \text{ TeV} \times 1 \text{ TeV}$ ) if this capability is extended to larger rapidities (as is planned in Run II for both CDF and D0). After  $b$  tagging, the largest background at Higgs masses below 100 GeV is QCD production of  $W + b\bar{b}$  and top backgrounds for masses above 100 GeV. Figure 2.12 shows the dijet mass distribution for the sum of all these backgrounds, plus the  $W + H$  signal for  $10 \text{ fb}^{-1}$ . An observation of the Higgs for masses below 100 GeV is possible after the Main Injector upgrade, and is within reach of the present Run II accelerator after several years of data-taking. For higher mass Higgs bosons, these statistics are too low; one would need about  $25 \text{ fb}^{-1}$  to observe the 120 GeV Higgs. This study assumed an approximate 20% improvement in dijet mass resolution obtained from applying a clustering algorithm that reduces the effect of gluon radiation at large angles to the jet. This dijet mass resolution and jet clustering is crucial in seeing the Higgs. It has been argued that the  $h \rightarrow \tau^+\tau^-$  and  $Z \rightarrow \nu\bar{\nu}$  channels can be used to improve these results [43].

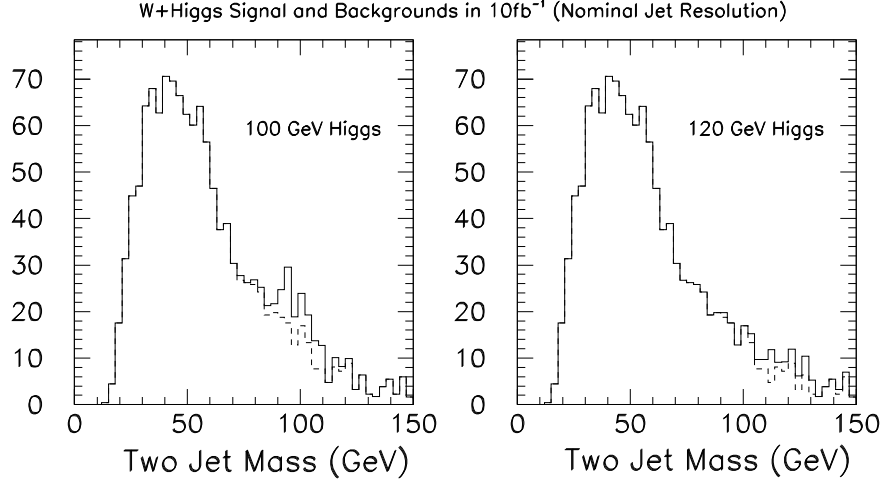


Figure 2.12: The signal plus background mass distributions for the  $WH$  process with  $10 \text{ fb}^{-1}$  of data at 2 TeV. The solid line is signal+background, the dashed line the sum of all backgrounds.

## Large Hadron Collider

At the Large Hadron Collider (LHC), detection of the SM  $h_{SM}$  is possible through the process  $gg \rightarrow h_{SM} \rightarrow \gamma\gamma$  for  $M_{h_{SM}} < 150 \text{ GeV}$  and through  $gg \rightarrow h_{SM} \rightarrow ZZ^{(*)} \rightarrow 4\ell$  for  $M_{h_{SM}} > 130 \text{ GeV}$ . A heavy  $h_{SM}$  is also detectable in the reaction  $WW \rightarrow h_{SM}$ , with the Higgs decaying to  $ZZ$  and also, possibly, to  $WW$ . The  $\gamma\gamma$  channel that is crucial for a light  $h_{SM}$  demands an excellent electromagnetic calorimeter, and much attention has been devoted to this in the LHC detector designs. For  $M_{h_{SM}} < 120 \text{ GeV}$ , it will also be possible to detect  $t\bar{t}h_{SM}$  and (possibly)  $Wh_{SM}$  with  $h_{SM} \rightarrow b\bar{b}$ , provided that the high  $b$ -tagging efficiency and purity projections are realized. Detection of the  $h_{SM}$  in the intermediate mass region when  $M_{h_{SM}} < 2M_W$  generally requires accumulating data for at least a year when the LHC is run at full luminosity. This should be contrasted with  $e^+e^-$  collisions, where the  $e^+e^- \rightarrow Zh_{SM}$  mode will allow detection in the same mass region in a matter of a few hours, assuming full instantaneous luminosity.

In the case of the MSSM for large  $M_{A^0}$ , the  $h^0$  is similar to the Standard Model Higgs  $h_{SM}$ . As for the  $h_{SM}$ , the  $h^0$  is straightforward to detect at an  $e^+e^-$  collider. On the other hand, the  $H^0$  and  $A^0$  do not resemble the Standard Model Higgs boson, and so one must separately consider their production process. We will show below that the observability of  $H^0$  and  $A^0$  at an  $e^+e^-$  collider depends only on the beam energy: for  $\sqrt{s} > 2M_{A^0} - 20 \text{ GeV}$ , these particles are found in the reaction  $e^+e^- \rightarrow Z^* \rightarrow H^0 A^0$ .

The story at the LHC is much more complex. The reactions which can be used to detect the Higgs particles of the MSSM, and their limits of applicability in parameter space, are displayed in Fig. 2.13 [35]. This figure represents the limit of the LHC capability, summing the results of two detectors in a multi-year run at design luminosity. For values of  $M_A > 200 \text{ GeV}$ , the LHC can detect the  $H^0$  and  $A^0$  only in certain specific decay channels, shown in

the figure, whose availability depends on the value of  $\tan\beta$ . Since this figure summarizes a great deal of analysis, we must point out at least a few of the assumptions which are used. The channel  $A^0, H^0 \rightarrow \tau^+\tau^-$  can be used only when the branching ratio to  $\tau$  is enhanced by a large value of  $\tan\beta$ . For small  $\tan\beta$ , modes with  $b\bar{b}$  or  $t\bar{t}$  in the final states require  $b$  tagging capabilities that will be challenging in the detection environment of the LHC. In addition, it should be noted that the process  $A^0, H^0 \rightarrow t\bar{t}$  has so far been studied only at the level of the comparison of cross sections for signal and background, and that, since the signal is 2–10% of the background, an excellent knowledge of the  $gg \rightarrow t\bar{t}$  cross section is required. Finally, though the  $h^0$  should be detected for the generic situation illustrated in Fig. 2.13, there are regions of the full parameter space of the MSSM where the  $h^0$  would not be observed [42]. Thus, it is unlikely that the whole MSSM Higgs spectrum would be observed at the LHC, and it is not possible to rule out the MSSM if none of its Higgs bosons are seen at the LHC.

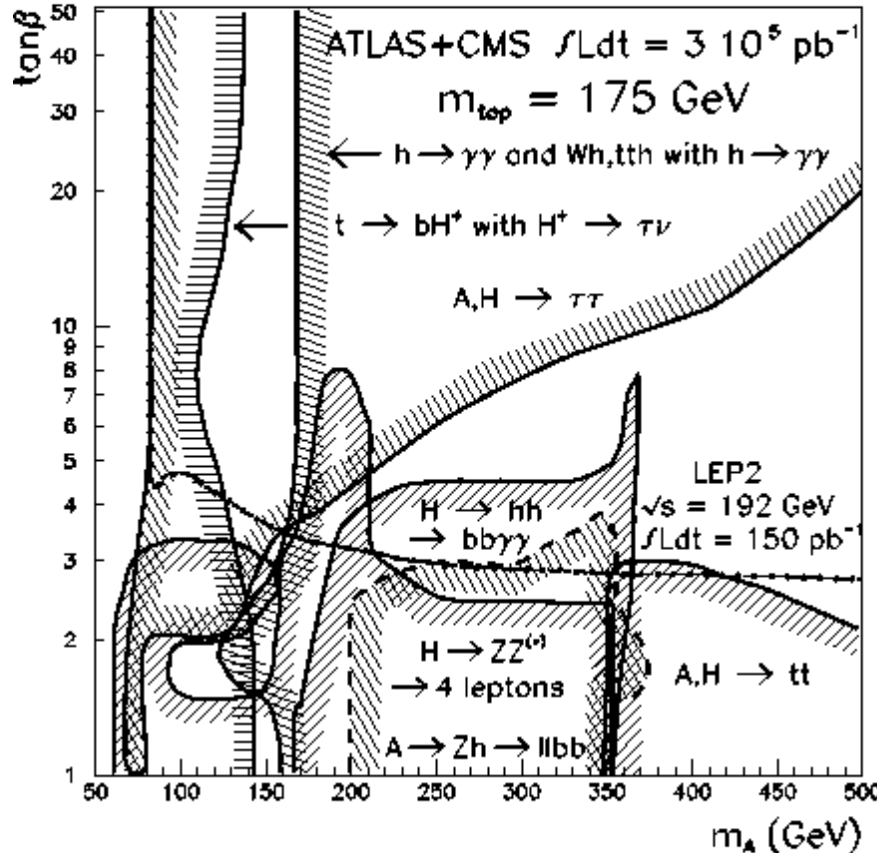


Figure 2.13: Higgs discovery contours ( $5\sigma$ ) in the generic parameter space of the MSSM for ATLAS+CMS at the LHC, for a multi-year run at design luminosity,  $300 \text{ fb}^{-1}$  per detector, from [35]. Renormalization group improved radiative corrections are included for  $M_{h^0}$  and  $M_{H^0}$ , assuming  $m_{\tilde{t}} = 1 \text{ TeV}$  and no squark mixing.

### 2.4.3 Standard Model Higgs

The main production processes for the SM Higgs in  $e^+e^-$  annihilation are  $e^+e^- \rightarrow ZH$  and the gauge boson fusion processes  $e^+e^- \rightarrow \nu\bar{\nu}H$  ( $WW$  fusion) and  $e^+e^- \rightarrow e^+e^-H$  ( $ZZ$  fusion). The cross sections for these processes are shown in Fig. 2.14. With a typical integrated luminosity of  $10 \text{ fb}^{-1}$  at  $\sqrt{s} = 500 \text{ GeV}$  with  $M_H = 150 \text{ GeV}$ , about 1000 signal events would be expected before cuts and branching ratios. Handy “rules of thumb” are that the peak for  $ZH$  production occurs at  $\sqrt{s} \approx M_Z + \sqrt{2}M_H$  and that the cross-over for equal cross sections from the fusion and bremsstrahlung mechanisms occurs at  $\sqrt{s} \approx 0.6M_H + 400 \text{ GeV}$ .

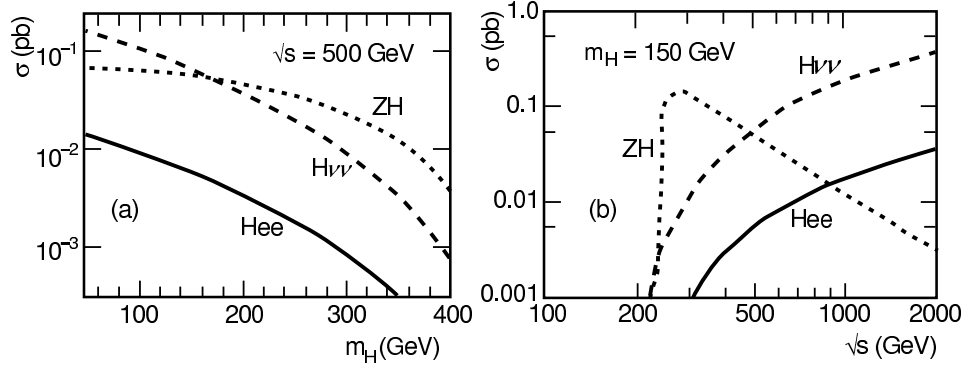


Figure 2.14: Cross section for Standard Model Higgs boson production.

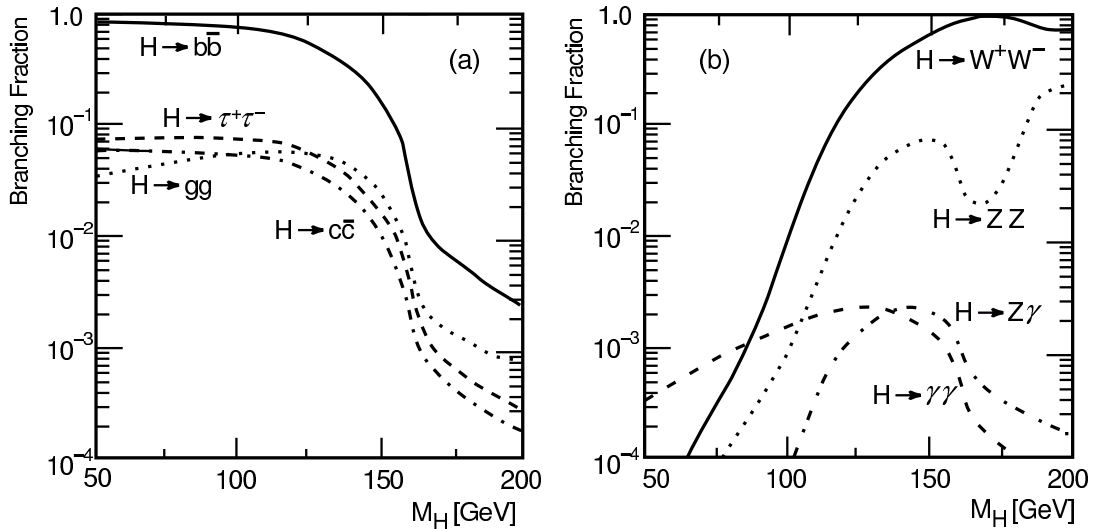


Figure 2.15: Branching fractions of a SM Higgs boson.

The decay modes of the Standard Model Higgs depend strongly upon its mass. The branching ratios of the Standard Model Higgs are shown in Fig. 2.15. A very interesting

region is the intermediate mass Higgs with  $M_Z < M_H < 2M_W$ , which at a hadron collider is relatively more difficult to detect than a heavy Higgs boson. Almost all of the decays, both those to fermions and those into pairs of gauge bosons are identifiable in  $e^+e^-$  experiments, and it should be possible to measure individual branching ratios. For an intermediate mass Higgs, the dominant decay channel is clearly  $H^0 \rightarrow b\bar{b}$ , with the branching ratio for  $H^0 \rightarrow W^+W^-^{(*)}$  growing with increasing mass (even for  $E_{cm} < 2M_W$  where one of the  $W$ 's must be off shell). This latter channel remains dominant for heavy Higgs bosons, and is joined by  $ZZ$  and  $t\bar{t}$  modes when kinematically accessible.

## Signal Topologies and Backgrounds

Typical signal topologies in the intermediate mass range are shown in Fig. 2.16. The associated production  $e^+e^- \rightarrow Z^0 H^0$ , is followed by standard decays of the  $Z^0$  (10%  $\ell^+\ell^-$ , 20%  $\nu\bar{\nu}$ , and 70%  $q\bar{q}$ ) and decays of the  $H^0$  mostly into  $b\bar{b}$ , occasionally into  $\tau^+\tau^-$ , and more rarely into  $c\bar{c}$  and  $gg$ . After straightforward cuts, the most serious backgrounds are due to irreducible Standard Model processes,  $e^+e^- \rightarrow ZZ$ ,  $Z\nu\bar{\nu}$ , and  $W e\nu$ .

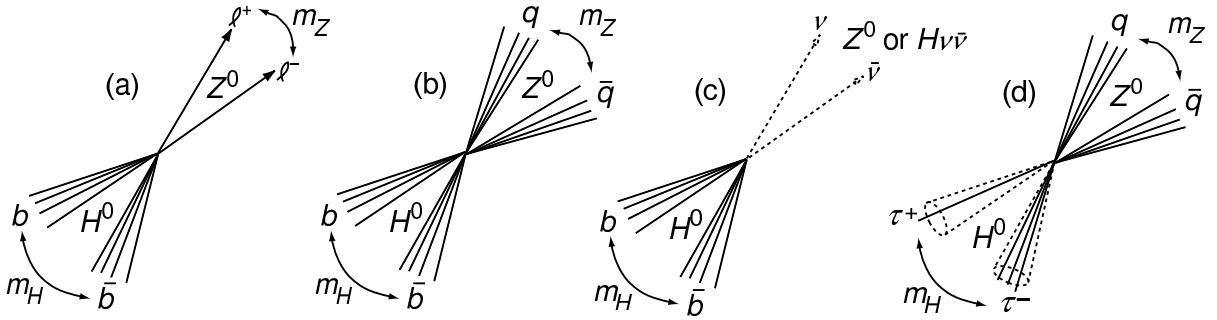


Figure 2.16: Important signal topologies for an intermediate mass SM Higgs boson.

## Experimental Studies

The detection of Higgs bosons in  $e^+e^-$  collisions at high energy has been studied extensively in simulations [48, 45, 46]. The detector simulations that have been employed usually emulate LEP/SLC-type detectors using smeared four-vectors, while some consider simulations of a more ambitious JLC-type detector [47]. Most studies include the effects of beamstrahlung, the radiation of photons in the intense electromagnetic fields of the beam-beam collision. Like more standard initial-state radiation, this effect is usually taken into account in kinematic fits by allowing for an unknown missing momentum along the beam axis.

In the topology of Fig. 2.16a, one can first identify two leptons with invariant mass close to the mass of the  $Z^0$ , and then investigate the remaining hadronic mass or use kinematic

constraints to study the missing or recoil mass in the event:

$$M_{miss} = \sqrt{(\sqrt{s} - E_{\ell^+} - E_{\ell^-})^2 - (\vec{p}_{\ell^+} + \vec{p}_{\ell^-})^2}.$$

This quantity has a large peak at the  $Z^0$  mass from the irreducible background process  $e^+e^- \rightarrow Z^0Z^0$ ;  $Z^0 \rightarrow \ell^+\ell^-$ ;  $Z^0 \rightarrow q\bar{q}$ . If  $M_H \approx M_Z$ , the signal and the  $ZZ$  background are kinematically equivalent, and one would need  $b$ -quark tagging to distinguish the signal. Since  $Br(Z^0 \rightarrow b\bar{b}) \simeq 20\%$ , while  $Br(H^0 \rightarrow b\bar{b}) \simeq 85\%$  at this mass, an analysis in this worst case would require  $50 \text{ fb}^{-1}$  of data.

The four-jet topology of Fig. 2.16b has been considered in a number of studies, in particular, in a comprehensive study by Janot [48] at  $\sqrt{s} = 500 \text{ GeV}$  which assumed an integrated luminosity of  $10 \text{ fb}^{-1}$ . After selection cuts, for  $M_H = 110 \text{ GeV}$ , a small signal is observed above the background, which comes mainly from  $e^+e^- \rightarrow W^+W^-$ ,  $Z^0Z^0$ , and  $qq(\gamma)$ . This signal is greatly enhanced, as shown in Fig. 2.17b, by requiring that at least one of the jets forming the Higgs signal peak come from a tagged  $b$  quark. The vertex-tagger is assumed to have the conservative performance  $\epsilon_{b\bar{b}} = 50\%$ ,  $\epsilon_{c\bar{c}} = 2.5\%$ ,  $\epsilon_{c\bar{s}} = 0.3\%$ , and  $\epsilon_{q\bar{q}} = 0.1\%$ , where the numbers give the efficiency for tagging a particular quark combination. The importance of  $b$  tagging is even greater as one moves up in mass.

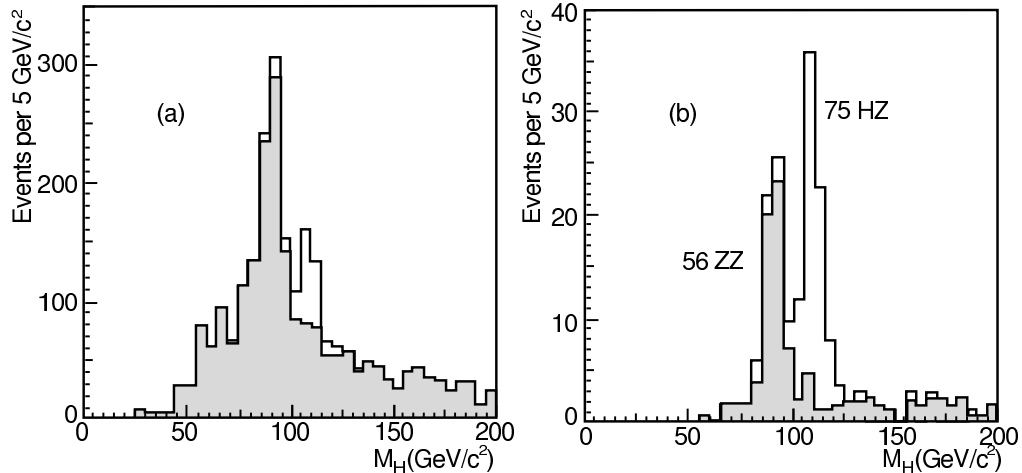


Figure 2.17: Distribution of the invariant mass of the Higgs jet pair in the four-jet topology (a) before and (b) after  $b$ -quark tagging, for all known backgrounds (shaded histograms) and for the signal ( $M_H = 110 \text{ GeV}$ ) (adapted from Ref. 10).

The missing energy topology shown in Fig. 2.16c can arise either from the  $ZH$  process, with  $(Z^0 \rightarrow \nu\bar{\nu})(H^0 \rightarrow b\bar{b})$ , or from  $WW$  fusion. The resultant events will have large missing energy, transverse momentum, and mass, plus the presence of acoplanar jets. This distinctive signature offsets the loss of the  $Z$ -mass constraint. The last topology of Fig. 2.16d can be isolated by tagging two  $\tau$  leptons either from their one- or three-prong decays recoiling

against a reconstructed  $Z^0$  decaying into  $q\bar{q}$ . Using a kinematically-constrained fit the missing neutrinos from the  $\tau$  decay can be taken into account.

The examples given so far rely primarily on the large branching ratio for  $H^0 \rightarrow b\bar{b}$ . As the  $H^0$  gets heavier, other decay modes begin to become important. For example, for  $M_H = 140$  GeV,  $Br(H^0 \rightarrow W^*W) \simeq 45\%$ . The mode  $(Z^0 \rightarrow q\bar{q})(H^0 \rightarrow W^*W)$  has been investigated [49] by demanding a six-jet event with a reconstructed  $Z^0$  hadronic decay, one jet pair reconstructing to  $M_W$ , and the last pair peaking at  $m < M_W$ , depending on  $M_H$ . Similarly, for  $M_H = 160$  GeV, the decay  $H^0 \rightarrow W^+W^-$  dominates, and for production via fusion,  $e^+e^- \rightarrow H\nu\bar{\nu}$ , the result is an acoplanar pair of reconstructed  $W$  bosons and a total visible mass peaking at the  $H$  mass which is expected to be well above background without the need for  $b$ -tagging.

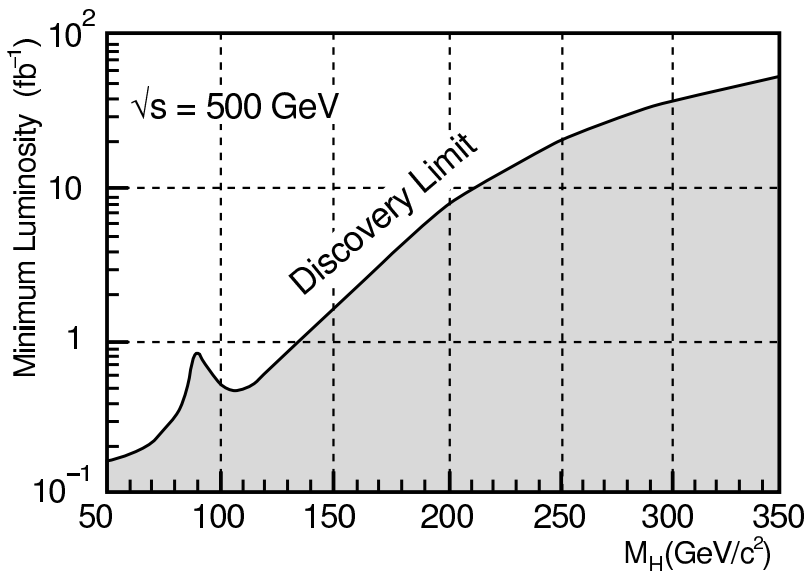


Figure 2.18: Minimum luminosity needed to discover a SM Higgs boson at a center-of-mass energy of 500 GeV.

Thus, studies have shown that with a detector similar to the LEP/SLC detectors, with  $b$ -quark vertex tagging provided by silicon microvertex detectors using present technology, an intermediate-mass SM Higgs boson cannot escape detection at an  $e^+e^-$  linear collider at  $\sqrt{s} = 500$  GeV. Figure 2.18 shows an estimate [48] of the minimum luminosity required to discover at the  $5\sigma$  level a SM Higgs boson of a particular mass. An integrated luminosity of only  $5 \text{ fb}^{-1}$  would be adequate to cover the entire intermediate mass range, while  $20 \text{ fb}^{-1}$  would allow a reach in mass up to about  $\sqrt{s}/2$ .

Higher  $\sqrt{s}$  would of course allow one to probe for the existence of much heavier Higgs bosons, mostly through  $WW$  fusion and decay into pairs of vector bosons. At center of mass energies of 1–2 TeV, different backgrounds such as  $e^+e^-W^+W^-$  and  $e^+\nu_e W^- Z^0$  need to be addressed. Even though there exist older studies [7, 50] of searches for heavy Higgs bosons in 1–2 TeV  $e^+e^-$  collisions, these investigations need to be updated with more detailed

simulations and to keep abreast of theoretical developments [51] regarding backgrounds and the decay of heavy Higgs bosons. For very large Higgs boson masses, this study becomes a part of the general problem of studying  $WW$  scattering at high energies; we discuss this problem in some detail in Section 7.2.

#### 2.4.4 Minimal Supersymmetric Standard Model Higgs

In the framework of the MSSM, production of the lightest  $CP$ -even state  $h^0$  is similar to that of the SM Higgs boson. It is produced by the  $Zh$  and  $WW$  fusion processes just described, with  $h^0$  replacing  $h_{SM}$ . In addition, new modes of production also open up, involving the heavy Higgs bosons  $H^0$  and  $A^0$ . The various production processes for  $h^0$  and  $H^0$  in  $e^+e^-$  annihilation depend on the mixing angles  $\alpha$  and  $\beta$  as indicated in Table 2.5. Notice the sum rule: One process in each line always has a substantial rate. As  $m_A \rightarrow \infty$  in the MSSM,  $\cos(\beta - \alpha) \rightarrow 0$ , and only the processes in the left-hand column of the table occur. In this limit, the rates of the  $h^0$  production processes are identical to those for the Standard Model Higgs.

Table 2.5: Dependence of the cross section on Higgs boson mixing angles for various Higgs boson production processes in the MSSM.

$\sin^2(\beta - \alpha)$	$\cos^2(\beta - \alpha)$
$h^0 Z^0$	$H^0 Z^0$
$h^0 \nu \bar{\nu}$	$H^0 \nu \bar{\nu}$
$H^0 A^0$	$h^0 A^0$

The phenomenology of the SUSY Higgs bosons varies in a smooth way as  $M_A$  is varied. The contours of Higgs mass over the MSSM parameter space are shown in Fig. 2.19 [52]. If  $M_A < 125$  GeV, then  $A^0$  and  $h^0$  are close in mass; if  $M_A > 125$  GeV, then  $M_A \simeq M_H$  and we begin to approach the large  $M_A$  limit. However, if  $M_A < 230$  GeV, then all of the MSSM Higgs bosons should still be observable at the NLC with  $\sqrt{s} = 500$  GeV. If  $M_A > 230$  GeV, it is possible that, at the  $\sqrt{s} = 500$  GeV stage of the NLC, only the lightest SUSY Higgs  $h^0$  may be observable *and* it would have production rates virtually indistinguishable from those of a minimal Standard Model Higgs boson. The remaining Higgs states could be discovered at higher  $\sqrt{s}$ , and there are also precision tests available, to be described later, which could distinguish a Standard Model Higgs from a supersymmetric Higgs. However, since the  $h^0$  will result in decay topologies similar to that of the SM Higgs, if this lightest  $h^0$  is not observed, then the MSSM is categorically ruled out. If the  $h^0$  is not seen below 150 GeV, the more general supersymmetry models incorporating grand unification are also excluded.

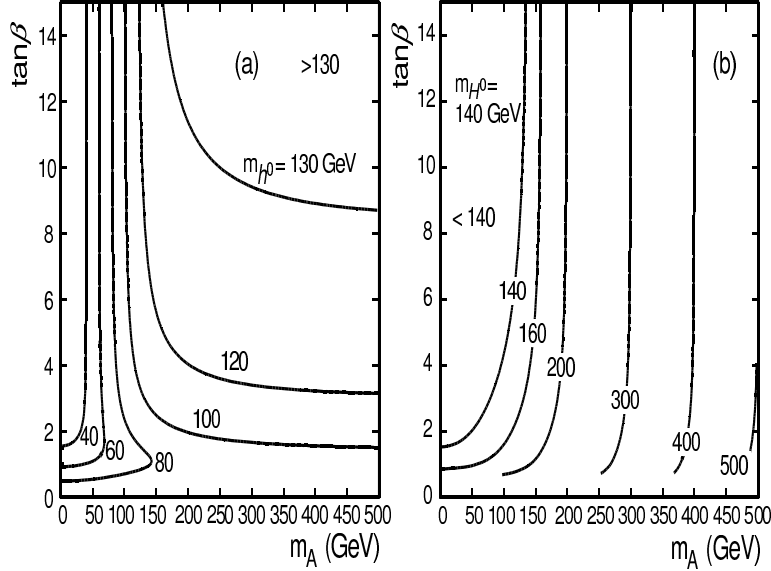


Figure 2.19: Contours of the values of (a)  $M_h$  and (b)  $M_H$  in the MSSM for  $m_t = 180$  GeV, assuming  $m_{SUSY} = 1$  TeV and maximal top squark mixing.

In general, for an intermediate mass boson, the branching ratio for a minimal SM Higgs boson to  $b\bar{b}$  is very close to that of the light  $CP$ -even state  $h^0$ . For large values of  $\tan\beta$ , the other neutral MSSM Higgs bosons decay predominantly into  $b\bar{b}$ , with a 3% branching ratio into  $\tau^+\tau^-$ . This simple pattern becomes more complex for smaller values of  $\tan\beta$  [51] with modes such as  $H^0, A^0 \rightarrow t\bar{t}$  (for  $M_{A^0} \approx M_{H^0} > 2m_t$ ) and  $H^0 \rightarrow h^0h^0$  and  $A^0 \rightarrow Zh^0$  (for  $M_{A^0} \approx M_{H^0} < 2m_t$ ) becoming more important. Despite more complicated cascade decays into lighter Higgs states, the bottom line remains clear: There should be plenty of jets from  $b$ -quarks to tag and elucidate signals. A case in point is the spectacular decay of  $H^0A^0$  into six  $b$  jets  $H^0 \rightarrow h^0h^0, h^0 \rightarrow b\bar{b}$ . Most final states decay into at least four  $b$ -quark jets, underlining the overwhelming importance of  $b$ -tagging in experimental studies. An interesting case deserving further study in simulations is the heavy Higgs decay into  $t\bar{t}^{(*)}$ .

## Experimental Studies

All of the topologies of Fig. 2.16 can be explored in the MSSM with the  $h^0$  taking the role of the Standard Model Higgs boson. A repetition of the analyses described earlier either would observe a single  $h^0$  similar to that of the SM Higgs, or, if  $\sin^2(\beta - \alpha) \simeq 0.5$ , would observe both the  $h^0$  and  $H^0$  states as shown in Fig. 2.20a [48].

An identical preselection for a four-jet topology can be used to search for  $HA$ . We require in this case that all four jets in  $(H^0 \rightarrow b\bar{b})(A^0 \rightarrow b\bar{b})$  be tagged as  $b$  jets. For large enough  $M_A$  and  $\tan\beta$ , we have  $M_A \simeq M_H$ , and we can demand that the two jet-pair masses of the

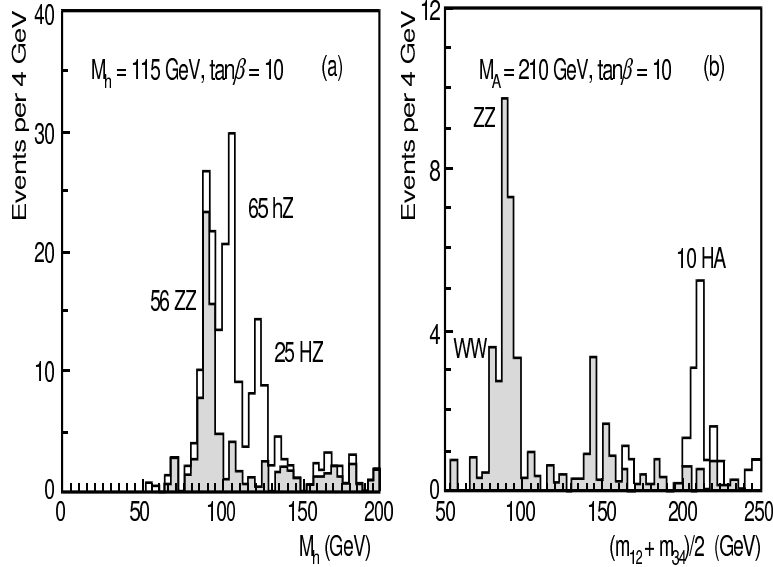


Figure 2.20: (a) Jet masses recoiling from a reconstructed  $Z^0$  after  $b$  tagging for  $\sin^2(\beta - \alpha) \simeq 0.5$ , and integrated luminosity of  $10^{-1}$  fb; (b) average of the two jet-pairs closest in invariant mass in an identified  $b\bar{b}b\bar{b}$  final state with  $M_A = 210$  GeV (adapted from [48]).

possible combinations to be close to equal. Then a signal as shown in Fig. 2.20b is possible. Since all the neutral SUSY Higgs decay into  $\tau^+\tau^-$  at some level, it is possible to observe all three MSSM states in a single analysis by looking at the invariant mass of both the  $\tau^+\tau^-$  and  $q\bar{q}$  in the  $\tau^+\tau^-q\bar{q}$  final state. In Fig. 2.21, we show the regions of plane of  $M_A$  versus  $M_h$  in which it is possible to observe all three neutral Higgs states of the MSSM at a linear collider with  $\sqrt{s} = 500$  GeV, or, conversely, the region where only the  $h^0$  can be observed [53].

In theories with multiple Higgs doublets such as the MSSM, searches for the charged Higgs bosons  $H^\pm$  are also important. An  $e^+e^-$  collider should be able to better resolve the hadronic decays of the  $H^\pm$  compared to a hadronic collider, and all of the expected final states  $H^+H^- \rightarrow c\bar{s}c\bar{s}, l\bar{l}l\bar{l}b$ , plus the easier topologies of  $c\bar{s}\tau^-\nu$  and  $\tau^+\nu\tau^-\bar{\nu}$  should be observable. A detailed simulation analysis [54] at  $\sqrt{s} = 500$  GeV with an integrated luminosity of  $10 \text{ fb}^{-1}$ , which makes heavy uses of  $b$ -tagging, has shown that one can establish a signal over the  $e^+e^- \rightarrow t\bar{t}$  and  $W^+W^-$  background in all of these channels. The results show a detection sensitivity for charged Higgs bosons up to about 210 GeV at  $\sqrt{s} = 500$  GeV, independent of decay mode. These conclusions can be strengthened further by adding the decay  $t \rightarrow bH^+$ . The bottom line is that if the  $A^0$  is lighter than about 200 GeV, then the  $H^\pm$  should be observable also.

If one is considering SUSY Higgs bosons, one should allow for the possibility of their decay into other SUSY particles. As an example, it is possible for  $h^0$  or  $H^0$  to decay into a pair of the lightest neutralinos (mixtures of fermionic partners of the  $Z$  and  $\gamma$ ) that would be stable and neutral. The result would be an “invisible” decay of the Higgs. This topology

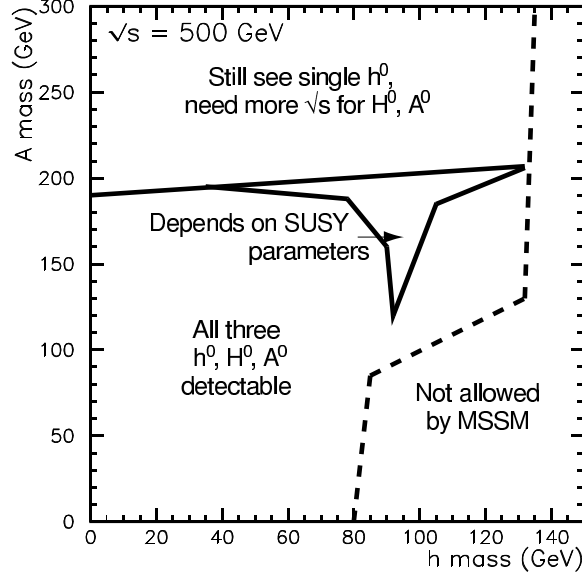


Figure 2.21: Regions of simultaneous detectability of  $h^0$ ,  $H^0$ , and  $A^0$  at center-of-mass energy of 500 GeV [53].

can be identified in the same way as described previously by studying the missing mass in a  $hZ$  or  $HZ$  event where the  $Z$  decays into a pair of electrons or muons. Both missing mass resolution and backgrounds (smaller direct  $Z\nu\bar{\nu}$  cross section) improve with lower center-of-mass energy, and such an analysis would benefit from running at  $\sqrt{s} \simeq 300$  GeV. The possibility of SUSY Higgs decays into other SUSY particles [51] such as SUSY partners of quarks and leptons warrant further experimental simulations.

## 2.4.5 Determination of Properties of Higgs Bosons

### Mass Measurement

To measure the mass of one or more of the possible Higgs bosons, one would probably optimize the running conditions to have smaller center-of-mass energy, to improve momentum resolution and to go to the peak of the cross section. For an intermediate mass Higgs,  $\sqrt{s} = 200\text{--}300$  GeV is appropriate. Under these conditions, one can precisely measure the recoil mass in  $e^+e^- \rightarrow Z^0 h^0$  events opposite to the reconstructed leptonic decay  $Z^0 \rightarrow e^+e^-$  or  $\mu^+\mu^-$ . Other modes, such as the four-jet topology, can also be employed. In all cases, kinematic fitting would be used to constrain the leptons or jets from a  $Z^0$  to reconstruct to  $M_Z$  and to allow for missing  $E_\gamma$  along the beam axis. A typical jet-jet mass resolution of  $\sigma_M \simeq 2.0$  GeV can be achieved assuming the excellent momentum resolution of  $\sigma_{p_t}/p_t = 1 \times 10^{-4} \oplus 0.1\%$  envisaged for the JLC detector [47]. For our NLC detector design, we could achieve  $\sigma_M \simeq 3.9$  GeV, as shown in Fig. 2.22. The differences between detector designs are much smaller when kinematic constrained fitting is included in the analysis. The

JLC-type detector has been estimated to provide a estimated precision on the Higgs mass of approximately 0.1% for  $\sqrt{s} = 300$  GeV,  $f L \cdot dt = 30 \text{ fb}^{-1}$ , and a 2.0% full width beam energy spread [55]. On the other hand, the NLC-type detector gives  $\Delta M_h \leq 160$  MeV up to  $M_h \simeq 160$  GeV with  $50 \text{ fb}^{-1}$  at  $\sqrt{s} = 500$  GeV.

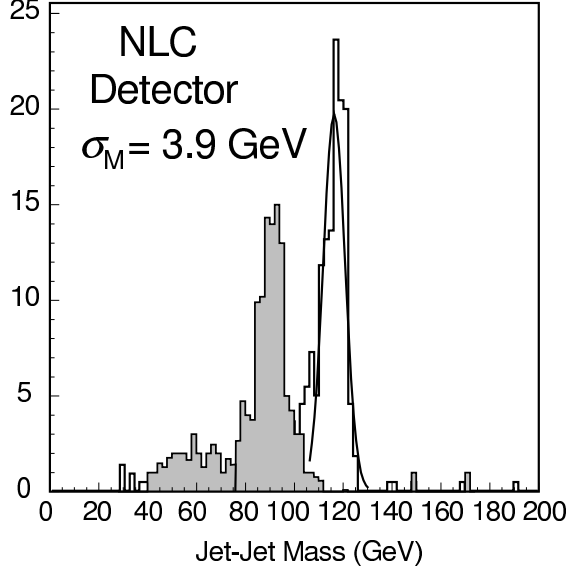


Figure 2.22: Mass resolution of  $\sigma_M \simeq 3.9$  GeV in the jet-jet invariant mass for jets from Higgs decay assuming the performance of a NLC detector (see text) for a simulated signal (open histogram) of a 120 GeV SM Higgs boson and all known backgrounds (shaded histogram) at 300 GeV with  $10 \text{ fb}^{-1}$ .

Once  $M_H$  is known precisely, it can be used as an input to check the experimental measurements of branching ratios and the production cross section with Standard Model predictions. Its value can also be compared to the theoretical value obtained from precision electroweak measurements, combined with the measurements of  $M_W$  and  $m_{top}$  expected from a linear collider.

## Cross Section Measurement

Measuring the production cross section of the Higgs provides one way of disentangling a SM Higgs boson from a SUSY Higgs, if one can observe the cross section suppression due to mixing

$$\sigma(e^+e^- \rightarrow h^0 Z^0) = \sin^2(\beta - \alpha) \cdot \sigma(e^+e^- \rightarrow h_{SM}^0 Z^0).$$

A distinct advantage of  $e^+e^-$  linear colliders over hadronic colliders is the ability to almost unambiguously tag the  $Z^0$  in  $hZ$  events and being able to study all of the decays  $h^0 \rightarrow X$  with small backgrounds. Both total absolute cross sections and individual Higgs branching ratios can then be measured. By using leptonic decays of the  $Z^0$  and kinematical fitting,

the absolute production cross section can be measured [55] with a precision of 7% with an integrated luminosity of  $30 \text{ fb}^{-1}$  and to 5% with  $50 \text{ fb}^{-1}$ . However it should be kept in mind that for a large area of SUSY parameter space, the SUSY Higgs cross section is less than 10% different from the SM Higgs cross section.

## Spin-Parity and CP Determination

In principle, the spin and parity of the Higgs boson can be found by studying both the production angular distribution of the Higgs and also the resulting angular distribution of the decay products of the  $Z^0$  in its rest frame in  $HZ$  events. In the high energy limit, Table 2.6 shows the expected angular distribution of scalar (*e.g.*,  $h^0$ ,  $H^0$ ) and pseudoscalar (*e.g.*,  $A^0$ ) Higgs bosons. In the table,  $\theta$  is the production angle of the Higgs boson and  $\theta_*$  is the polar angle of the fermions from  $Z$  decay measured in the  $Z$  rest frame. In practice, however, a purely CP-odd Higgs boson couples to  $ZZ$  only at the one-loop level, and then the  $ZA$  cross section would be very small. For a Higgs boson that is a mixture of CP-even and CP-odd components, the production would mainly be sensitive to the CP-even part, and the angular distributions would not reveal the CP-odd component [56].

Table 2.6: Expected angular distributions for Higgs bosons with different spin-parity.

	Scalar, $0^{++}$	Pseudoscalar, $0^{-+}$
$d\sigma(\epsilon^+\epsilon^- \rightarrow HZ^0)/d\cos\theta$	$\propto \sin^2\theta$	$\propto (1 - \sin^2\theta)$
$d\sigma(Z^0 \rightarrow f\bar{f})/d\cos\theta_*$	$\propto \sin^2\theta_*$	$\propto (1 \pm \cos\theta_*)^2$

A much better way to determine the Higgs'  $CP$  character is with polarized  $\gamma\gamma$  collisions [57, 58]. In this technique, which we will discuss in detail in Section 9.2, the Higgs boson is produced as an  $s$ -channel resonance. Then it is possible to study the angular correlations of the decay products of the resonance in decays such as  $H \rightarrow \tau^+\tau^-$  and  $t\bar{t}$ . By spin analyzing the subsequent decays  $t \rightarrow b\ell\nu$  for top quarks from heavy Higgs boson decay, and  $\tau \rightarrow \pi\nu$  or  $\tau \rightarrow \rho\nu$  for  $\tau$ 's from intermediate mass Higgs decay, a  $CP$ -even state and  $CP$ -odd state can be distinguished [56, 59]. This  $CP$  state separation is much better in the angular correlations between top quark decay products.

## Branching Ratio Measurements

The measurement of the branching ratios of any observed Higgs boson is an essential ingredient to understand the nature of the symmetry breaking and to make predictions about other aspects of the Higgs sector. This is especially when only a single neutral Higgs is observed, which might be either the Standard Model Higgs or the lightest neutral Higgs from SUSY.

The clean environment in  $e^+e^-$  annihilation permits one to tag a  $Z^0$  in one hemisphere, and then observe the decay  $h^0 \rightarrow X$  in any decay mode in the opposite hemisphere. An example of such an analysis [49] at  $\sqrt{s} = 400$  GeV, simulating an SLD-like detector, first identifies a  $Z^0$  in a  $HZ$  event and then considers those decays where the recoiling Higgs decays into jets. The Higgs decays to two jets can be separated by flavor by counting the number of tracks with a significantly large impact parameter:  $b_{norm} = b/\sigma_b > 3$ , where  $b$  is the impact parameter and  $\sigma_b$  is the error on  $b$ . The decay  $h \rightarrow WW^{(*)}$  is identified by demanding that the event be consistent with containing six jets, and that a jet pair with invariant mass close to the  $W$  mass is found. With  $50 \text{ fb}^{-1}$  of data,  $Br(h \rightarrow b\bar{b})$  can be measured to a statistical precision of 7%, and branching ratios into  $WW^*$  and  $(c\bar{c} + gg)$  to 24% and 39% respectively. These relative errors are shown superimposed upon the Standard Model values in Fig. 2.23a. The figures also shows the variation in branching ratios that one would expect from the variation of  $\tan\beta$ . In the MSSM, it is very difficult to arrange such a large variation in  $\tan\beta$  without a compensatory variation in  $\alpha$ , but the figure shows the utility of this measurement in Higgs studies in a more general context. For the comparison of the Standard Model Higgs boson to the MSSM, one should consult Fig. 2.23b, where the branching ratio of a light Higgs boson into  $b\bar{b}$  is compared for these two possibilities over the MSSM parameter space.

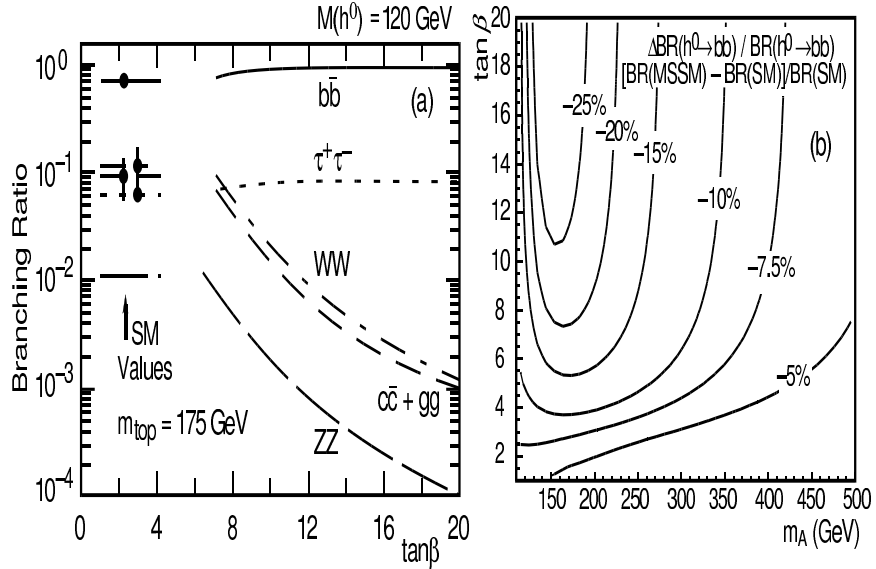


Figure 2.23: (a) Expected errors on the Standard Model branching fractions compared to those predicted for a 120 GeV  $h^0$  MSSM Higgs boson; (b) contour lines of fractional deviation of  $Br(h^0 \rightarrow b\bar{b})$  ( $m_t = 175$  GeV,  $m_{SUSY} = 1$  TeV).

An interesting quantity [61] is the ratio of branching ratios to  $c\bar{c}$  versus  $b\bar{b}$ . At tree level,

$$\frac{Br(h \rightarrow c\bar{c})}{Br(h \rightarrow b\bar{b})} \approx \frac{m_c^2}{m_b^2} \cdot \left( \frac{M_h^2 - M_A^2}{M_A^2 - M_Z^2} \right)^2,$$

where  $m_c$  and  $m_b$  are the  $c$  and  $b$  quark masses respectively. (We should note that this formula can receive substantial radiative corrections in some regions of the MSSM parameter space.) If the branching ratios indicated are measured along with  $M_h$ , it is possible to estimate  $M_A$ . In a simulation study of this measurement [62] at  $\sqrt{s} = 300$  GeV,  $HZ$  events are selected for each decay mode of the  $Z^0$ , and the decay mode of the Higgs is determined using three-dimensional impact parameters. Flavor tagging is performed by selecting charged tracks that satisfy  $b/\sigma_b \geq 2.5$  and counting the number in each jet from the Higgs decay. For  $M_H = 120$  GeV,  $50 \text{ fb}^{-1}$  of data, and assuming 90% polarization of the electron beam, the statistical error on the ratio of branching ratios  $Br(h \rightarrow c\bar{c} + gg)/Br(h \rightarrow b\bar{b})$  would be 20.4%, varying with the Higgs mass as shown in Fig. 2.24a. This does not include a substantial systematic uncertainty from  $m_c/m_b$ , which we believe will be reduced in the next few years through lattice gauge theory calculations. Then, as shown in Fig. 2.24b, this measurement could be sensitive to  $A^0$  masses up to 400 GeV, well above the maximum kinematic reach of a 500 GeV collider. Observation of the  $A^0$  in this way would help to plan the next step in energy.

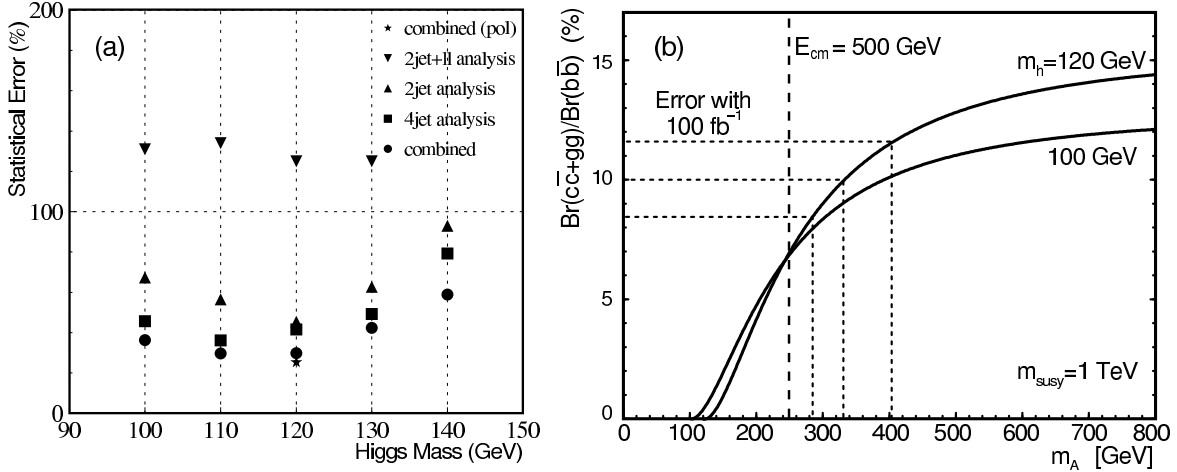


Figure 2.24: (a) Statistical error with  $50 \text{ fb}^{-1}$  of data on  $Br(h \rightarrow c\bar{c} + gg)/Br(h \rightarrow b\bar{b})$  as a function of Higgs mass; (b) implications for estimation of  $A^0$  mass.

For the decay  $h \rightarrow \gamma\gamma$ , it is difficult to measure the branching ratio at an  $e^+e^-$  collider because this mode is relatively rare. However, it should be possible to measure the absolute partial width  $\Gamma(h \rightarrow \gamma\gamma)$  by exploiting the ability of an electron collider to be run as a  $\gamma\gamma$  collider. This measurement is discussed in Section 9.1.

## Determination of Higgs Total Width

In the preceding sections, we have indicated many ways in which measurements at the NLC can distinguish between the Standard Model Higgs and the light Higgs  $h^0$  of the MSSM. There are also a number of quantities at the LHC which are sensitive to this difference, as

outlined in [35]. However, to obtain the complete set of partial width of the Higgs boson in a model-independent way, measurements from LHC must be combined it with data both from  $e^+e^-$  and  $\gamma\gamma$  collisions at the NLC. A possible procedure is the following. First determine  $Br(b\bar{b})$  from  $Zh$  events and combine with  $\sigma(WW \rightarrow h) \cdot Br(b\bar{b})$  both measured at the NLC to obtain the  $WWh$  coupling. Alternatively, a measurement of  $\sigma(e^+e^- \rightarrow Zh)$  at the NLC gives the  $ZZH$  coupling and the ratio of the  $WWh$  and  $ZZh$  couplings given by  $M_W^2/M_Z^2 = \cos^2 \theta_W$  also gives the  $WWh$  coupling. This coupling and a measurement of  $\sigma(Wh) \cdot Br(\gamma\gamma)$  at the LHC can be used to determine  $Br(\gamma\gamma)$ . Therefore one can combine  $Br(b\bar{b})$  with the  $\gamma\gamma$  collider measurement of  $\sigma(\gamma\gamma \rightarrow h) \cdot Br(b\bar{b})$  to obtain  $\Gamma(h \rightarrow \gamma\gamma)$ . We can then finally compute the total width  $\Gamma_h^{\text{tot}} = \Gamma(h \rightarrow \gamma\gamma)/Br(\gamma\gamma)$  and  $\Gamma(h \rightarrow b\bar{b}) = Br(b\bar{b})\Gamma_h^{\text{tot}}$ . A simpler route exists using only  $e^+e^-$  data when the Higgs boson is heavy enough that the branching ratio to  $WW^*$  is relatively large, so that it can be measured accurately. In this case, we can simply measure  $Br(h \rightarrow WW^*)$  and infer  $\Gamma_h^{\text{tot}} = \Gamma(h \rightarrow WW^*)/Br(WW^*)$ . Although the accumulation of errors may be significant, the basic point is that data from all three colliders or from the NLC alone can be combined to complete a *model-independent* determination of the properties of a light Higgs boson.

## 2.4.6 Summary

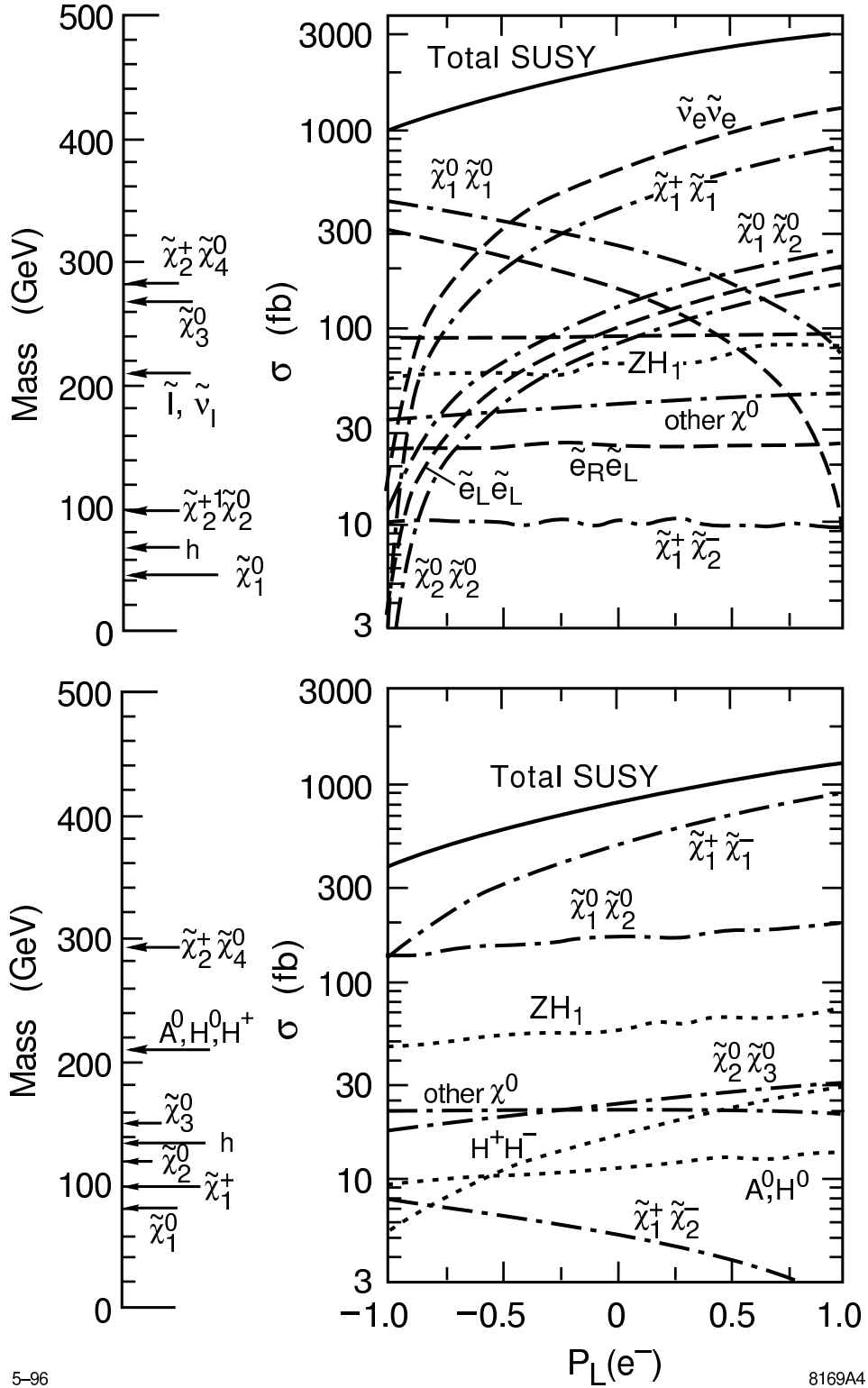
From the studies described, the discovery of a Standard Model intermediate-mass Higgs boson at an  $e^+e^-$  linear collider at  $\sqrt{s} = 500$  GeV can be easily achieved with an integrated luminosity of only  $10 \text{ fb}^{-1}$ . Such a machine allows the detection of *at least* the lightest MSSM Higgs  $h^0$ , if not all three SUSY neutral states. If the lightest Higgs is not observed, then not only is the Minimal Supersymmetric Standard Model ruled out, but also the general idea that the Higgs boson is a fundamental particle up to the unification scale is called into question. If the  $A^0$  is not kinematically accessible at  $\sqrt{s} = 500$  GeV, then the measurement of  $h^0$  branching ratios can give hints of the values of  $M_A$  and  $\tan \beta$  and tell us where to go next in energy. For definitive evidence,  $\sqrt{s} > 2M_A$  would still be needed. For Higgs bosons above the intermediate mass range, their decay into pairs of vector bosons makes them straightforward to detect at the NLC as at the LHC; however, more up-to-date experimental simulations are needed. Just as important as its ability to discover the Higgs boson is the ability of the linear collider to make precision measurements of the properties and couplings of a Higgs boson. Even if the Higgs boson is discovered earlier at LEP2 or at the LHC, we will need the NLC to learn its complete story.

## 2.5 Supersymmetry

To build a complete unified theory with a fundamental Higgs boson, one is led to introduce supersymmetry, the symmetry between fermions and bosons in space-time. Supersymmetry is the only known principle with sufficient structure to allow the construction of grand unified theories in which fundamental scalar particles can naturally be very light compared to the unification scale. Supersymmetric unification models explain the values of the Standard Model coupling constants as measured at  $Z^0$  energies, and also incorporate a mechanism of electroweak symmetry breaking associated with the heavy top quark. General reviews of supersymmetric models can be found in [36, 37, 63, 64]. Supersymmetry also offers the more speculative but tantalizing possibility of a connection between phenomena observable at collider energies and string theory and other profound mathematical theories of the fundamental forces [65, 66].

In this section, we will examine the manner in which supersymmetry (SUSY) might manifest itself at a 0.5-1.0 TeV  $e^+e^-$  Linear Collider (NLC). Our discussion here is part of a broader, and continuing, investigation. At present, our study is being carried out within the supersymmetry scenario based on the minimal supergravity model with gauge coupling unification and radiative electroweak symmetry breaking (SUGRA). We have calculated most of the relevant cross sections and angular distributions for the production and decay of supersymmetric particles, and we include a report of them as an appendix [67]. Because of the difficulty of knowing where and how supersymmetry will manifest itself, we must study the phenomenology of supersymmetry over a wide range of its parameters. In this study, we have chosen five points in the parameter space of the SUGRA model which illustrate qualitatively different possibilities for the spectrum of new particles [67]. Because of the power of the experimental tools offered by the NLC, our goals are much more ambitious than simply to discover the existence of supersymmetry. We would like to measure the masses of supersymmetric particles with precision, and determine the underlying values of the basic parameters of the theory. In the most optimistic scenario, the extrapolation of these parameters to the unification scale would give evidence into the details of the fundamental unified model [68].

The number of supersymmetric particles is quite large. Hence, it is typical that many of these particles will be produced in the same data sample at a particular energy center-of-mass energy. One of the properties of  $e^+e^-$  linear colliders is that the electron can be longitudinally polarized and its orientation can be changed at will. Already, the SLC provides an electron beam with 77% polarization. We expect that, in the future, this magnitude can be increased substantially. The ability to have electron beams with high longitudinal polarization is very useful to discriminate between the various supersymmetric signals and to understand and remove the Standard Model background processes [69]. This can be seen by examining the standard model cross sections as a function of polarization, shown already in Fig. 2.3, and comparing these to the polarization-dependence of the cross sections for the supersymmetric production processes, shown for two representative points in Fig. 2.25. Having a 90% longitudinally polarized electron in the right handed mode will reduce the production



5-96

8169A4

Figure 2.25: The cross section of Supersymmetric particle production at  $E_{\text{cm}} = 0.5$  TeV as a function of the electron polarization for points 3, 4 in our parameter space.

rate of Standard Model background processes such as  $W^+W^-$  pair production by an order of magnitude while enhancing some of the supersymmetric particle signals. The left-handed supersymmetric particles, like the Standard Model background, are also suppressed, while the right-handed ones are enhanced. This is seen in Fig. 2.25. Hence, by varying the polarization we can determine which of the supersymmetric particles are giving us a particular signal. Polarization of the positrons could give an additional advantage. For example, if we could collide totally right-handed electrons with totally left-handed positrons, all of the standard model backgrounds from  $e^+e^-$  annihilation processes would disappear, while the supersymmetric signals from  $\tilde{e}_R^-\tilde{e}_R^+$  production would remain. (Some background would also remain due to two-photon reactions [70].) An additional handle on our ability to discriminate among the various supersymmetric signals is their different angular distributions [67]. These distributions for a typical case are shown in Fig. 2.26. A third powerful discriminating tool is the adjustment of the center-of-mass energy. Once one has an estimate of the masses of the lightest supersymmetric particles, it is advantageous to decrease the energy of the collider so that only these lightest states are produced, measure their properties at this lower energy, and then increase the energy of the collider systematically.

### 2.5.1 Supersymmetry Signals at the NLC

In our study, we have generated signal and background processes using the simulation program ISAJET [6]. This program allows for both electron and positron longitudinal polarization. The influence of the detector is accounted for by smearing the generated momenta and directions of the particles produced in the simulation with resolution functions as described in Section 2.

The spectrum of supersymmetric particles for the five parameter sets that we have chosen for detailed study are exhibited in Table 2.7. These spectra are computed consistently from a supergravity model with  $m_t = 180$  GeV. The values of the underlying parameters for these scenarios is given in [67].

In each of the five cases, the lowest mass supersymmetric particle is the  $\chi_1^0$ . In the class of models we discuss, there is a conserved R-parity which implies that this particle is stable. It then passes through the detector without leaving a signal. This particle is in all cases sufficiently massive that it carries away significant missing energy. On the other hand, Standard Model background processes can mimic this signal because, as a result of their peaked differential cross-section in the forward and backward directions [67], many of the particles in the final state go along the beam direction. Also it is possible that neutrinos can carry away a sizable portion of the energy, or that the event is mismeasured due to the detector resolution.

In Fig. 2.27 we show the expected observed energy for the Standard Model processes  $e^+e^- \rightarrow W^+W^-, Z^0Z^0, q\bar{q}$  after a requirement that at least three particles be present in each hemisphere. This allows us to avoid including the  $e\nu W$  final state and most of the events where the  $W$ 's and  $Z$ 's decay into leptons and neutrinos; only a few events with  $\tau$  in the

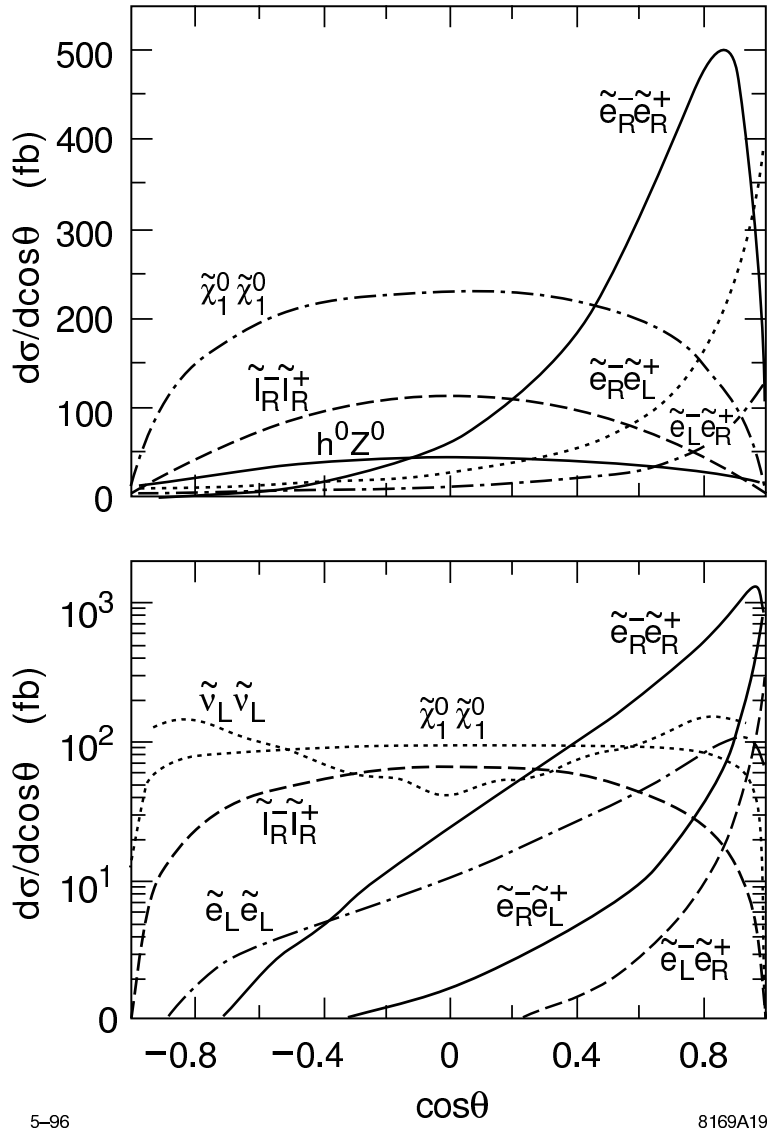


Figure 2.26: The differential cross section of supersymmetric particle production for an 80% polarized right handed electron at  $E_{cm} = 0.5$  and 1.0 TeV for point 2 in our parameters list.

Table 2.7: Supersymmetric particle masses at five representative points in the parameter space of phenomenological supergravity models.

<b>Parameter Set</b>	1	2	3	4	5
$\chi_1^0$	85.87	128.51	44.41	77.83	57.00
$\chi_2^0$	175.24	257.05	96.73	115.29	111.21
$\chi_3^0$	514.96	549.08	267.81	146.84	440.03
$\chi_4^0$	523.78	556.07	284.18	292.40	460.12
$\chi_1^\pm$	175.12	257.02	96.10	96.06	109.82
$\chi_2^\pm$	522.82	555.72	282.52	292.45	457.09
$h^0$	84.86	92.24	68.82	130.58	102.15
$H^0$	766.47	698.24	389.39	201.72	619.21
$A^0$	762.32	693.30	381.75	200.00	616.45
$H^\pm$	765.70	697.05	388.81	214.75	620.52
$\tilde{q}_L$	605.23	670.84	317.23	1000.00	464.04
$\tilde{b}_L$	516.58	621.43	272.31	1000.00	384.70
$\tilde{t}_1$	417.65	537.12	265.55	923.13	179.85
$\tilde{q}_R$	605.23	670.84	317.23	1000.00	464.04
$\tilde{b}_R$	597.15	655.70	313.40	1000.00	457.79
$\tilde{t}_2$	547.20	655.21	328.15	1099.35	495.72
$\tilde{l}_L^-$	425.96	238.35	215.72	1000.00	320.69
$\tilde{\nu}_L$	421.43	230.16	206.63	1000.00	314.65
$\tilde{l}_R^-$	408.80	156.97	206.54	1000.00	307.45
$\tilde{g}$	552.19	760.16	298.15	900.00	428.03

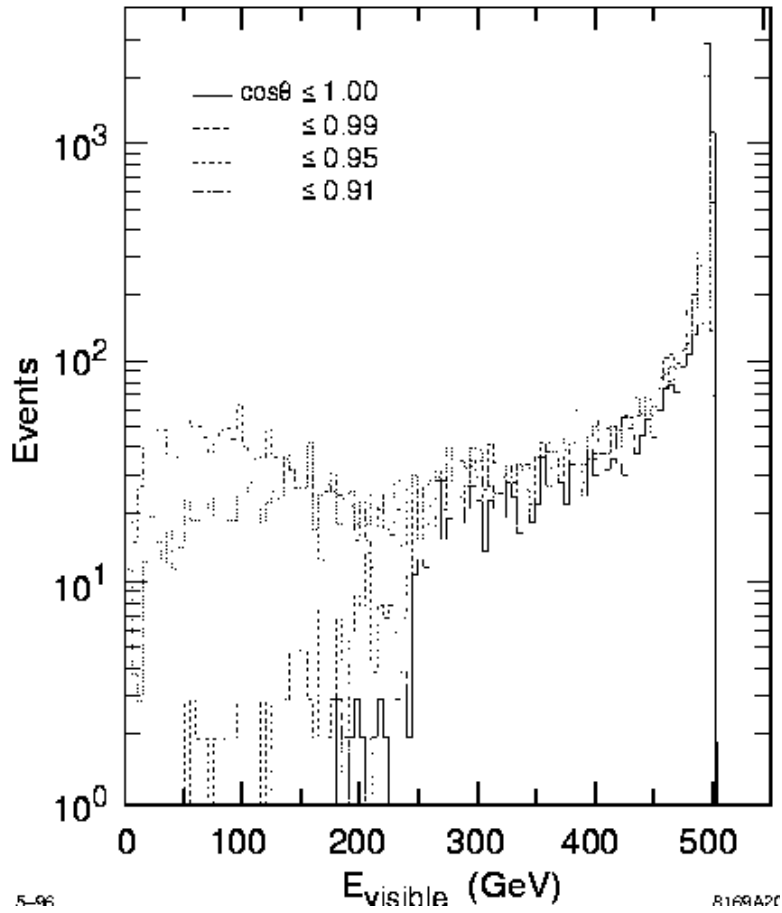


Figure 2.27: The Visible Energy for Standard Model final states  $W^+W^-$ ,  $Z^0Z^0$ ,  $q\bar{q}$  for various calorimetry coverage. We require that there be at least 3 particles in each hemisphere.

final state remain. The figure shows the effect of various assumptions about the calorimetric coverage in  $\cos(\theta)$ , to determine how much energy is lost in the beam direction. We note that the tail of events with low visible energy ( $E \approx 100$  GeV or less) begins to increase noticeably for  $\cos(\theta) < 0.97$  or so. Hence good calorimetric coverage is imperative if we want to use the low visible energy as a signal for supersymmetric particles. We do not smear the particles in this plot to determine the true loss of particles down the beam direction. The detector design presented in this report has calorimetric coverage down to  $\cos(\theta) = 0.99$ , which, as we will see, is sufficient to allow us to see the signal due to supersymmetric particles.

We have made a study of the signals seen in the various sets of SUGRA parameters [67]. We show here some of the results for the signal to background ratios for the SUGRA parameter set 4. In this scenario, the main signals are due to the pair-production of the charginos  $\chi_1^\pm$  and the neutralinos  $\chi_1^0, \chi_2^0$ . The visible (observed) energy for these signals and the others [67] is shown in Fig. 2.28. The signal is in the region of 100 GeV visible energy; hence our requirement that there needs to be calorimetric coverage down to small angles. In Fig. 2.29 we show the visible energy distribution, properly normalized with the relative cross section for background Standard Model events and signal from supersymmetric events. A small bump can be observed in the region of small visible energy. To isolate the signal due to chargino ( $\chi_1^+ \chi_1^-$ ) production, we require that there be at least five hadrons in each hemisphere. After additional cuts in the data to enhance the signal, we are able to obtain a signal to background ratio of 12 to 1 as shown in Fig. 2.30. This signal is then used to determine the masses of the  $\chi_1^\pm$  and the  $\chi_1^0$  as described below. Similarly, with appropriate cuts we obtain a signal for  $\chi_2^0 \chi_1^0$  production with no background from the Standard Model processes, but, as shown in Fig. 2.31, a background of  $\approx 10\%$  from  $\chi_1^+ \chi_1^-$ . (We expect to reduce this background with further analysis.) The complete observed signal is shown in Fig. 2.32. This can then be used to determine the masses of the  $\chi_2^0$  and  $\chi_1^0$ . It is interesting to check that the two determinations of the  $\chi_1^0$  mass agree. This self consistency would give us confidence that we are seeing the consequences of a consistent model and would encourage us to use the resulting model parameters to predict the masses of the other particles. The levels of signal to background seen in this analysis are typical for scenarios of supersymmetric particle production processes in  $e^+e^-$  colliders.

## 2.5.2 Superparticle Mass Measurements

We will now discuss in more detail the measurement of the masses, spins, and cross-sections of the various possible supersymmetric signals. Some very beautiful studies on these issues have already been reported in [68, 71, 72]. These papers indicate that, indeed, linear collider experimentation provides very powerful methods by which to measure the production and decay parameters of the various supersymmetric particles. This should allow us to uncover which of the various supersymmetric models is the correct one. One recent study [68] has shown that, for slepton or chargino pair-production, we can use the upper and lower limits of the energy spectrum of the secondaries from supersymmetric particle decays to determine these particle masses. In addition, we can use the angular distribution of the signal to

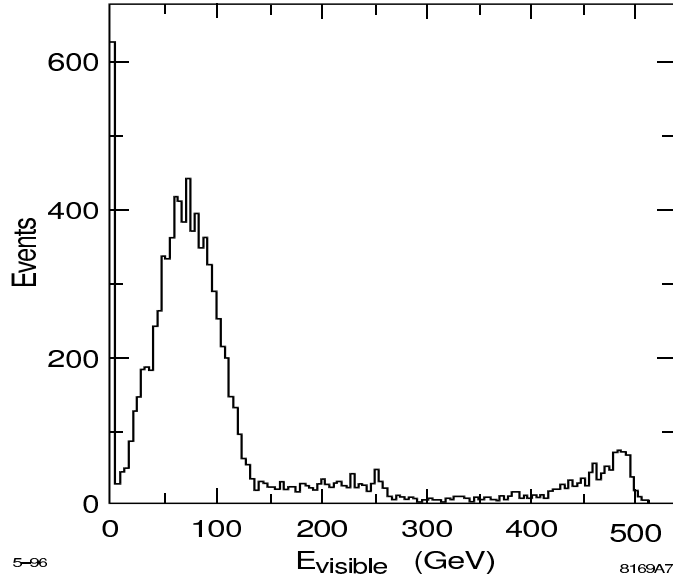


Figure 2.28: The visible energy for the supersymmetric processes defined by the SUGRA parameter set 4 after detector resolution smearing. The peak at 0 is due to  $\tilde{\chi}_1^0\tilde{\chi}_1^0$  and  $\tilde{\chi}_2^0\tilde{\chi}_1^0 \rightarrow \nu\bar{\nu}\tilde{\chi}_1^0\tilde{\chi}_1^0$  processes. The broad small peak at 500 GeV is due to  $Z^0h^0$ ,  $H^+H^-$ , and  $H^0A^0$  final states.

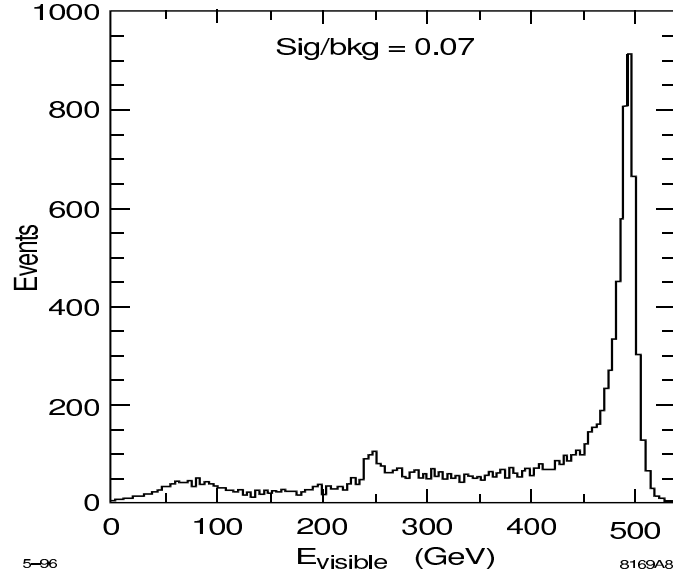


Figure 2.29: The visible energy for the normalized (relative cross-section) SUSY processes associated with SUGRA parameters 4 and the Standard Model processes. The smearing due to detector resolution is included.

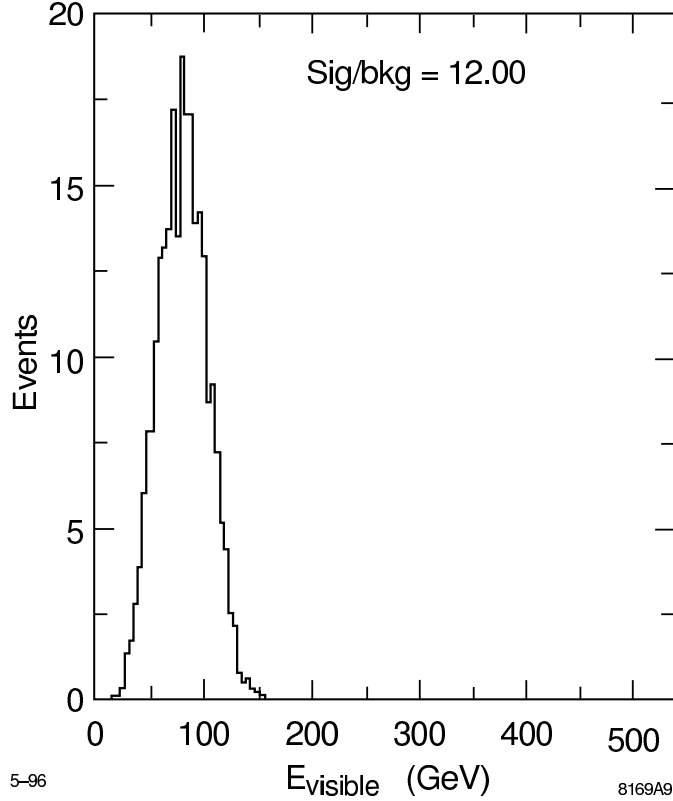


Figure 2.30: The visible energy for the normalized (relative cross-section) SUSY process  $e^+e^- \rightarrow \chi_1^+\chi_1^-$  associated with parameter set 4 and Standard Model processes after cuts to enhance the signal over background. The cuts are that there be only 1 broad jet with  $> 5$  particles and with  $E_{vis} < 80$  GeV in each hemisphere.

say something about the spin of the sparticles producing these distributions. A threshold scan will also differentiate between scalars and fermions by determining whether the energy dependence follows a  $\beta$  or a  $\beta^3$  law.

In this study, we expand on this work by increasing the number of cases that have been studied and attempt to determine how much these measurements constrain the possible region of parameter space. Here we will describe how well we can determine the masses of the supersymmetric particles using the simulated resolution parameters in our detector design. For brevity, we will only consider here the parameters sets 3 and 5. In case 3, the most important supersymmetry cross section for an incident 95% left-hand polarized electron beam is that of sneutrino pair production,  $\tilde{\nu}_e\tilde{\nu}_e$ , as shown in Fig. 2.25. The branching ratio for  $\tilde{\nu}_e \rightarrow e^-\chi_1^+$  is 61%. The  $\chi_1^+$  decays mostly to  $W^+\chi_1^0$ . Hence, 5-10% of the time we can have a final state signal  $e^\mp e^\pm \mu^\pm + 2$  jets. This signal will have hardly any Standard Model background. The energy distribution of the  $e^\mp$  can be used to determine the  $\tilde{\nu}_e$  mass. The  $e^\mp$  energy spectrum, based on a  $20 \text{ fb}^{-1}$  data sample, is shown in Fig. 2.33. The background

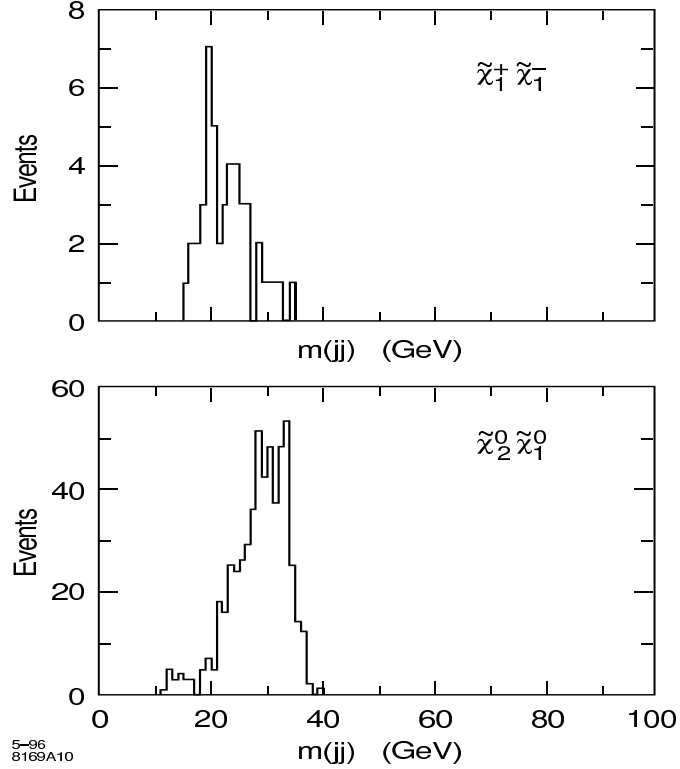


Figure 2.31: The 2-jet mass distribution for the processes  $e^+e^- \rightarrow \chi_1^+\chi_1^- (\chi_1^0\chi_2^0) \rightarrow q\bar{q}\chi_1^0q\bar{q}\chi_1^0 (\chi_1^0q\bar{q}\chi_1^0)$ . The cuts require 2 jets with more than 1 particle in each and both jets in one hemisphere only.  $E_{visible} < 125, 70$  GeV for the two jets, and  $\cos(\theta) < 0.85$  for the thrust axis of the event.

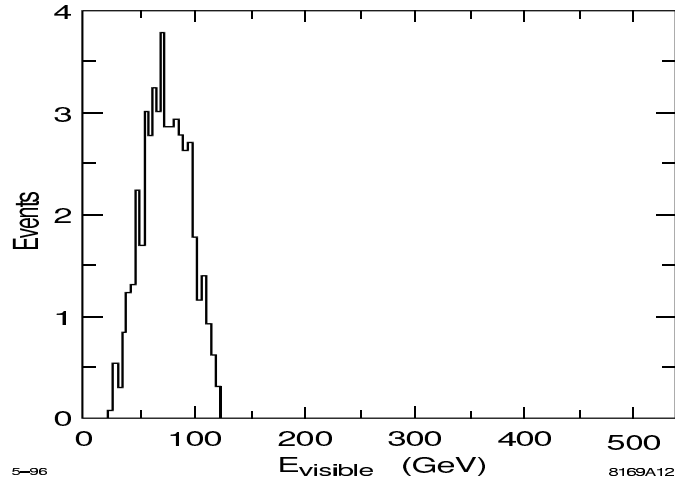


Figure 2.32: The visible energy distribution for the SUSY process  $e^+e^- \rightarrow \chi_2^0\chi_1^0$  associated with parameter set 4 and the Standard Model background processes, after the cuts defined in the previous figure to enhance the signal over background.

is shown by the dotted line. A fit to this energy spectrum leads to the following values for the masses:

$$M_{\tilde{\nu}_e} = 207.5 \pm 2.5 \quad (4) \quad \text{GeV}$$

$$M_{\chi_1^+} = 97.0 \pm 1.2 \quad (2) \quad \text{GeV}$$

at the 68% (90%) confidence level. These results should be compared with the input values, given in the table, of 206.6 and 96.1 GeV respectively.

Another interesting signal is the  $\tilde{e}_L^+ \tilde{e}_L^-$  process in order to determine the mass of the  $\tilde{e}_L$  (left-handed slepton). The useful signal is due to the decay chain  $\tilde{e}_L^- \rightarrow e^- \chi_2^0 \rightarrow e^- Z^0 \chi_1^0 \rightarrow e^- \mu^- \mu^+ \chi_1^0$ . This leads to a final state with one electron, one positron, four muons, and a small visible energy. We can also consider the analogous decay chain for  $\tilde{\mu}_L^+ \tilde{\mu}_L^-$ . We considered these two possibilities together by isolating final states with 6 leptons and missing energy, in which the highest energy leptons are either  $e^+ e^-$  or  $\mu^+ \mu^-$ . This analysis assumes that  $\tilde{e}_L^-$  and  $\tilde{\mu}_L^-$  have the same mass; with higher statistics, a mass splitting would be apparent. The results for an effective 1 year run (50 fb<sup>-1</sup>) is shown in Fig. 2.34. The fit to the lepton energy spectrum gives the following values for the masses:

$$M_{\tilde{e}_L} = 221.6 \pm 5.6 \quad (8) \quad \text{GeV}$$

$$M_{\chi_2^0} = 94.7 \pm 5.3 \quad (10) \quad \text{GeV}$$

at the 68% (90%) confidence level, which are quite close to the input values of 215.7 and 96.8 GeV in spite of the low statistics in this sample. Since  $M_{\tilde{\nu}} - M_{\tilde{e}_L}$  is determined by just  $SU(2)$  symmetry, these measurements lead to a model-independent constraint on the parameter  $\tan(\beta)$  according to the equation:

$$M_{\tilde{\nu}}^2 - M_{\tilde{e}_L}^2 = M_W^2 \cos(2\beta) .$$

In the case of SUGRA parameter 5 we have a series of signals whose masses can be determined. This point includes a low mass stop squark  $\tilde{t}_1$ , a chargino  $\chi_1^+$ , neutralinos  $\chi_1^0$  and  $\chi_2^0$ , and the light Higgs boson  $h^0$ . We measure the  $\chi_1^+$  and  $\chi_1^0$  masses by studying the production process  $e^+ e^- \rightarrow \chi_1^+ + \chi_1^-$ . For a 95% left handed polarized electron the cross-section is  $\approx 0.75$  pb so that for a 1 year run at our standard luminosity we get over  $10^4$  events. The  $\chi_1^+$  decays into the 3 body final states  $q\bar{q}\chi_1^0$  and  $e\nu\chi_1^0$ , with the branching ratios predicted for the Standard Model  $W$  boson decay into the similar channels. Hence, about 68% of the time it will decay into two hadronic jets +  $\chi_1^0$ . To isolate this signal we use similar cuts to those discussed above associated with Fig. 2.30. The resulting  $E_{jj}$  values, the energies of each of the 2 jet systems from the  $\tilde{\chi}_1^+$  decays, has no sharp end point behavior due to the 3 body nature of its decay. Hence we cannot easily use the  $E_{jj}$  spectrum to determine the masses. Since the combined mass of the 2 jets,  $M_{jj}$  does not vary much in this case, and since we have a large sample of events, we can force two body kinematics on this process by selecting a slice of  $M_{jj}$  around a given value, which in our case is chosen to be 30 GeV. Hence the  $E_{jj}$  distribution follows approximately the two body kinematics of the

process  $\tilde{\chi}_1^+ \rightarrow \tilde{\chi}_1^0 + (jj)$  (30 GeV). The  $E_{jj}$  distribution and the best mass fit to the data is shown in Fig. 2.35. The result is:

$$M_{\tilde{\chi}_1^+} = 107.5 \pm 6.5 \text{ GeV}$$

$$M_{\tilde{\chi}_1^0} = 55.0 \pm 3.5 \text{ GeV}$$

at the 68% confidence level. This is to be compared with the input values of 109.8 and 57.0 GeV respectively.

Finally, for parameter point 5, we have also studied determining the mass of the  $\tilde{t}_1$  (stop) quark. Here we note that the process  $e^+e^- \rightarrow \tilde{t}_1^+\tilde{t}_1^- \rightarrow b\tilde{\chi}_1^+\bar{b}\tilde{\chi}_1^-$  occurs with a 100 % branching ratio. Since this cross section hardly depends on the electron polarization we study this case with a 95% right handed polarized electron ( $P_L(e^-) = -0.9$ ) to minimize the background from  $WW$  pair production [67]. We isolate the events with  $\geq 5$  jets, and we select from these events with two tagged  $b$ 's, and no isolated leptons or  $\tau$  jets. Finally we require a missing mass  $> 140$  GeV. For our standard 1 year run we obtain a SUSY signal of 286 events with a  $WW$  background of 36 events. The energy distribution of the  $b$ -jets is shown in Fig. 2.36. This distribution depends on the mass of the  $\tilde{t}_1$  and the mass of the  $\tilde{\chi}_1^+$ . The masses we obtain are:

$$M_{\tilde{t}_1} = 182 \pm 11 \text{ GeV}$$

$$M_{\tilde{\chi}_1^+} = 114 \pm 8 \text{ GeV}$$

to be compared with the input values of 180 and 110 GeV respectively. Other interesting work on squark mass determination [73] has also been carried out.

We hope that in this short presentation we have indicated the effectiveness of an 0.5-1.0 TeV  $e^+e^-$  Linear Collider in determining the masses of the Supersymmetric particles. We have not discussed how to determine the spin of these. This we propose to accomplish where possible by looking at their production angular distribution and by looking at their production behavior as a function of the electron longitudinal polarization. This work will continue in order to determine further what additional parameters need to be determined to be able to guarantee that the signals we observe are due to supersymmetric particles.

### 2.5.3 Supersymmetry Reach of the NLC and LHC

To conclude, we make a brief comparison of the relative reach capabilities of a 0.5-1.5 TeV  $e^+e^-$  Linear Collider and the CERN LHC  $pp$  collider as to their ability to determine whether the observed signals are due to supersymmetric particles. First of all, the NLC, operating at  $E_{\text{cm}} \geq 250\text{-}300$  GeV should be able to search for the light Higgs boson,  $h^0$ , over the entire parameter space range of the minimal supersymmetry model. If the NLC does not observe the  $h^0$ , then this model must be ruled out. In addition, since the  $h^0$  is expected to behave very nearly like a Standard Model Higgs boson, even if it is discovered, it may be difficult to tell if it is a SUSY or Standard Model Higgs. Hence, discovery of the  $h^0$  alone may not be

sufficient evidence for supersymmetry. On the other hand, the NLC has a substantial ability to discover many of the superpartners.

In Fig. 2.37, we show our estimates of the reach of NLC and LHC into the SUGRA parameter space, defined by underlying mass parameters  $m_0$  and  $m_{1/2}$ . In the top figure, we have plotted the contours corresponding to  $\tilde{\ell}_R$  and  $\tilde{\chi}_1^\pm$  masses of 250, 500 and 750 GeV, approximately representing the reach of NLC(0.5 TeV), NLC(1.0) and NLC(1.5) in observing these supersymmetric particles. We also show the reach for supersymmetry recently calculated [74] for the CERN LHC assuming  $10 \text{ fb}^{-1}$  of integrated luminosity. Comparing the two figures we note that the reach of the LHC is larger than that of the NLC at 500 GeV, but its reach is comparable to that of the NLC at 1 TeV. It is important to note that the reactions at NLC and LHC typically access different particles in the supersymmetry spectrum, so the experiments at these colliders should be considered cooperative rather than competitive. In addition, precision measurements of particle properties such as mass, spin, and mixing angles will be much easier at the NLC [68] than at the LHC. The LHC might be able to provide complementary information via squark and gluino production channels which may not be accessible at the NLC.

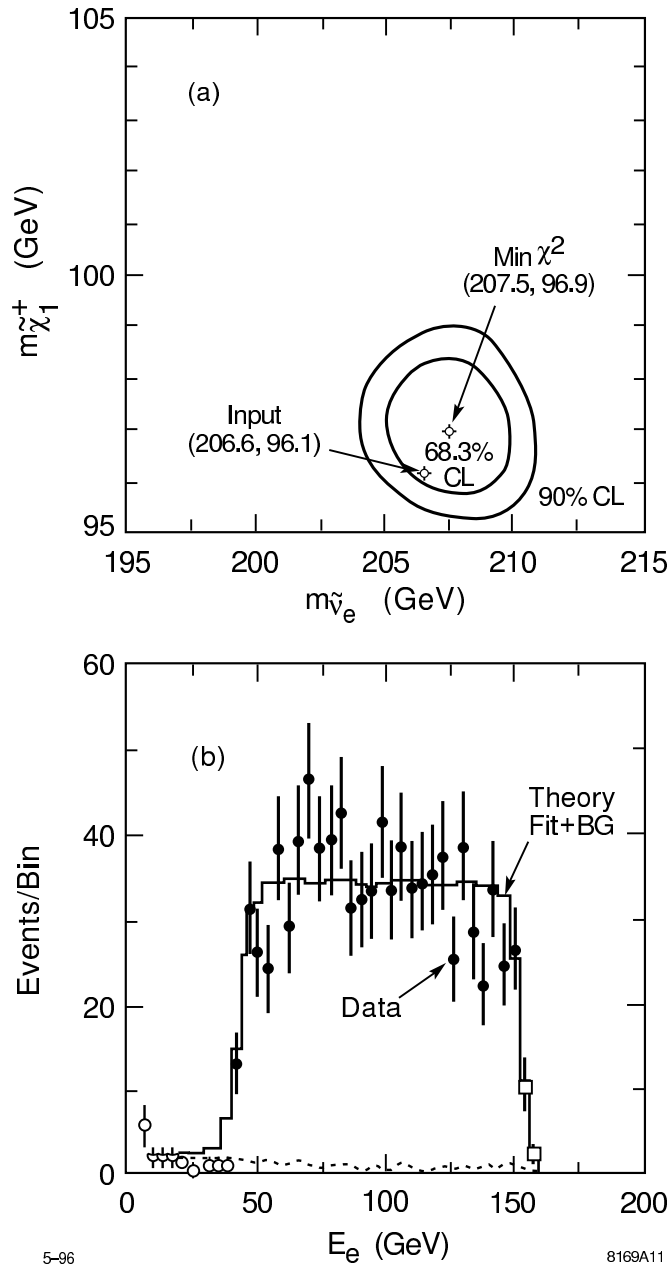


Figure 2.33: The electron energy distribution in the process  $e^+e^- \rightarrow \tilde{\nu}_e\tilde{\nu}_e \rightarrow e^-\chi_1^+e^+\chi_1^- \rightarrow e^-\mu^+\chi_1^0e^+\chi_1^0 + 2 \text{ jets}$  and the fit that determines the mass of the  $\tilde{\nu}_e = 207.5 \pm 2.5$  GeV and the mass of the  $\chi_1^\pm = 97.0 \pm 1.2$  GeV at the 68% C.L.

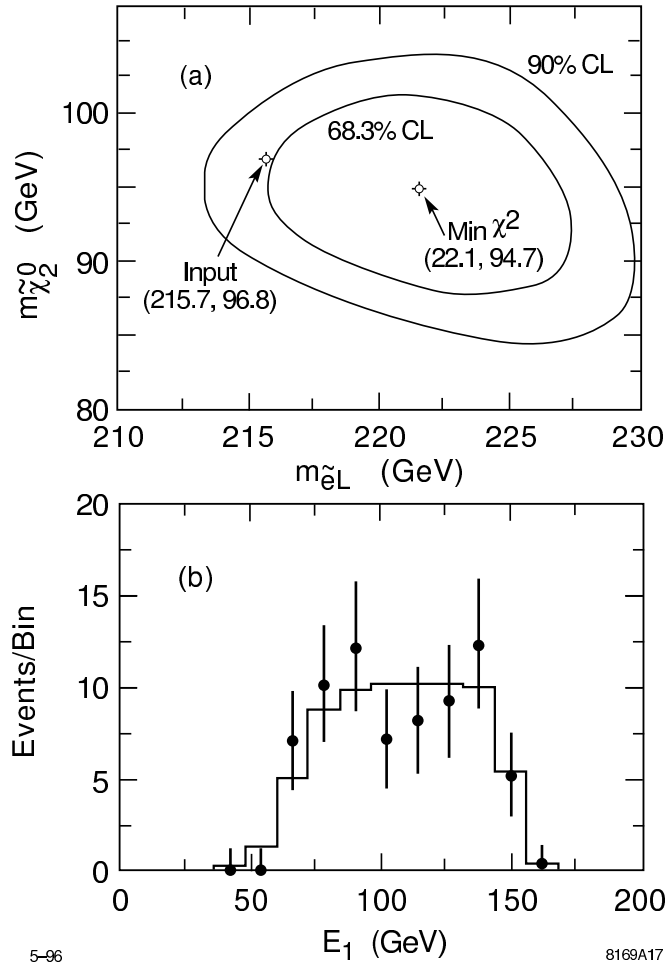


Figure 2.34: The energy distribution of the two highest energy leptons in the process  $e^+e^- \rightarrow \tilde{\ell}_L^- \tilde{\ell}_L^+ \rightarrow \ell^- \tilde{\chi}_2^0 \ell^+ \tilde{\chi}_2^0 \rightarrow \ell^- Z^0 \chi_1^0 \ell^+ Z^0 \chi_1^0 \rightarrow$  six leptons plus missing energy, and the fit that determines the mass of the  $\tilde{\ell}_L$  and the  $\tilde{\chi}_2^0$ . Only those events were considered in which the highest energy leptons were  $e^+e^-$  or  $\mu^+\mu^-$ . The fit gives the mass values  $M_{\tilde{\ell}_L} = 221.6 \pm 5.6$  GeV and  $M_{\tilde{\chi}_2^0} = 94.7 \pm 5.3$  GeV

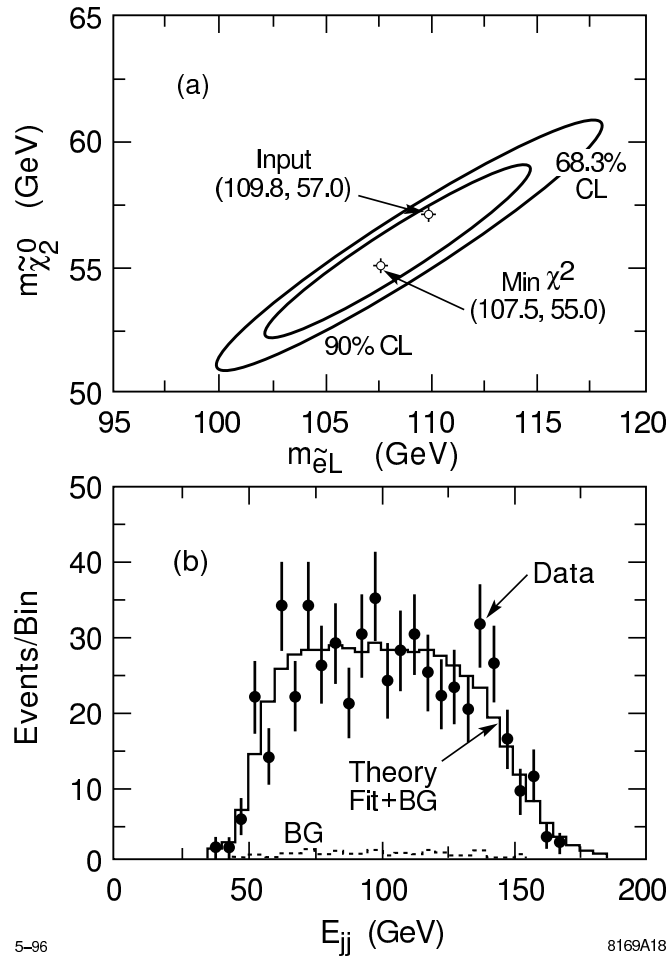


Figure 2.35: The quark pair energy distribution in the process  $e^+e^- \rightarrow \tilde{\chi}_1^+\tilde{\chi}_1^- \rightarrow q\bar{q}\tilde{\chi}_1^0q\bar{q}\tilde{\chi}_1^0$  and the fit to the  $\tilde{\chi}_1^+$ ,  $\tilde{\chi}_1^0$  masses. The fit gives the mass values  $M_{\tilde{\chi}_1^+} = 107.5 \pm 6.5$  GeV and  $M_{\tilde{\chi}_1^0} = 55.0 \pm 3.5$  GeV.

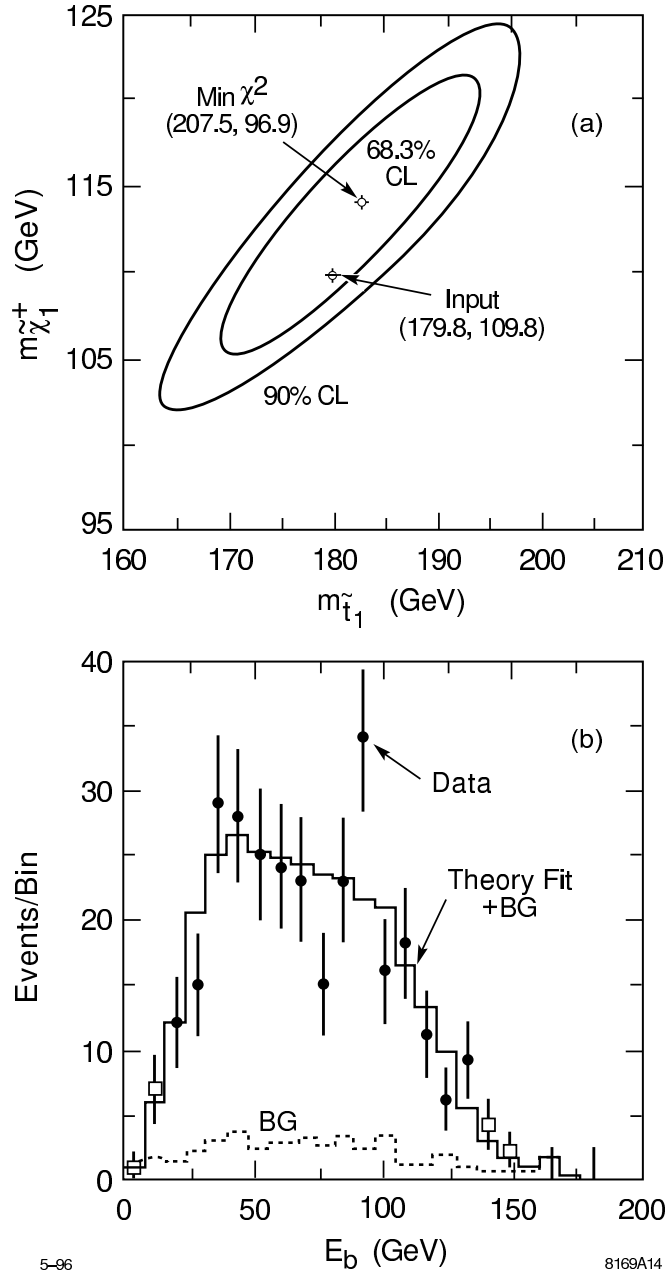


Figure 2.36: The b-jet energy distribution in the process  $e^+e^- \rightarrow \tilde{t}_1\tilde{t}_1^- \rightarrow b\tilde{\chi}_1^+\bar{b}\tilde{\chi}_1^-$  and the fit to the  $\tilde{t}_1\tilde{\chi}_1^+$  masses. The fit gives the mass values  $M_{\tilde{t}_1} = 182 \pm 11\text{GeV}$  and  $M_{\tilde{\chi}_1^+} = 114 \pm 8\text{ GeV}$ .

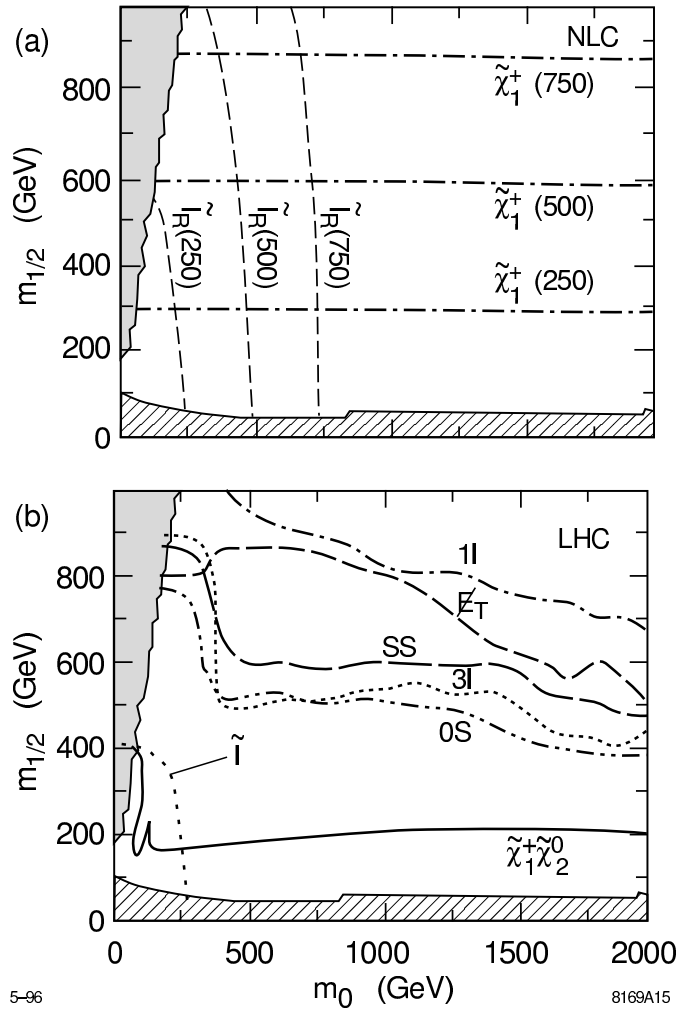


Figure 2.37: Comparison of the reach of the NLC(0.5 TeV), NLC(1.0), NLC(1.5) presented in the top figure, and the LHC assuming an integrated luminosity of  $10 \text{ fb}^{-1}$  in the bottom figure. The contours are labeled  $\tilde{l}$  for the slepton reach,  $\tilde{\chi}_1^+ \tilde{\chi}_1^0$  for the  $\tilde{\chi}_1^+ \tilde{\chi}_1^0 \rightarrow 3l$  reach,  $1l$  for the reach via lepton + jets +  $\cancel{E}_T$  events,  $\cancel{E}_T$  for events with multi-jets +  $\cancel{E}_T$ , SS for same-sign dileptons + jets +  $\cancel{E}_T$  and  $3l$  for trilepton + jets +  $\cancel{E}_T$ .

## 2.6 Anomalous Gauge Boson Couplings

Although the Standard Electroweak Model has been verified to astounding precision in recent years at LEP and SLC, one important component has not been tested directly with significant precision: the non-Abelian self couplings of the weak vector gauge bosons. Deviations of non-abelian couplings from expectation would signal new physics, perhaps arising from unexpected loop corrections involving propagators of new particles. In addition, as will be discussed in Chapter 8, precise measurements of  $WWV$  couplings, where  $V = \gamma$  or  $Z$ , can provide important information on the nature of electroweak symmetry breaking. Recent results from CDF and D0 indicate the presence of triple gauge boson couplings, but have not yet reached a precision better than order unity [75]. Upcoming measurements at LEP II, at an upgraded Tevatron and at the LHC will improve upon this precision considerably, but cannot match the expected precision of a 500 GeV NLC, much less that of a 1.0 or 1.5 TeV NLC. There exist indirect constraints on the anomalous couplings from the precision electroweak measurements at the  $Z^0$  resonances, in particular, from the fact that loop diagrams involving weak vector bosons are seen to take the values expected in the Standard Model. However, the ambiguities in the calculation of these diagrams call for more direct measurements [76].

In this brief report we restrict attention mainly to measurement of possibly anomalous  $WWV$  couplings via the process  $e^+e^- \rightarrow W^+W^-$ , but much work has been done on other processes that involve non-abelian couplings in  $e^+e^-$  annihilation, including  $ZZ\gamma$ ,  $Z\gamma\gamma$ ,  $WWZZ$ , and  $WWWW$  [75]. In addition, many of these couplings can also be measured independently using the  $e^-e^-$ ,  $e^-\gamma$  and  $\gamma\gamma$  options for the NLC. We will describe one common parametrization of anomalous  $WWV$  couplings, summarize present and expected pre-NLC measurements of  $WWV$  couplings, and discuss in more detail what can be done at the NLC.

### 2.6.1 Parametrization

In parametrizing anomalous couplings, we follow the notation of Ref. [4] in which the generic effective Lagrangian for the  $WWV$  vertex is written:

$$\begin{aligned}
L_{WWV}/g_{WWV} &= i g_1^V (W_{\mu\nu}^\dagger W^\mu V^\nu - W_\mu^\dagger V_\nu W^{\mu\nu}) + i \kappa_V W_\mu^\dagger W_\nu V^{\mu\nu} + \frac{i \lambda_V}{M_W^2} W_{\lambda\mu}^\dagger W_\nu^\mu V^{\nu\lambda} \\
&\quad - g_A^V W_\mu^\dagger W_\nu (\partial^\mu V^\nu + \partial^\nu V^\mu) + g_5^V \epsilon^{\mu\nu\rho\sigma} (W_\mu^\dagger \overset{\leftrightarrow}{\partial}_\rho W_\nu) V_\sigma + \tilde{\kappa}_V W_\mu^\dagger W_\nu \tilde{V}^{\mu\nu} \\
&\quad + \frac{i \tilde{\lambda}_V}{M_W^2} W_{\lambda\mu}^\dagger W_\nu^\mu \tilde{V}^{\nu\lambda}, \tag{2.11}
\end{aligned}$$

where  $W_{\mu\nu} \equiv \partial_\mu W_\nu - \partial_\nu W_\mu$ ,  $V_{\mu\nu} \equiv \partial_\mu V_\nu - \partial_\nu V_\mu$ ,  $(A \overset{\leftrightarrow}{\partial}_\mu B) \equiv A(\partial_\mu B) - (\partial_\mu A)B$ , and  $\tilde{V}_{\mu\nu} \equiv \frac{1}{2} \epsilon_{\mu\nu\rho\sigma} V^{\rho\sigma}$ . The normalization factors are defined for convenience to be  $g_{WW\gamma} \equiv -e$  and  $g_{WWZ} \equiv -e \cot \theta_W$ . The 7 coupling parameters defined in Eq. 2.11 for each of  $\gamma$  and  $Z$  include the C and P violating couplings  $g_5^V$  as well as the CP-violating couplings  $g_A^V$ ,  $\tilde{\kappa}_V$ ,  $\tilde{\lambda}_V$ . In most studies and in this one, such terms are neglected. At tree level in the Standard

Model  $g_1^V = \kappa_V = 1$  and  $\lambda_V = g_4^V = g_5^V = \tilde{\kappa}_V = \tilde{\lambda}_V = 0$ . The couplings in Eq. 2.11 should properly be written as form factors with momentum-dependent values. This complication is of little importance at an  $e^+e^-$  collider where the  $WW$  center of mass energy is well defined, but it must be borne in mind for other processes, particularly those measurable at hadron colliders.

We follow the common convention in defining  $\Delta g_1^Z \equiv g_1^Z - 1$  and  $\Delta \kappa_V \equiv \kappa_V - 1$ . The  $W$  electric charge fixes  $g_1^\gamma(q^2 \rightarrow 0) \equiv 1$ . In perhaps more familiar notation, one can express the  $W$  magnetic dipole moment as  $\mu_W \equiv \frac{e}{2M_W}(1 + \kappa_\gamma + \lambda_\gamma)$  and the  $W$  electric quadrupole moment as  $Q_W \equiv -\frac{e}{M_W^2}(\kappa_\gamma - \lambda_\gamma)$ .

In any model with new physics at high energy that couples to the  $W$  boson, the anomalous couplings will be induced at some level. A useful way to represent this effect is to write an  $SU(2) \times U(1)$ -invariant effective Lagrangian to represent the effects of the new physics, and then to couple this to the weak vector bosons by gauging the symmetry. In the literature, this has been done using both linear and nonlinear effective Lagrangians [76, 77, 78]. Typically, the anomalous couplings predicted in such models are suppressed by factors of  $M_W^2/\Lambda^2$ , where  $\Lambda$  is a multi-TeV scale, or by factors  $\alpha_w/4\pi$ . These lead to typical values of the anomalous couplings below  $10^{-2}$  and make it difficult to observe these couplings before directly observing the new physics itself. In the Standard Model one expects loop contributions of  $O(10^{-3})$  [79]. In the supersymmetry model, one might expect loop contributions, depending on the values of the supersymmetry parameters [80].

For the present discussion, we use a linear realization with the additional constraint of equal couplings for the  $U(1)$  and  $SU(2)$  terms in the effective Lagrangian that contribute to anomalous triple gauge boson couplings. This gives an effective lagrangian with two free parameters, which we will take to be  $K_\gamma$  and  $\lambda_\gamma$ . This restriction is called the ‘HISZ scenerio’ [81]. This restriction of the parameter space has recently been applied to comparative studies of the anomalous  $W$  couplings at colliders [75]. It is important to note, however, that studies of  $e^+e^- \rightarrow W^+W^-$  at the NLC can also test this hypothesis by independently determining the  $\gamma$  and  $Z$  couplings to the  $W$  [82].

## 2.6.2 Present and Expected Pre-NLC Measurements

The only present direct measurements of  $WWV$  couplings come from the CDF and D0 Experiments [75] at the Tevatron, which have searched for  $WW$ ,  $WZ$ , and  $W\gamma$  production. The  $WW$  and  $WZ$  searches have yielded  $O(1)$  candidates and the  $W\gamma$  searches have yielded  $O(10)$  candidates, consistent with expectation. These observations have led to limits on the corrections to the coupling parameters of order unity. For example, D0 sets a 95% CL range  $-1.8 < \Delta \kappa_\gamma < 1.9$  assuming  $\lambda_\gamma = 0$  or a range  $-0.6 < \lambda_\gamma < 0.6$  assuming  $\kappa_\gamma = 0$  (both limits assume  $\Lambda = 1$  TeV in the appropriate form factors).

One expects significant improvement at LEP II [83], once the accelerator exceeds the  $W$ -pair threshold energy. Techniques similar to those described below will be applied to  $e^+e^- \rightarrow W^+W^-$  events at c.m. energies ranging from threshold at  $\approx 160$  GeV to  $\approx 195$  GeV.

Assuming no anomalous couplings are observed after an integrated luminosity of  $500 \text{ pb}^{-1}$ , 95% CL limits on individual couplings (all others set to zero) of  $O(0.1)$  are expected.

After the Main Injector upgrade has been completed, it is expected that the Tevatron will collect  $O(1-10) \text{ fb}^{-1}$  of data. (Further upgrades in luminosity are also under discussion.) If  $10 \text{ fb}^{-1}$  is achieved, it is expected [75] that limits on  $\Delta\kappa_\gamma$  and  $\lambda_\gamma$  will be obtained that are competitive with those from LEP II with  $500 \text{ pb}^{-1}$ .

Finally, one expects the LHC accelerator to turn on sometime before the NLC and to look for the same signatures considered at the Tevatron. The planned luminosity and c.m. energy, however, give the LHC a large advantage over even the Main Injector Tevatron in probing anomalous couplings. The ATLAS Collaboration has estimated [24] that with  $100 \text{ fb}^{-1}$ , one can obtain (in the HISZ scenario) 95% CL limits on  $\Delta\kappa_\gamma$  and  $\lambda_\gamma$  in the range  $5-10 \times 10^{-3}$ . We should note that these studies do not yet include helicity analysis on the  $W$  bosons.

### 2.6.3 Measurements in $W$ Pair Production at the NLC

The fact that the expected LHC limits improve dramatically upon those of a high-luminosity Tevatron indicates the importance of center-of-mass energy. This reflects the fact that, in the effective Lagrangian description, the anomalous couplings arise from higher-dimension effective interactions.

The NLC has an added advantage over hadron colliders in reconstructing  $W$  pair events due to absence of spectator partons. To a good approximation, full energy and momentum conservation constraints can be applied to the visible final states. Thus an  $e^+e^- \rightarrow W^+W^-$  event can ideally be characterized by five angles: the production angle  $\Theta_W$  of the  $W^-$  with respect to the electron beam, the polar and azimuthal decay angles  $\theta^*$  and  $\phi^*$  of one daughter of the  $W^-$  in the  $W^-$  reference frame, and the corresponding decay angles  $\bar{\theta}^*$  and  $\bar{\phi}^*$  of one of the  $W^+$  daughters. In practice, initial-state photon radiation and final-state photon and gluon radiation (in hadronic  $W$  decays) complicate the picture. So does the finite width of the  $W$ . Nevertheless, for the studies below, we will characterize  $e^+e^- \rightarrow W^+W^-$  events by these five angles and fit distributions in the angles to obtain values of anomalous couplings.

At high energies, the  $e^+e^- \rightarrow W^+W^-$  process is dominated by  $t$ -channel  $\nu_e$  exchange, leading primarily to very forward-angle  $W$ 's where the  $W^-$  has an average helicity near minus one. This makes the bulk of the cross section difficult to observe with precision. However, the amplitudes affected by the anomalous couplings are not forward peaked; the central and backward-scattered  $W$ 's are measurably altered in number and helicity by the couplings.  $W$  helicity analysis through the decay angular distributions provides a powerful probe of anomalous contributions. Most studies, including those discussed here, restrict attention to events for which  $|\cos \Theta_W| < 0.8$ . Not surprisingly, the most powerful channel to use is one in which one  $W$  decays leptonically (to  $e\nu$  or  $\mu\nu$ ) and the other hadronically ( $\approx 30\%$  of all  $e^+e^- \rightarrow W^+W^-$  events) Although one gains statistics when both  $W$ 's decay hadronically, one loses considerable discriminating power from being unable to purely tag the charge of

the  $W$  daughter quarks. The channel in which both  $W$ 's decay leptonically suffers from both poor statistics and kinematic ambiguities due to two undetected neutrinos. For the leptonic  $vs$  hadronic channel, the lepton energy carries important information for kinematic reconstruction. For simplicity, most studies have not yet attempted to incorporate  $W \rightarrow \tau\nu$  decays.

Figure 2.38 (taken from Ref. [84]) shows 95% CL exclusion contours in the plane  $\lambda_\gamma$   $vs$   $\Delta\kappa_\gamma$  in the HISZ scenario for different c.m. energies and integrated luminosities (0.5 fb<sup>-1</sup> at 190 GeV, 80 fb<sup>-1</sup> at 500 GeV, and 190 fb<sup>-1</sup> at 1500 GeV). These contours are based on ideal reconstruction of  $W$  daughter pairs produced on mass-shell with no initial-state radiation. The contours represent the best one could possibly do. A previous study [82] assuming a very high-performance detector but including initial-state radiation and a finite  $W$  width found some degradation in these contours, primarily due to efficiency loss when imposing kinematic requirements to suppress events far off mass-shell or at low effective c.m. energies. Nevertheless, one attains a precision of  $O(10^{-3})$  at NLC(500) and  $O(\text{few} \times 10^{-4})$  at NLC(1500). Another nice feature of coupling studies at NLC is the ability to disentangle couplings in models more general than HISZ via tuning of the electron beam polarization, as shown in Ref. [82].

A study [85] undertaken for this workshop has examined the effects of detector resolution on achievable precisions. One might expect *a priori* that the charged track momentum resolution would be most critical since the energy spectrum for the  $W$ -daughter muons peaks at a value just below the beam energy, falling off nearly linearly with decreasing energy. One might also expect the hadron calorimeter energy resolution to be important in that it affects the energy resolution of jets to be identified with underlying  $W$ -daughter quarks. Indeed, one finds that these resolutions do matter, but that the nominal resolution parameters assumed for the purposes of this workshop are quite adequate. A significant source of degradation in sensitivity to anomalous couplings comes from initial state photon radiation, aggravated by beamsstrahlung, the presence of which is difficult to establish in a single lepton-jets event, given the undetected neutrino. In this respect, the four-jets channel in which both  $W$ 's decay hadronically, is more promising. Further investigation of this channel is in progress.

In summary, the studies reviewed in this section confirm the power of the NLC to extract anomalous couplings. We expect some degradation in coupling parameters precision from the ideal case due to the underlying physical phenomena of initial state photon radiation and the finite  $W$  width and a smaller degradation from the imperfection of matching detected particles to primary  $W$  daughters, but these effects are not serious and should be straightforward to incorporate in a real measurement.

## 2.6.4 Measurements in Other Reactions at the NLC

In addition, the NLC allows measurements of non-Abelian gauge boson couplings in other channels [75]. The process  $e^+e^- \rightarrow Z\gamma$  probes  $ZZ\gamma$  and  $Z\gamma\gamma$  couplings, and processes such as  $e^+e^- \rightarrow WWZ$  probe quartic couplings. The  $WW\gamma$  and  $WWZ$  couplings can be probed

independently via the processes  $e^+e^- \rightarrow \nu\bar{\nu}\gamma$  and  $e^+e^- \rightarrow \nu\bar{\nu}Z$ , respectively.

Similar measurements can be carried out at  $e^-e^-$ ,  $e^-\gamma$  and  $\gamma\gamma$  colliders, where the expected reduction in luminosity is at least partly compensated by other advantages [82, 86]. For example, the process  $\gamma e^- \rightarrow W^-\nu_e$  probes the  $WW\gamma$  coupling, independent of  $WWZ$  effects. The polarization asymmetry in this reaction reverses as the energy of the collisions is varied, and the location of this zero-crossing provides a sensitive probe of  $\lambda_\gamma$  [87]. The reaction  $\gamma\gamma \rightarrow W^+W^-$  also separates effects of the  $\gamma$  couplings from those of the  $Z$ , and also probes the 4-boson  $WW\gamma\gamma$  vertex. The power of this facility is enhanced by its ability to polarize both incoming beams [82].

### 2.6.5 Conclusions

Although there will have been a number of measurements of anomalous coupling parameters from LEP II, the Tevatron, and the LHC before the turn-on of the NLC, the precisions on the values of the couplings attainable with the NLC will quickly overwhelm the previous measurements. Moreover, the higher the accessible energy at NLC, the more dramatic the improvement will be. Figure 2.39 (taken from Ref. [88]) shows a useful comparison among these accelerators. The enormous potential of the NLC is apparent.

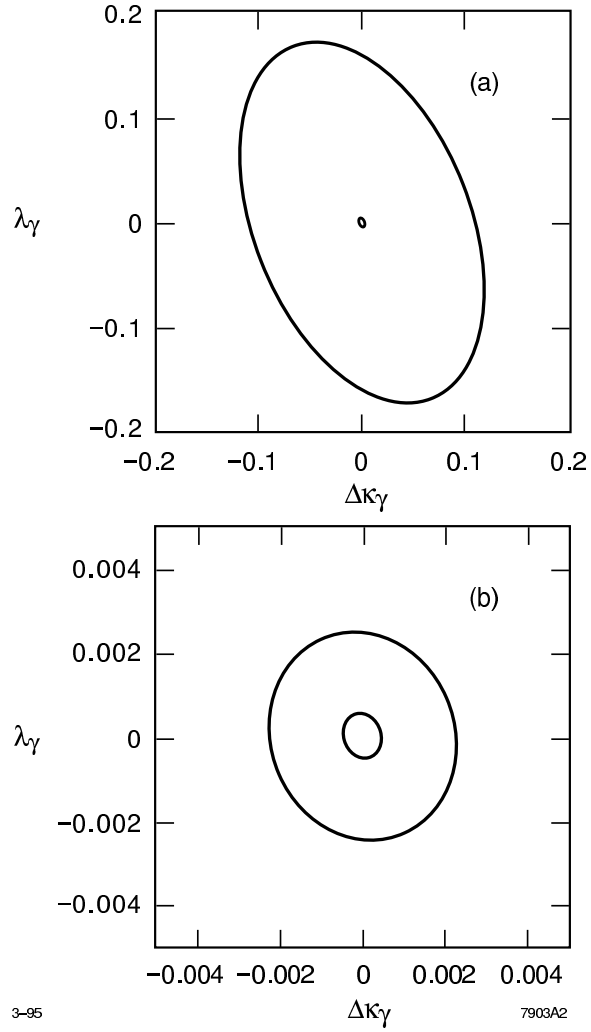


Figure 2.38: 95% CL contours for  $\Delta\kappa_\gamma$  and  $\lambda_\gamma$  in the HISZ scenario. The outer contour in (a) is for  $E_{\text{CM}} = 190$  GeV and  $0.5 \text{ fb}^{-1}$ . The inner contour in (a) and the outer contour in (b) is for  $E_{\text{CM}} = 500$  GeV with  $80 \text{ fb}^{-1}$ . The inner contour in (b) is for  $E_{\text{CM}} = 1.5$  TeV with  $190 \text{ fb}^{-1}$ .

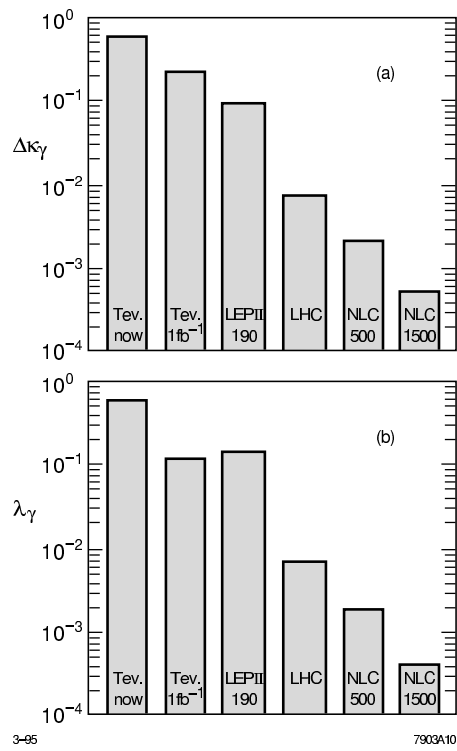


Figure 2.39: Comparison of representative 95% CL upper limits on  $\Delta\kappa_\gamma$  and  $\lambda_\gamma$  for present and future accelerators.

## 2.7 Strong $WW$ Scattering

In this section we examine how well an  $e^+e^-$  linear collider with a center-of-mass energy of 500–1500 GeV can study the strongly interacting Higgs sector. We also compare the estimated sensitivity of such a collider with that of the LHC.

### 2.7.1 The Reaction $e^+e^- \rightarrow W^+W^-$

Strong electroweak symmetry breaking affects the reaction  $e^+e^- \rightarrow W^+W^-$  through anomalous couplings at the  $W^+W^-\gamma$  and  $W^+W^-Z$  vertices and through enhancements in  $W_L^+W_L^-$  production due to  $I = J = 1$  resonances. Here we have used the symbol  $W_L$  to denote a longitudinally polarized W boson. Anomalous couplings at the three-gauge boson vertices are related to the chiral Lagrangian parameters  $L_{9L}$  and  $L_{9R}$  [77]. A technipion form factor  $F_T$  is used to parameterize [89] the strong  $W_L^+W_L^-$  interaction in the  $I = J = 1$  state; it is analogous to the rho-dominated pion form factor in  $e^+e^- \rightarrow \pi^+\pi^-$ .

Whether one is measuring trilinear vector boson couplings or searching for an enhancement in  $W_L^+W_L^-$  production, the experimental goal is the same: disentangle the  $W^+W^-$  polarization states, and in particular isolate the polarization state  $W_L^+W_L^-$ . We shall describe the results of a study that utilizes a final-state helicity analysis of all observable final-state variables in order to isolate  $W_L^+W_L^-$  production [3].

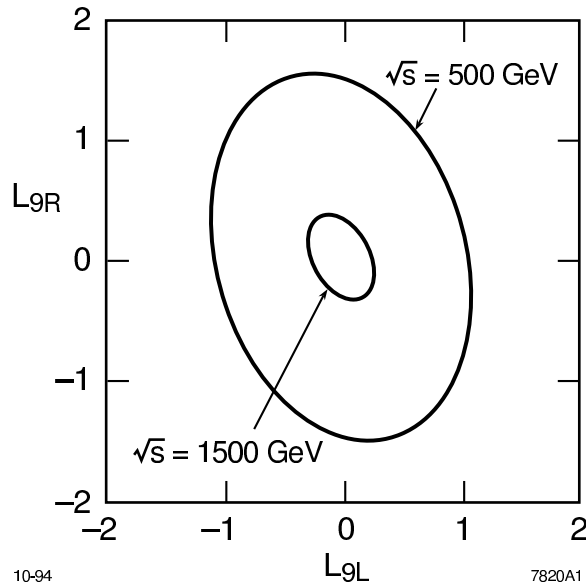


Figure 2.40: The 95% confidence level contours for  $L_{9L}$  and  $L_{9R}$  at  $\sqrt{s} = 500$  GeV with  $80 \text{ fb}^{-1}$ , and at  $\sqrt{s} = 1500$  GeV with  $190 \text{ fb}^{-1}$ . The outer contour is for  $\sqrt{s} = 500$  GeV. In each case the initial state electron polarization is 90%.

The maximum likelihood method is used to fit for chiral Lagrangian parameters or for the real and imaginary parts of the technipion form factor. Figure 2.40 shows the 95% confidence level contours for the chiral Lagrangian parameters  $L_{9L}$  and  $L_{9R}$  at  $\sqrt{s} = 500$  GeV and at  $\sqrt{s} = 1500$  GeV. The parameters  $L_{9L}$  and  $L_{9R}$  are normalized such that values of  $\mathcal{O}(1)$  are expected if the Higgs sector is strongly interacting.

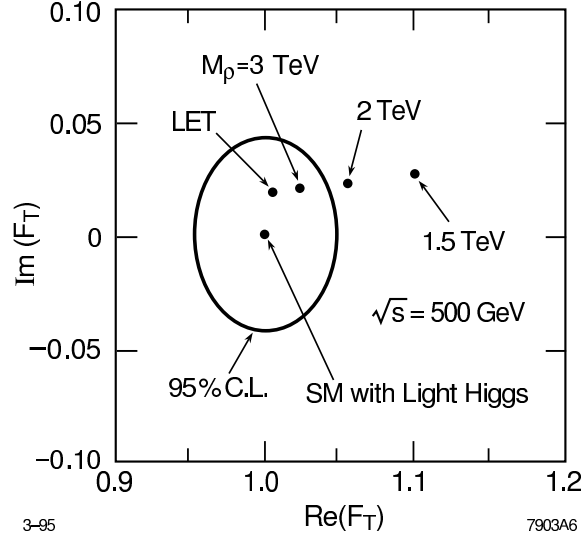


Figure 2.41: 95% confidence level contours for the real and imaginary parts of  $F_T$  at  $\sqrt{s} = 500$  GeV with  $80 \text{ fb}^{-1}$ . The values of  $F_T$  for various technirho masses are indicated.

Figure 2.41 shows the 95% confidence level contour for the real and imaginary parts of  $F_T$  at  $\sqrt{s} = 500$  GeV. The use of beam polarization is essential to obtain a strong constraint on  $\text{Im}(F_T)$ . Also indicated are values of  $F_T$  for various technirho masses. The infinite technirho mass point is labelled Low Energy Theorem (LET) since in this limit there is residual  $W_L^+ W_L^-$  scattering described by the same low energy theorems that govern low energy  $\pi^+ \pi^-$  scattering. We see that the NLC at  $\sqrt{s} = 500$  GeV can exclude technirho masses up to about 2.5 TeV and can discover technirho resonances with masses of more than 1.5 TeV. The significance of the 1.5 TeV technirho signal would be  $6.7\sigma$ . A 1.0 TeV technirho would produce a  $17.7\sigma$  signal. For comparison, the minimal technicolor model predicts a technirho mass of about 2.0 TeV.

Figure 2.42 contains confidence level contours for the real and imaginary parts of  $F_T$  at  $\sqrt{s} = 1500$  GeV. The non-resonant LET point is well outside the light Higgs 95% confidence level region and corresponds to a  $4.5\sigma$  signal. The labeling of points here deserves some comment. We use the model of [89] to describe the form factor  $F_T$ . In this model, as the vector resonance mass is taken to infinity, its effect on the form factor decreases, and what is left behind is the residual scattering predicted by the LET. The values for high-mass technirho indicate this decoupling. With this understanding, the 6 TeV, 4 TeV and 3 TeV

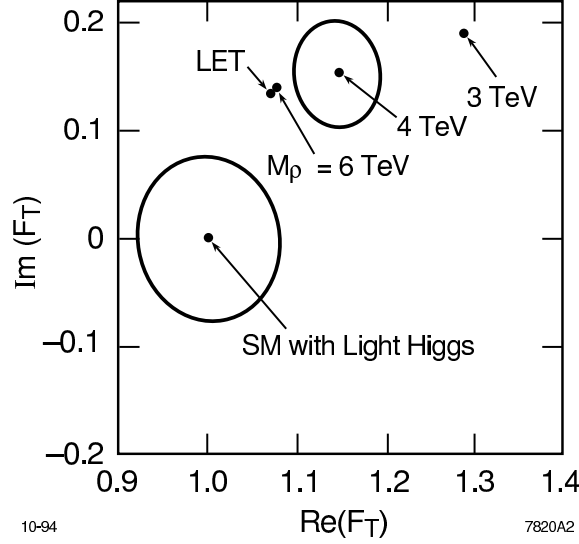


Figure 2.42: Confidence level contours for the real and imaginary parts of  $F_T$  at  $\sqrt{s} = 1500$  GeV with  $190 \text{ fb}^{-1}$ . The contour about the light Higgs value of  $F_T = (1, 0)$  is 95% confidence level and the contour about the  $M_\rho = 4$  TeV point is 68% confidence level.

technirho points correspond to  $4.8\sigma$ ,  $6.5\sigma$ , and  $11\sigma$  signals, respectively. A 2 TeV technirho would produce a  $37\sigma$  signal.

It might appear that the value of  $F_T$ , and hence the significance of technirho signals, would be very sensitive to the technirho width when  $\sqrt{s}$  is much less than the technirho mass. In the model we have considered, however, this is not true. The results presented above were obtained assuming that  $\Gamma_\rho/M_\rho = 0.22$ . If, for example, the technirho width is reduced to  $\Gamma_\rho/M_\rho = 0.03$  then the 1 TeV signal at  $\sqrt{s} = 500$  GeV is reduced from  $17.7\sigma$  to  $16.3\sigma$ , the 1.5 TeV signal at  $\sqrt{s} = 500$  GeV is reduced from  $6.7\sigma$  to  $6.4\sigma$ , and the 4 TeV signal at  $\sqrt{s} = 1500$  GeV is reduced from  $6.5\sigma$  to  $6.3\sigma$ .

## 2.7.2 The Reaction $e^+e^- \rightarrow \nu\bar{\nu}W^+W^-$ and $\nu\bar{\nu}ZZ$

The important gauge boson scattering processes  $W_L^+W_L^- \rightarrow W_L^+W_L^-$  and  $W_L^+W_L^- \rightarrow Z_LZ_L$  are studied at the NLC with the reactions  $e^+e^- \rightarrow \nu\bar{\nu}W^+W^-$  and  $e^+e^- \rightarrow \nu\bar{\nu}ZZ$ . We describe the results that Barger *et al.* [90] have obtained by analyzing these processes.

Barger *et al.* use several models to test the effectiveness of their analysis of  $e^+e^- \rightarrow \nu\bar{\nu}W^+W^-$  and  $\nu\bar{\nu}ZZ$ . In addition to the Standard Model Higgs boson with mass  $m_H = 1$  TeV, they use a Chirally-Coupled Scalar (CCS) model, a Chirally-Coupled Vector (CCV) model, and the LET model. They utilize a series of cuts to produce an event sample that is rich in the final states  $\nu\bar{\nu}W_L^+W_L^-$  and  $\nu\bar{\nu}Z_LZ_L$ . Figure 2.43 shows the  $M_{WW}$  and  $M_{ZZ}$  distributions after all cuts. The 1 TeV Higgs scalar resonance stands out in both the  $\nu\bar{\nu}WW$